Review

Hui Wang*

Plasmon-driven molecular scission

https://doi.org/10.1515/nanoph-2024-0417
Received August 12, 2024; accepted November 7, 2024;
published online November 21, 2024

Abstract: Plasmon-driven photocatalysis offers a unique means of leveraging nanoscale light–matter interactions to convert photon energy into chemical energy in a chemoselective and regioselective manner under mild reaction conditions. Plasmon-driven bond cleavage in molecular adsorbates represents a critical step in virtually all plasmon-mediated photocatalytic reactions and has been identified as the rate-determining step in many cases. This review article summarizes critical insights concerning plasmon-triggered bond-cleaving mechanisms gained through combined experimental and computational efforts over the past decade or so, elaborating on how the plasmon-derived physiochemical effects, metal–adsorbate interactions, and local chemical environments profoundly influence chemoselective bond-cleaving processes in a diverse set of molecular adsorbates ranging from small diatomic molecules to aliphatic and aromatic organic compounds. As demonstrated by several noteworthy examples, insights gained from fundamental mechanistic studies lay a critical knowledge foundation guiding rational design of nanoparticle–adsorbate systems with desired plasmonic molecule-scissoring functions for targeted applications, such as controlled release of molecular cargos, surface coating of solid-state materials, and selective bond activation for polymerization reactions.

Keywords: plasmon resonances; bond cleavage; plasmonic photocatalysis; hot carriers; field enhancement; photothermal transduction

1 Introduction

Metallic nanostructures combine finely tunable optical properties with remarkable catalytic activities in single nanoscale entities, creating unique opportunities of utilizing light–matter interactions as a leverage to optimize the efficiencies, rates, and selectivity of solar-to-chemical energy conversion processes [1]–[6]. The optical responses of a metallic nanoparticle are dominated by resonantly excited collective oscillations of free electrons against the restoring force of positively charged nucleus lattices within the nanoparticulate confinement (Figure 1a), an interesting phenomenon known as localized plasmon resonances [7]–[10]. An optically excited plasmonic nanoparticle may function as a nanoscale light-concentrating antenna, drastically enhancing not only the light absorption/scattering efficiencies at the resonant frequencies but also the local electric fields near the nanoparticle surfaces [7]–[10]. Plasmon resonances may decay through either radiative photon scattering or nonradiative Landau damping, and the branching ratio between the radiative and nonradiative decay is determined by the radiance of the plasmon mode, the dimensions and compositions of nanoparticles, and the local environment near the particle surfaces [6], [11]. The strongly enhanced photon scattering at the nanoparticle surfaces creates localized hot spots exploitable for plasmon-enhanced spectroscopies, such as surface-enhanced Raman scattering (SERS) [12]–[15] and surface-enhanced fluorescence (Figure 1b) [16]–[19]. When multiple metallic nanoparticles are placed close to each other, the local electric fields inside the interparticle gaps can be further enhanced by several orders of magnitude in comparison to those achievable on individual nanoparticles [7], [20], even enabling SERS detection at the single-molecule level in certain hot spots [21]–[24]. The nonradiative Landau damping can be described as a quantum mechanical process in which a plasmon quantum relaxes through excitation of an electron–hole pair within the conduction band (CB) of the metallic materials on a timescale of 1–100 fs [4], [6], [11], [25]. The photoexcited electrons derived from Landau damping are highly energetic and nonthermally distributed above the Fermi level, while the holes are distributed below the Fermi level. When the energy of the excitation photons exceeds the energy threshold for the interband electronic transitions, electrons in the valence band (VB) of the metal can also be photoexcited, producing energetic holes in the VB and excited electrons near the Fermi level in the CB [25]–[27]. These nonthermal electrons and holes, commonly

***Corresponding author: Hui Wang**, Department of Chemistry and Biochemistry, University of South Carolina, Columbia, SC 29208, USA, E-mail: wang344@mailbox.sc.edu. https://orcid.org/0000-0002-1874-5137

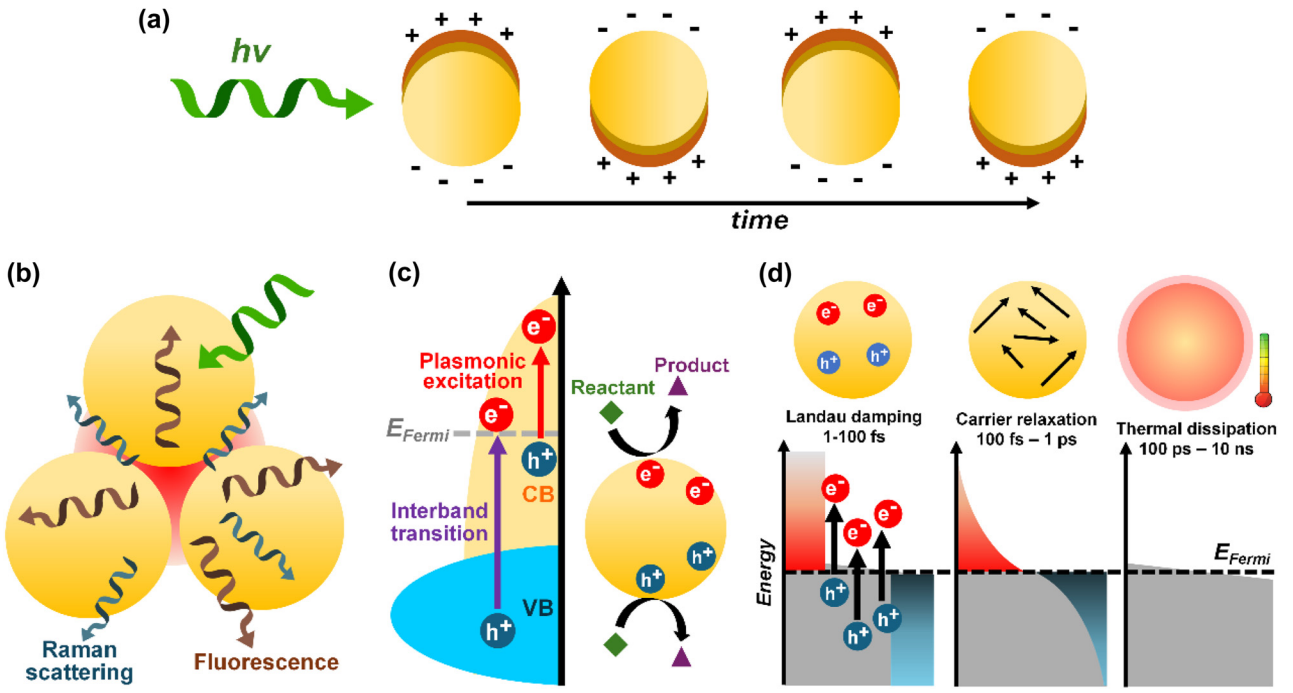

Figure 1: Excitation and decay of localized plasmon resonances in metallic nanostructures. Schematic illustrations of (a) resonant excitation of free electron oscillations in a metallic nanoparticle, (b) local field enhancements in the interparticle gaps of a plasmonically excited nanoparticle trimer, (c) photoexcitation of intraband and interband hot carriers and hot carrier-driven photochemistry on the nanoparticle surface, and (d) evolution of energy distributions of plasmonic hot carriers during Landau damping, carrier relaxation, and thermalization. The energy distributions of hot electrons are represented by the red areas above the Fermi energy, E_{Fermi}, and those of holes are represented by the blue areas below E_{Fermi}, respectively.

termed as hot carriers, can either be extracted to initiate photochemical reactions on the nanostructured metal surfaces (Figure 1c) or undergo multistep carrier relaxation and thermalization processes within the nanoparticles [4], [6], [11], [25], eventually leading to local temperature elevation in material lattices and dissipation of heat to the surrounding medium (Figure 1d).

The aforementioned photophysical effects derived from excitation and decay of plasmon resonances can be harnessed to catalyze photochemical transformations of molecular adsorbates on metallic nanoparticle surfaces [1]–[6]. By deliberately tuning the plasmon–adsorbate interactions, it becomes possible to not only selectively activate a targeted chemical bond in the adsorbate molecules but also modulate the activation energy of a specific elementary step in a multistep reaction [2], [3], [28], [29]. Because of the spatially localized nature and heterogeneous distribution of active sites, plasmon-mediated molecular transformations occur preferentially in localized hot spots rather than over the entire photocatalyst surfaces, which provides a unique way to locally tailor the surface chemistry of metallic nanoparticles with nanoscale precision [5]. Such chemoselectivity and regioselectivity are often unattainable in heterogeneous catalysis under thermal conditions.

The light-harvesting and photocatalytic behaviors of plasmonic metallic nanostructures differ strikingly from those of the conventional semiconductor photocatalysts [30]–[32]. First, the photoexcitation of excitons in semiconductors requires photon energies above the materials' band gaps, whereas the remarkable plasmonic tunability offered by metallic nanostructures makes it possible to efficiently harvest the solar energy for photochemical reactions over a much broader spectral range [32], even at excitation energies far below the energy threshold for interband electronic transitions. While the band gap engineering of semiconductor photocatalysts requires careful tuning of the sizes, compositions, and doping of the nanoparticles, the plasmonic spectral features of metallic photocatalysts can be fine-tuned to match the solar spectrum by simply tailoring the nanoparticle geometries without changing the materials' compositions. Second, certain chemical bonds in molecular adsorbates can be selectively activated to achieve desired reaction outcomes by deliberately tuning the metal–adsorbate interactions, which may give rise to chemoselectivity typically unachievable in semiconductor-driven photocatalysis [29], [33]–[36]. Third, the rate of a plasmon-driven reaction may exhibit a superlinear dependence on excitation power above certain light intensity

threshold [6], [30], which is in striking contrast to the sublinear power dependence commonly observed on semiconductor photocatalysts. Fourth, the rate of a plasmon-driven reaction may increase exponentially with the working temperature, while semiconductor photocatalysts typically exhibit decreased quantum efficiencies and slower reaction rates at elevated temperatures [30].

Photoexcited plasmonic nanostructures are catalytically versatile, capable of boosting a large variety of bond-cleaving dissociation and bond-forming coupling reactions involving a plethora of surface-adsorbed reactants ranging from small diatomic molecules and ionic species to structurally more sophisticated organic compounds and polymers [1]–[6]. While the library of plasmon-mediated photocatalytic reactions keeps expanding as the discovery of new reactions continues, there is an imperative need for developing deep and comprehensive understanding of the detailed mechanisms involved in plasmon-mediated molecule-transforming processes. Although immense research efforts have been devoted and significant advancements have been achieved over the past decade, plasmon-mediated photochemistry remains a rapidly growing research area full of fundamentally intriguing open questions and its potential for important technological applications is still far from being fully realized. Several prominent review articles published in the last decade provide comprehensive overviews of the major breakthroughs and the state-of-the-art progress in the field of plasmon-mediated photocatalysis, covering various critical aspects in the context of hot carrier energetics and dynamics (photoexcitation, relaxation, separation, and utilization) [4], [11], [37], [38], design of complex plasmonic photocatalysts (multimetallic antenna-reactor systems and metal–semiconductor heteronanostructures) [28], [39], [40], mechanistic studies using *in situ* characterization techniques (spectroscopies and microscopies) [41]–[47], and important reactions relevant to clean energy and sustainable chemistry (nitrogen fixation, hydrogen production, and carbon dioxide utilization) [48]–[51]. Some widely debated controversies, mechanistic ambiguities, and key experimental and theoretical challenges in the broadly defined research area of plasmonic photochemistry have also been discussed in several insightful perspective articles [52]–[56].

Keeping sight of the existing literature, this review focuses on a crucial step in plasmonic photocatalysis, specifically bond cleavage in molecular adsorbates on nanostructured metal surfaces. Virtually all plasmon-mediated photocatalytic reactions, regardless of how mechanistically complex and versatile they are, require cleavage of specific chemical bonds in the reactant molecules before new bonds can be formed to create the final products. The plasmon-triggered bond cleavage represents not only a critical elementary step at the early stage of the reactions but also, in many cases, the rate-limiting kinetic bottleneck of the entire molecule-transforming processes. In this review article, I will first provide an outline of the fundamental mechanisms involved in plasmon-driven cleavage of chemical bonds in molecule adsorbates. Then I will choose structurally simple homonuclear diatomic adsorbates with various interatomic bond orders, such as H_2, O_2, and N_2, as model systems to demonstrate how the photon energies can be effectively harvested by plasmonic nanoparticles to drive energetically uphill bond dissociation processes. The primary driving forces for photocatalytic scission of these diatomic molecules will be discussed in the context of several plasmon-induced physicochemical effects, such as local field enhancements, hot carrier transfer, and photothermal transduction. Next, I will elaborate on the detailed mechanisms of plasmon-driven bond cleavage in structurally more sophisticated organic molecular adsorbates. The mechanistic complexity and versatility of plasmon-driven molecular scission can be fully manifested by a selection of molecule-scissoring reactions that involve selective cleavage of a wide variety of chemical bonds, such as sulfur–sulfur, nitrogen–carbon, carbon–carbon, and carbon–halogen bonds. Built upon the insights gained from fundamental mechanistic studies, I will further showcase several deliberately designed catalyst–adsorbate systems that can be successfully employed as plasmonic molecule-scissoring tools for targeted applications, such as light-triggered drug release, light-driven surface functionalization, and selective bond activation for polymerization. Finally, I will summarize the insights gained from previous work, identify key challenges in current research, and envision future directions in this research area.

2 Fundamental working mechanisms of plasmonic molecular scissors

Resonantly excited plasmonic electron oscillations only maintain their coherence for approximately 1–10 fs before they start to partition their energies into several radiative and nonradiative decay channels [11], through which energy can be deposited into molecular adsorbates to activate certain chemical bonds for cleavage. In general, plasmon-induced bond activation involves formation of either electronically or vibrationally excited intermediates with reduced activation energies for bond dissociation. Such

activation energy reduction can be achieved through several distinct plasmon-mediated pathways dictated by local field enhancements, hot carriers, and photothermal heating, respectively.

Nanoscale resonant energy transfer processes in strongly coupled metal–molecule systems [57]–[61] have been extensively explored, revealing that the excited state lifetimes of molecular adsorbates can be significantly influenced by the plasmons of the metal substrates. In metal–semiconductor hybrid nanostructures, the interband transitions in the semiconductors can be enhanced by the plasmons of the metallic domains, an interesting process often known as plasmon-induced resonance energy transfer (PIRET) in the literature [62]–[64]. In metal–molecule systems, the large local field enhancements near the metallic nanoparticle surfaces are exploitable for enhancing intramolecular electronic excitations in the adsorbates [65]. When resonant with the plasmons, vibronic transitions between the frontier molecular orbitals, specifically the highest occupied molecular orbital (HOMO) and the lowest unoccupied molecular orbital (LUMO), of the adsorbates can be drastically enhanced benefiting from the intense scattering photons reradiated from the plasmonic nanoparticles (Figure 2a). The efficiency of plasmon-enhanced intramolecular excitations is determined by the coupling between the locally enhanced electric fields in hot spots with transition dipoles in the molecules near the metal surfaces. Molecules in their excited vibronic states may either evolve along a dissociative potential energy surface until a covalent bond is fully dissociated or relax back to an excited vibrational state in the ground electronic state (Figure 2b). These excitation and relaxation processes can be fully described in the context of the Franck–Condon Principle. The plasmon-enhanced intramolecular excitations do not involve charge transfer between the metal nanoparticles and surface adsorbates and thus do not require direct contact of the molecules with the metal surface. However, a molecule must be in close proximity to the nanoparticle surface, typically within a few nanometers, to achieve appreciable enhancements of intramolecular excitations because the local field intensity decays rapidly as the distance between the molecule and the metal surface increases [66], [67].

The nonradiative plasmon decay is the primary pathway for generating nonthermal charge carriers [4], [11], [37], [38], [68]. Through Landau damping, the energy of absorbed photons is utilized to excite electron–hole pairs in the metallic nanostructures, leading to transient, nonthermal distribution of electrons and holes across the Fermi level of the metal. The primary hot electrons generated during Landau damping, also referred to as the first-generation nonequilibrium carriers, undergo a rapid relaxation process on the

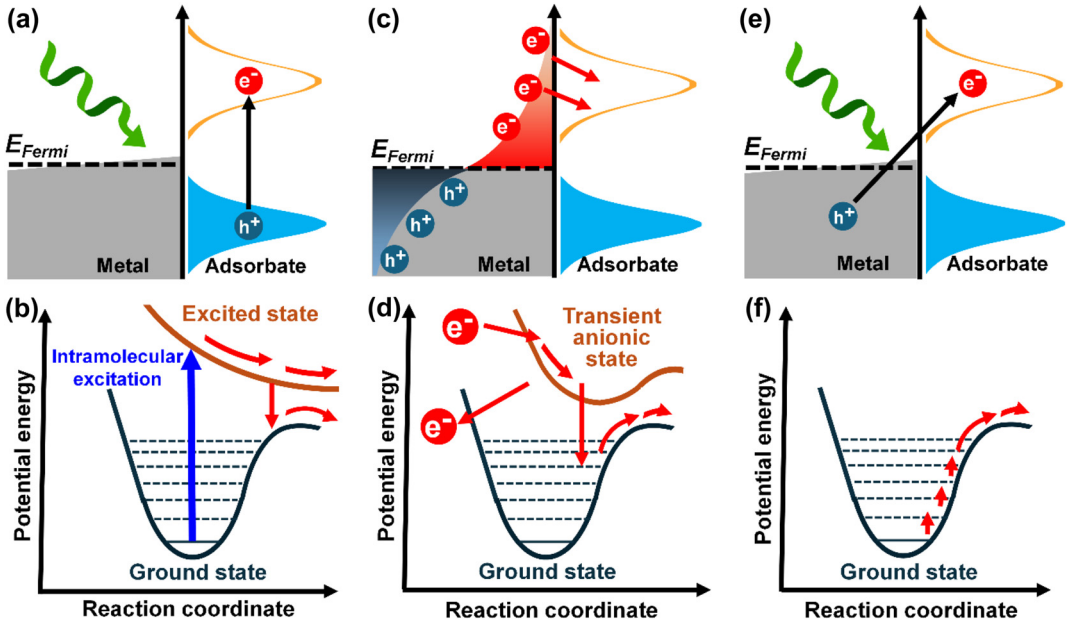

Figure 2: Mechanisms of plasmon-driven bond cleavage. (a) Schematic illustration and (b) potential energy surface diagram of bond cleavage driven by plasmon-enhanced intramolecular electronic excitations. (c) Schematic illustration and (d) potential energy surface diagram of bond cleavage driven by indirect metal-to-adsorbate transfer of hot electrons. (e) Schematic illustration of direct electron injection into molecular adsorbates through chemical interface damping. (f) Potential energy surface diagram of a photothermally triggered bond cleavage involving deposition of thermal energy into adsorbate vibrations. Adapted from ref. [65]. Copyright 2019 Wiley.

timescales of ∼100 fs to ∼1 ps to redistribute their energies among larger populations of electrons in the metallic nanostructures through inelastic electron–electron and electron–surface scattering. The energy distribution profiles of the hot electrons evolve over time during carrier relaxation, resulting in Fermi-Dirac-like distributions of hot electrons featured by an effective electron temperature higher than the temperature of the material lattices (Figure 1d). Given sufficient energy, hot electrons accumulated on nanoparticle surfaces can get injected into unoccupied orbitals of adsorbate molecules (Figure 2c) to drive photocatalytic reactions. Similarly, hot hole-driven reactions may also take place upon transfer of electrons from occupied orbitals of molecular adsorbates to the metal. Because carrier relaxation may start immediately after Landau damping before the hot carriers reach the nanoparticle surfaces and get ejected, most photocatalytic reactions are primarily driven by the relaxed hot carriers rather than the less-populated first-generation hot carriers [69], even though the later one is more energetic. Therefore, Landau damping-driven photocatalysis typically involves the injection of hot electrons into the adsorbate orbitals that are fairly close to the Fermi level of the metal [69]. The short lifetimes, limited diffusion lengths, and multiple competing relaxation pathways are all key factors limiting the utilization efficiencies of plasmonic hot carriers for photocatalysis [4], [11], [29], [37], [38], [69].

The transfer of hot electrons from metals to molecular adsorbates leads to the formation of transient anionic radicals whose activation energies for bond cleavage are significantly lower than those of their neutral counterparts in the ground state (Figure 2d). After releasing an electron back to the metallic nanoparticle, a transient anionic radical can be converted to its neutral counterpart in a vibrationally excited state (Figure 2d), an interesting process known as plasmon-induced vibrational activation [2], [3]. The hot electron-induced activation of a certain vibrational mode becomes particularly effective when the potential energy surface of a transient anionic adsorbate is significantly modified and shifted in comparison to that of its neutral counterpart. For example, Kim and coworkers [70] recently found that the symmetric stretching vibration of the nitro group could be selectively excited upon transient hot electron transfer to the antibonding LUMO of surface-adsorbed *para*-nitrothiophenol. Interestingly, a significant population of the vibrationally excited *para*-nitrothiophenol adsorbates existed in the overtone-excited states, which exhibited even higher reactivities than those in the first-excited vibrational states.

The involvement of photoexcited hot carriers in bond activation of molecular adsorbates was initially observed in photodesorption processes on single-crystal surfaces of bulk metals illuminated by femtosecond-pulse lasers at photon flux densities 6–9 orders of magnitude higher than the solar radiation [71]–[76]. In the surface photochemistry community, this phenomenon is referred to as desorption induced by electronic transitions (DIET) [77], [78]. Metallic nanoparticles, especially small ones within the sub-10 nm size regime, have been of particular interest for heterogeneous catalysis because of their large surface area-to-volume ratios, high abundance of active sites on their surfaces, and tunable metal–support interactions. When serving as the catalyst materials for surface photochemistry, metallic nanoparticles are more advantageous than bulk metals benefiting from their unique plasmonic properties. The densities of hot carriers at the metallic nanoparticle surfaces are substantially higher than those at the bulk metal surfaces due to the enhanced light absorption, making it possible to effectively drive photochemistry at much lower photon flux densities, even under continuous wave (CW) illuminations at intensities comparable to the solar irradiation [30]. In addition, the energy distributions of hot carriers in nanoparticles can be tuned over a broader energy range across the Fermi level than in bulk metals, owing to the unique tunability of plasmon resonance frequencies in metallic nanoparticles. Furthermore, the confinement by a nanoparticle may introduce interesting modifications to the electronic states of the metal–adsorbate complexes, further enhancing our capability to improve the reactivities of molecular adsorbates by fine-tuning the metal–adsorbate interactions.

The radiative photon scattering and nonradiative Landau damping, discussed above, are two intrinsic plasmon decay pathways regardless of the local environment surrounding the photoexcited nanoparticles. When a molecular adsorbate or another material is in direct contact and strongly coupled with a metallic nanoparticle, the plasmons may decay through an alternative pathway known as chemical interface damping (CID) [6], [79]. CID involves the direct injection of electrons into unpopulated orbitals of the molecular adsorbates while leaving the holes in the metal (Figure 2e), which has been considered as a potentially more efficient charge-transfer channel than the indirect charge transfer following Landau damping [2], [6]. Direct adsorbate-to-metal electron transfer processes are often referred to as CID as well [80]. Analogous to CID in coupled plasmon–molecule systems, decay of a plasmon by directly exciting an electron from a metal to a strongly coupled semiconductor has also been observed in Au–CdSe heteronanostructures, a process also known as plasmon-induced interfacial charge-transfer transition (PICTT) [81]. By tuning the interactions between the Au and CdSe domains in the heteronanostructures, quantum efficiencies as high as

24 % can be achieved for the PICTT process, far exceeding those achievable through indirect charge transfer following Landau damping. The photocatalytic reactions induced by Landau damping and CID may have different quantum efficiencies, reaction selectivity, and kinetic features. Although the past few years have witnessed some research endeavors to delineate various nonthermal plasmonic effects on photocatalysis [82], [83], it is still challenging to unambiguously distinguish the Landau damping- and CID-mediated mechanisms in plasmon-driven photocatalytic reactions.

The photoexcited hot carriers that do not get extracted and involved in the surface photocatalytic reactions may dissipate their energies to the phonons of the metals and eventually reach the thermally equilibrated state over timescales ranging from ~100 ps to ~10 ns [11]. Such photothermal transduction delivers heat locally to the metal–adsorbate interfaces and deposits thermal energies into the vibrational modes of the molecular adsorbates [65], [84]–[86]. In this plasmon-mediated photothermal catalysis mechanism, the vibrationally excited adsorbates evolve along the potential energy surface of the ground electronic state without involving any charge-transfer processes (Figure 2f). As demonstrated by ample examples in the literature, both nonthermal hot carriers and photothermal heating can provide crucial contributions to the overall kinetic enhancements, even though it remains a significant challenge to quantitatively evaluate the thermal and nonthermal effects in plasmonic photocatalysis [52], [87]–[92].

3 Plasmon-driven bond cleavage in homonuclear diatomic molecules

Despite their seemingly simple structures, homonuclear diatomic molecules may undergo mechanistically complicated plasmon-driven dissociation reactions that exhibit interesting kinetic characteristics dictated by multiple photophysical and photochemical effects. Under thermal reaction conditions, it typically requires high energy costs to break the strong covalent bonds in diatomic molecules. Molecular adsorption to the surfaces of optically excited plasmonic nanostructures may lead to significant reduction of the activation energies for bond dissociation, triggered by injection of hot electrons into antibonding orbitals of the molecular adsorbates and/or the enhanced local fields at the nanoparticle surfaces (see schematic illustration in Figure 3). Here I discuss the mechanisms of plasmon-driven dissociation of three representative homonuclear diatomic molecular adsorbates, specifically H_2, O_2, and N_2, in the order of increasing bond energies and orders. Mechanistic insights gained from these homonuclear diatomic adsorbates form a knowledge foundation critical for understanding plasmon-driven bond cleavage in structurally more sophisticated molecules.

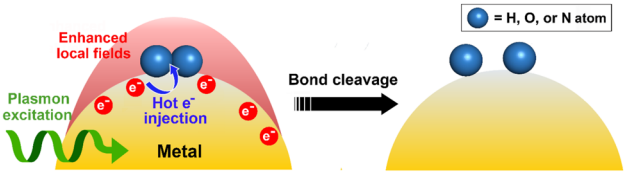

Figure 3: Schematic illustration of plasmon-driven bond cleavage in diatomic molecular adsorbates, such as H_2, O_2, and N_2, on a metal nanoparticle surface.

3.1 Plasmon-driven H_2 dissociation

H_2 represents the structurally simplest homonuclear diatomic molecule, in which the two H atoms are connected covalently through a single nonpolar σ bond with a dissociation energy of 436 kJ mol^{-1}. Although such an energy barrier appears exceedingly high to overcome in thermally driven chemical transformations, the activation energy of H–H bond cleavage can be significantly reduced with the aid of plasmon resonances. Halas and coworkers [93] discovered that plasmonic hot electrons photoexcited in Au nanoparticles could be transferred to the antibonding σ_u^* orbital of surface-adsorbed H_2, effectively triggering the H–H bond cleavage even at room temperature and atmospheric pressure. Because molecular H_2 exhibited negligibly low binding affinity to Au surfaces, the nanoparticulate Au photocatalysts were dispersed on TiO_2 supports (Figure 4a), which enhanced the interactions of H_2 molecules with Au surfaces to facilitate the transfer of hot electrons. The rate of H_2 dissociation was measured indirectly by monitoring the HD formation under continuous light illumination when exposing the Au/TiO_2 photocatalysts to a mixture of H_2 and D_2 (Figure 4b). While almost no H_2/D_2 dissociation was observed over bulk Au, small Au nanoparticles in the sub-10 nm size regime appeared catalytically active due to high abundance of atomically undercoordinated reactive sites on their surfaces. Although the production of HD was kinetically very slow in dark, a sharp increase in the rate of HD formation by 6-fold was observed when an Au/TiO_2 photocatalyst sample (1.75 wt % Au loading) was illuminated by a supercontinuum laser at a power density of 2.4 W cm^{-2} (Figure 4c). Under continuous laser illumination, the temperature of the photocatalyst substrate increased by ~5 °C due to photothermal heating, reaching a steady state

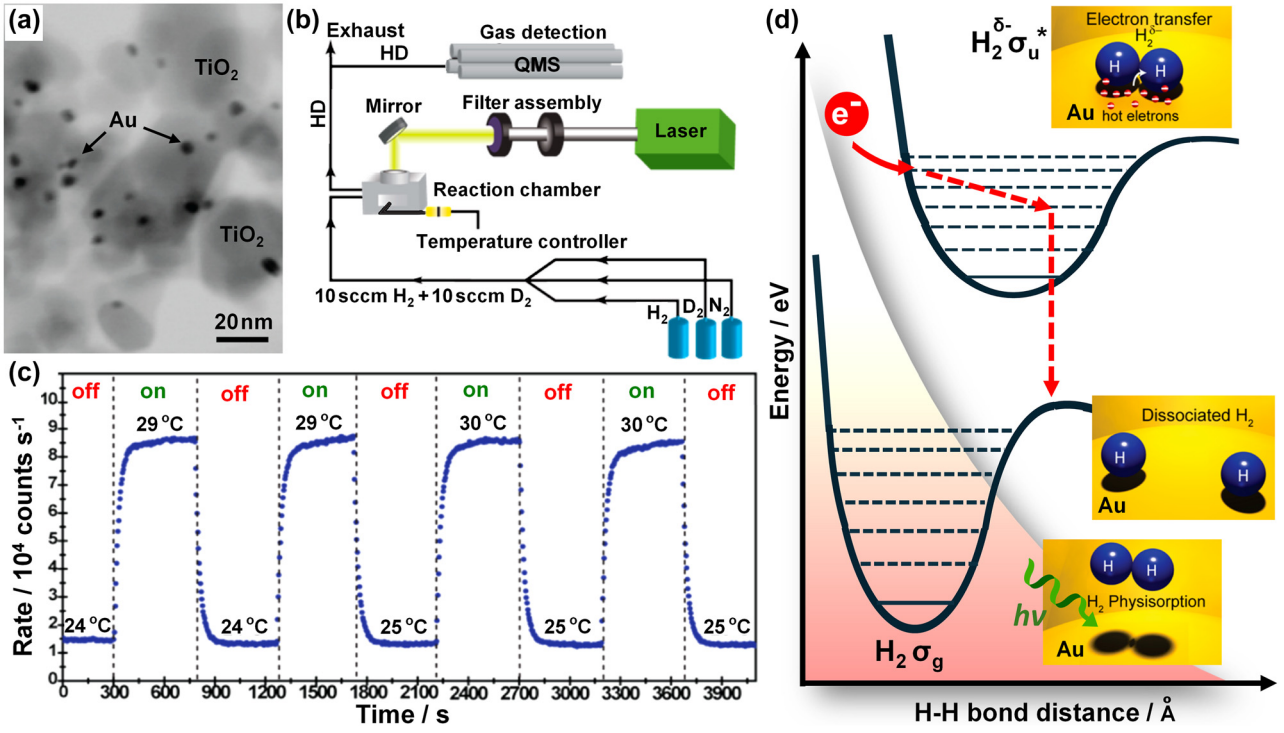

Figure 4: Plasmon-driven dissociation of H_2/D_2. (a) Scanning transmission electron micrograph showing distribution of Au nanoparticles over a TiO_2 support (1.75 wt % Au). (b) Schematic illustration of the experimental setup for kinetic measurements of plasmon-driven HD formation. (c) Real-time monitoring of rate with laser excitation (on, 2.41 W cm^{-2}) and without laser excitation (off). During 8 min of laser irradiation on the photocatalyst, the temperature increased by ~5 °C as shown in the figure. The dotted vertical lines indicate the laser on/off times. (d) Proposed mechanism of hot electron-induced H_2 dissociation on an Au nanoparticle surface. Adapted from ref. [93]. Copyright 2013 American Chemical Society.

temperature around 29–30 °C within a few minutes. When the laser was switched off, the rate of HD formation reverted to its initial value in dark, clearly showing that this reaction could be kinetically modulated by light in a reversible manner.

A series of experimental observations coherently suggested that the photocatalytic dissociation of H_2 and D_2 on Au/TiO_2 catalysts was essentially driven by photoexcited hot carriers in the Au nanoparticles. First, the rate of photocatalytic HD formation depended sensitively on the sizes and coverages of Au nanoparticles on the TiO_2 support, whereas pristine TiO_2 without Au nanoparticles under the same experimental conditions showed negligible photoenhancement in HD production rate [93]. A fraction of photoexcited energetic hot electrons might overcome the Schottky barrier at the Au/TiO_2 interface (0.9–1 eV) to get injected into the TiO_2 matrix, which reduced the number of hot electrons utilizable for the H_2/D_2 dissociation. When changing the support material from semiconducting TiO_2 to entirely insulating SiO_2, the rate of photocatalytic HD formation increased dramatically by two orders of magnitude, further verifying that the photodissociation of H_2/D_2 was indeed caused by hot electron injection into the surface-adsorbed H_2/D_2 [94]. Second, at a constant reaction temperature, the rate of HD formation exhibited a linear dependence on the photon flux density, which was a kinetic signature of hot carrier-driven photochemical reactions [93], [94]. Third, keeping the reaction temperature the same, photothermal processes gave rise to substantially higher reaction rates and yields than those achievable through thermal heating in dark, which verified the crucial roles of nonthermal hot carriers in catalyzing the dissociation of H_2/D_2 [93], [94]. Fourth, the photocatalytic action spectra (excitation wavelength dependence of reaction rate) matched the spectral profiles of light absorption by the Au nanoparticles very well [93], [94], indicating a direct correlation between H_2/D_2 dissociation rate and hot electron abundance in Au nanoparticles. Density functional theory (DFT) calculations revealed that as an H_2 molecule approached the Au surface, both the bonding $1\sigma_g$ and the antibonding $1\sigma_u^*$ orbitals of H_2 downshifted in energy due to the Au–H_2 interactions. The energetically down-shifted $1\sigma_u^*$ state became hybridized with the conduction band electrons in Au, yielding a partially occupied antibonding $1\sigma_u^*$ state [93]. On the basis of the experimental observations and the computational results, a hot electron-driven reaction mechanism was proposed. As

schematically illustrated in Figure 4d, photoexcited hot electrons in the high energy tail of nonequilibrium Fermi–Dirac distribution got transferred into the $1\sigma_u^*$ state of surface-adsorbed H_2, producing a transient negative ion, $H_2^{\delta-}$, with significantly elongated the H–H bond. After releasing an electron back to Au, the $H_2^{\delta-}$ intermediate relaxed to the potential energy continuum of the neutral H_2 in excited vibrational states, eventually leading to the H–H bond dissociation. The seminal work published by Halas and coworkers [93], [94] clearly demonstrated the feasibility of harvesting plasmonic hot electrons to trigger bond cleavage in H_2 molecules. However, several critical aspects concerning the detailed reaction mechanisms remained open to further investigations.

Although plasmonic hot electrons were identified as the primary driving force for the H_2 dissociation, the reaction rate was also significantly influenced by the photothermal effects. A simple experimental approach widely utilized to distinguish the nonthermal and thermal contributions to plasmonic photocatalysis is to measure the dependence of reaction rate on the power of excitation light [95], [96]. In the case of a photocatalytic reaction driven solely by hot carriers, the reaction rate is expected to be linearly proportional to the excitation power under moderate CW illumination. In contrast, the rate constant of a dark reaction under thermal conditions should typically follow an Arrhenius-type temperature dependence. Assuming that the temperature elevation is proportional to the excitation power in a photothermal process, the rate of a photothermally triggered reaction should exhibit an exponential dependence on the illumination power. When extracting mechanistic information from the excitation power dependence of reaction rate, however, caution must be taken because a seemingly linear power dependence may be alternatively fitted with the Arrhenius equation at almost the same level of satisfaction [95], [96]. To unambiguously distinguish the thermal and nonthermal effects, the excitation power must be varied across a statistically significant range to ensure that the reaction rate varies over multiple orders of magnitude, which is difficult to achieve experimentally in many cases.

Lack of detailed information about the local structures at the photocatalytically active surface sites has been another major barrier toward thorough mechanistic understanding. As exemplified by the plasmon-mediated photopolymerization, the hottest spots for plasmonic photocatalysis coincided with the highest local field enhancements on the surfaces of individual Ag nanoparticles [97]. On close-packed Au nanoblock arrays, the primary hot spots for photopolymerization were located within the nanoscale gaps between adjacent nanoblocks [98], where the local field enhancements were dramatically higher than those on individual nanoblocks. Whether the spatial distributions of hot spots for the plasmon-driven H_2 dissociation reaction follow the same rules of regioselectivity still remains an open question. Schatz and coworkers [99] conducted *ab initio* nonadiabatic molecular dynamics calculations to simulate the dissociation of H_2 into atomic H on metallic nanoparticles upon excitation by femtosecond laser pulses. When an H_2 molecule was located near the surface of a single Au nanoparticle, the wave-functions of H_2 and the nanoparticle became hybridized at chemically relevant separations. In the coupled metal–adsorbate system, the antibonding state of H_2 was only 1.48 eV above the Fermi level of Au, which suggested that visible light-excited hot electrons were energetic enough to get transferred from Au nanoparticles to the antibonding state of the H_2 molecules, resulting in a repulsive potential energy surface that promoted H_2 dissociation. When two Au nanoparticles of the same size were positioned close to each other to form a dimer, the abundance of hot electrons in the interparticle gaps became drastically higher than that achievable on individual nanoparticles benefitting from the enormous field enhancements in the interparticle hot spots. However, if the H_2 molecule was located at the center of the gap in a plasmonic dimer, dissociation was suppressed instead of being enhanced due to sequential charge transfer, which reduced the probability of electronic occupation in the antibonding state. An asymmetric displacement of the molecule in the gap restored the H_2 dissociation as the additional charge transfer was significantly suppressed due to symmetry breaking. Experimental demonstration of such reactivity tunability in plasmonic photocatalysis, nevertheless, remains challenging due to lack of capability to precisely control the spatial distributions of individual molecules in a plasmonic hot spot.

It remains unclear whether the injection of hot electrons into the antibonding orbital of surface-adsorbed H_2 occurs indirectly following Landau damping or directly through CID. Guo, Zhang, and coworkers [100] carried out computational investigations using a simple model composed of an H_2 molecule interacting with an Au_6 cluster. Time-dependent density functional theory (TDDFT) calculations revealed that the initial photoexcitation was primarily restricted to the metal, producing hot electrons in the Au_6 cluster. The results of quantum dynamics simulations suggested that the diabatic charge transfer states caused rapid bond dissociation in H_2, whereas no such molecular dissociation occurred in the diabatic hot electron states. The dissociation of H_2 occurred through multiple crossings from the hot electron states to the charge transfer states.

Although these computational results were highly suggestive of a reaction mechanism involving indirect hot electron transfer following Landau damping, the $H_2@Au_6$ model was too small to sustain any localized plasmon resonances and thus, unable to fully describe the photoexcitation, transfer, and relaxation of hot electrons in larger metal nanoparticles that were commonly utilized as plasmonic photocatalysts. The possible involvement of CID in the plasmon-driven dissociation of H_2 should certainly be taken into consideration in future computational and experimental investigations.

Hot carriers exploitable for photocatalysis can be created in metallic nanoparticles through two fundamentally different mechanisms, nonradiative decay of plasmons and direct photoexcitation of interband transitions. Choosing Al nanocrystals as a model materials system, Halas and coworkers [101] demonstrated that both intraband and interband hot carriers could be effectively utilized to drive the photocatalytic H_2 dissociation. Al nanocrystals with an average size of 100 nm exhibited two light absorption peaks around 460 and 800 nm, which could be assigned to the localized plasmon resonances and the interband transitions, respectively. Photoexcitation of interband transitions in Al by near-infrared light resulted in more efficient HD production even though the light absorption cross sections associated with interband transitions were smaller than those of the plasmon resonances. The interband hot electrons in Al were distributed approximately 1–1.5 eV above the Fermi level and were thus, energetic enough to get injected into the H_2 adsorbates to trigger the bond cleavage. More recently, Schatz and coworkers [102] compared the influence of plasmonic versus interband excitations on laser pulse-driven dissociation of H_2 adsorbed to octahedral Ag and Au nanoparticles through real-time TDDFT calculations. The computational results clearly revealed that plasmon excitation led to lower threshold light intensity for H_2 dissociation in the case of Ag nanoparticles, but in Au nanoparticles, interband excitations became photocatalytically more effective than plasmonic excitations. In Ag and Al nanoparticles, the plasmon resonances and interband transitions occur in well-separated spectral regions, and thus can be selectively excited by choosing appropriate excitation wavelengths. In nanoparticles made of other metals, such as Au, Cu, Pd, and alloys, however, plasmon resonances may get strongly dampened by interband transitions due to spectral overlap of the two photoexcitation processes [103]–[108]. How the interplay between plasmons and interband transitions modulates the photocatalytic behaviors of metallic nanoparticles is a fundamentally important topic well-worthy of further investigations.

3.2 Plasmon-driven O_2 dissociation

With a bond dissociation energy as high as 498 kJ mol^{-1}, the O=O double bond in molecular O_2 is even stronger than the H–H bond in H_2. Interestingly, molecular O_2 adsorbed on the surfaces of plasmonically excited metallic nanostructures can readily undergo photocatalytic dissociation even at room temperature and atmospheric pressure [2], [30], [109]. It was proposed that the plasmon-driven dissociation of O_2 was induced by injection of hot electrons into the antibonding π^* orbital of surface-adsorbed O_2 [2], [30], [109], a mechanism analogous to that of the plasmon-driven H_2 dissociation in many aspects. The dissociation of O_2 leads to the formation of atomic O on the nanoparticle surfaces, which rapidly oxidizes a variety of molecular substrates [109]. In the case of ethylene epoxidation, dissociation of O_2 was identified as the rate-limiting step [109].

Linic and coworkers [30] studied the kinetics of plasmon-driven ethylene epoxidation over Al_2O_3-supported Ag nanocubes as a function of excitation light intensity at different reaction temperatures. The photocatalytic rate exhibited a linear dependence on the light intensity up to 300 mW cm^{-2} but switched to a superlinear power dependence at higher excitation powers. The magnitude of the kinetic isotope effect, which was defined as the ratio between the reaction rates for the $O_2{}^{16}$ and $O_2{}^{18}$ isotopes, increased substantially when entering the superlinear power dependence regime. Both the linear-to-superlinear transition of power dependence and the enhanced kinetic isotope effect were the kinetic signatures of electron-driven photocatalytic reactions on metals. A third kinetic characteristic of plasmon-driven O_2 dissociation was that both the temperature and light intensity positively influenced the quantum yield of the photocatalytic reaction. At a constant temperature, the quantum yield remained essentially unchanged in the low excitation power regime until a substantial increase was observed upon transition from the linear to the superlinear regime. At a given light intensity, the quantum yield increased monotonically upon elevation of the operating temperature. All these experimental observations were highly suggestive of a hot electron-driven reaction mechanism. Injection of an electron into the antibonding orbital of surface-adsorbed O_2 led to the formation of a transient negative ion, $O_2{}^-$, which might lose an electron and evolve into neutral O_2 in excited vibrational states. The lifetimes of these excited vibrational states, typically on picosecond timescale, were substantially longer than the timescale of a bond vibration (several femtoseconds), enabling effective utilization of the vibrational energy gained by O_2 to overcome the activation energy barrier for the bond cleavage.

Within the framework of the proposed mechanism, the switch from the linear to superlinear power dependence could be interpreted as the consequence of transition from single-electron to multi-electron processes. In the low excitation power regime, the bond cleavage was initiated upon injection of a single electron into each O_2 adsorbate. In the high excitation power regime where superlinearity emerged in the power dependence, the probability of electronic excitation of an adsorbate already vibrationally excited from previous electron scattering events became substantially higher. Meanwhile, the kinetic isotope effect also became more pronounced because multiple electron-scattering events led to a larger discrepancy in the vibrational energy gained by the two isotopes. The proposed mechanism also captured the experimentally observed temperature dependence of reaction rate. At higher temperatures, the O_2 adsorbates, on average, required less energy gain in electron scattering events to overcome the activation energy barrier because of increased population of adsorbates in the excited vibrational states. In addition, the probability of gaining a specific number of vibrational quanta became higher if the molecule was initially in an excited vibrational state. Therefore, the photocatalytic rate exhibited an exponential dependence on the operating temperature at a constant excitation power.

Although the origin of the aforementioned kinetic features could be interpreted reasonably well in the context of the proposed hot electron-driven mechanism, recent experimental and computational investigations suggested an alternative reaction mechanism that did not involve hot carrier transfer [110]. Through rigorous comparison of the quantum yields, local field enhancements, and hot carrier densities across a broad range of nanoparticle sizes and excitation photon wavelengths, Christopher and coworkers [110] proposed that the plasmon-mediated O_2 dissociation over SiO_2-supported Ag nanoparticles was essentially triggered by the direct interactions of the O_2 adsorbates with the plasmonic near-fields on Ag nanoparticle surfaces rather than hot electron transfer or photothermal heating. The quantum yields for O_2 dissociation were experimentally measured as a function of excitation photon wavelength on three photocatalyst samples with average Ag particle sizes of 14.1, 27.4, and 48.6 nm (Figure 5a), respectively. Over all three photocatalyst samples investigated, the maximal quantum yields for O_2 dissociation were achieved when the Ag plasmons were resonantly excited within the wavelength range of 400–450 nm. The three samples also exhibited comparable quantum yields across the entire explored wavelength range. Finite difference time domain (FDTD) calculations were carried out to study the effects of particle size on the relative electric field enhancement at the Ag nanoparticle surfaces (Figure 5b) and the relative hot carrier density in Ag nanoparticles (Figure 5c). The calculated hot carrier density increased by ~2 orders of magnitude

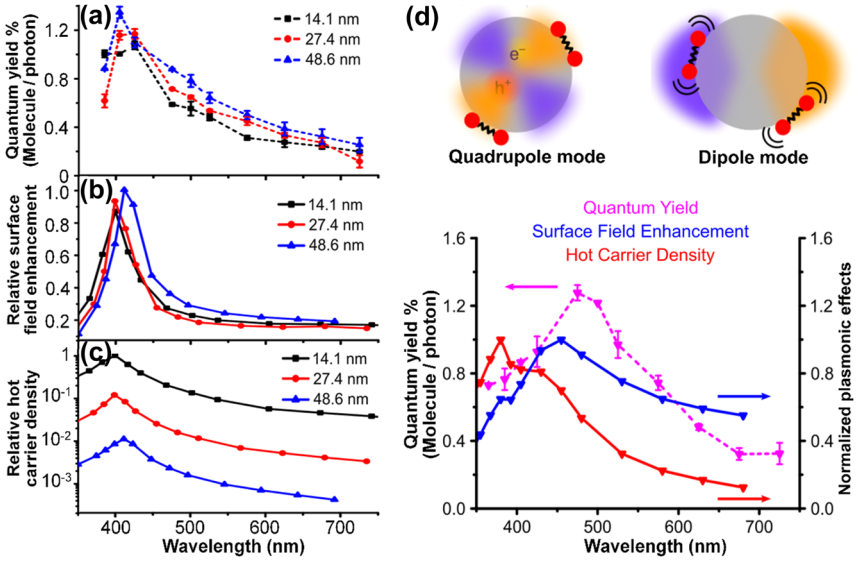

Figure 5: Plasmonic near field-triggered O_2 dissociation on Ag nanostructures. (a) Experimentally measured quantum yield for ethylene epoxidation on Ag nanoparticles with average sizes of 14.1, 27.4, and 48.6 nm. FDTD-calculated (b) relative surface field enhancement and (c) relative hot charge carrier density as a function of excitation photon wavelength for Ag nanoparticles with sizes of 14.1, 27.4, and 48.6 nm. The relative surface field enhancements and hot charge carrier densities were normalized to the highest value determined by FDTD calculations. (d) Excitation wavelength-dependent quantum yield for O_2 dissociation, surface electric field enhancement, and hot carrier density in 104.4 nm Ag nanoparticles. The schematic illustrations of the dipole and quadrupole plasmon modes are shown at top of panel (d). Adapted from ref. [110]. Copyright 2019 American Chemical Society.

when decreasing the particle size from 49 to 14 nm, deviating drastically from experimentally observed trend in the quantum yield for O_2 dissociation. However, the calculated surface field enhancements followed a trend consistent with the quantum yields, strongly suggesting that the plasmon-mediated O_2 dissociation was triggered by direct interactions of adsorbed O_2 with the enhanced local fields on Ag nanoparticle surfaces.

The direct correlation between plasmonic field enhancement and quantum yield for O_2 dissociation became more evident in the case of larger Ag nanoparticles beyond the quasi-static limit. Due to the phase retardation effect, Ag nanoparticles that were 104.4 nm in diameter exhibited extinction spectral features associated with both dipolar and quadrupolar plasmon resonances. The quadrupolar plasmon modes primarily led to photon absorption, whereas the light extinction at the dipole plasmon resonance frequencies was dominated by scattering. The electric field enhancement at the Ag particle surface trended with the longer-wavelength dipolar plasmon mode, whereas the density of hot carriers in Ag nanoparticles trended with the shorter-wavelength quadrupolar dark plasmon mode. As shown in Figure 5d, the wavelength-dependence of quantum yield matched the trend of relative surface field enhancement, deviating significantly from the trend of relative hot carrier density inside the Ag nanoparticles. Real-time TDDFT calculations further revealed that the local field enhancement played the major role in driving the O_2 dissociation reaction, while significant charge transfer was neither necessary nor sufficient for inducing bond cleavage in surface-adsorbed O_2 [111]. At the current level of mechanistic understanding, the local field-mediated mechanism appears more plausible than the hot electron-driven mechanism, even though multiple critical aspects concerning the detailed mechanisms still need to be further investigated.

3.3 Plasmon-driven nitrogen fixation

With a nonpolar and strong N≡N triple bond (dissociation energy of 941 kJ mol^{-1}), molecular N_2 is structurally stable and chemically inert. Even the cleavage of the first bond in N_2, which converts a N≡N bond into a N=N bond, requires an energy as high as 410 kJ mol^{-1}. The bond cleavage in N_2 molecules is crucial for the N_2 reduction and has been considered as the rate-limiting kinetic bottleneck of the entire nitrogen fixation process. Nitrogen fixation is an important chemical process through which molecular N_2, which constitutes 78 % of the atmosphere, is reduced and converted into ammonia, a noncarbon-based compound indispensable in industrial processes for synthesizing fertilizers, pesticides, and pharmaceuticals. Nitrogen fixation relies critically on the use of catalyst materials [112]–[115]. In biological systems, nitrogen fixation is effectively catalyzed by enzymes called nitrogenases under mild reaction conditions [116]–[118]. However, biological nitrogen fixation is far from being able to meet the industrial needs for large-scale synthesis of ammonia. The most widely utilized method for nitrogen fixation in industry has been the Haber–Bosch process, which converts H_2 and N_2 into ammonia using oxide-supported Fe-based catalysts at high temperature (300–500 °C) and pressure (100 atm). There have been tremendous research interests in searching for high-performance catalyst materials and optimization of the reaction conditions to reduce the energy cost required for the manufacturing processes [112]–[115], [119]–[121]. Photocatalytic nitrogen fixation provides a particularly attractive approach that enables sustainable ammonia synthesis in a simulated natural environment, i.e., at ambient pressure, at room temperature, in aqueous reaction media, and under solar irradiation [122]–[125].

Nitrogen fixation on the surfaces of catalyst materials can occur through either dissociative or associative reaction pathways (Figure 6a) [126]. In the dissociative pathway, the N≡N bond is completely broken before each individual N adatom gets hydrogenated on the catalyst surface, eventually producing two NH_3 molecules independently. In the Haber–Bosch process, the reaction proceeds along the dissociative pathway, which occurs at high reaction temperatures and pressures. Alternatively, catalytic nitrogen fixation can occur through the associative mechanism, which involves the conversion of the N≡N bond into the N=N bond, immediately followed by stepwise hydrogenation until ammonia is finally produced. In the associative distal mechanism, the N_2 molecule adsorbs to the catalyst surface in an end-on coordination mode. The two N atoms get hydrogenated in a sequential manner, which leads to the production of one ammonia molecule at a time. In the associative alternating mechanism, however, both N_2 atoms are hydrogenated simultaneously, forming two equivalents of ammonia from each N_2 molecule. Photocatalytic nitrogen fixation, in most cases, take places through the associative mechanisms, whereas the complete dissociation of N_2 into atomic N remains difficult to achieve due to the high energy cost required to fully break the N≡N bond.

Optically excited metallic nanoparticles exhibit unique capabilities to catalyze the dissociation of N_2 toward NH_3 production under mild conditions. The mechanism of plasmon-driven nitrogen fixation involves injection of hot electrons into the antibonding orbital of surface-adsorbed N_2, which causes weakening of the N≡N bond and triggers the bond dissociation process [49]–[51], [127]. Aikens and

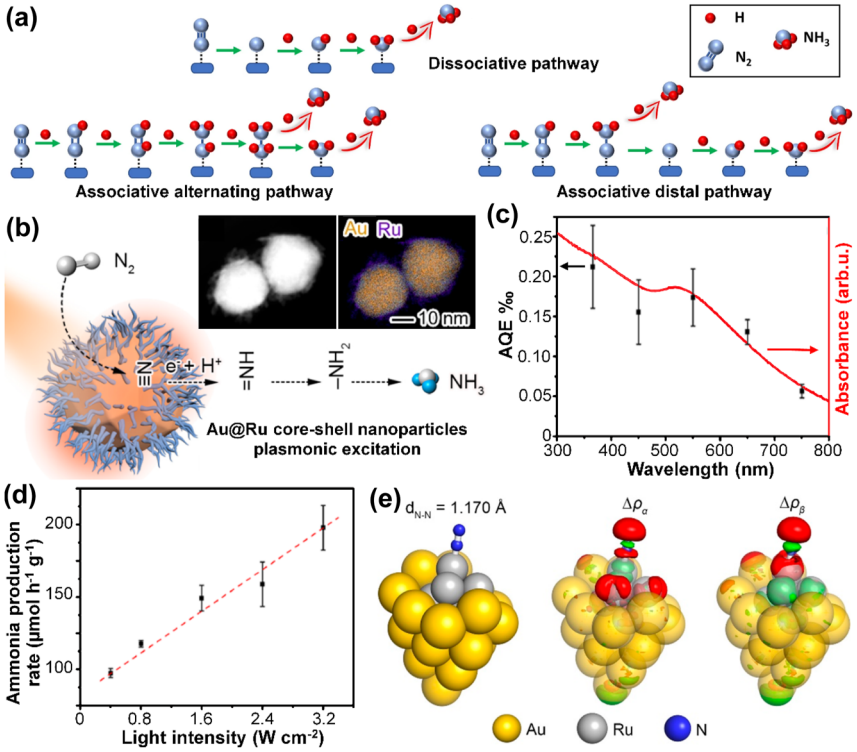

Figure 6: Plasmon-driven nitrogen fixation. (a) Schematic illustration of the dissociative and associative pathways of catalytic nitrogen fixation. (b) Schematic illustration of plasmon-driven N_2 dissociation on Au@Ru antenna-reactor nanostructures. The insets show a transmission electron microscopy image and energy-dispersive spectroscopy-based elemental mapping profiles of Au@Ru nanoparticles. (c) Apparent quantum efficiencies (AQEs) for N_2 fixation over Au@Ru nanoparticles in pure water under 20 mW cm^{-2} monochromatic light irradiation (black squares) and UV–vis extinction spectrum of colloidal Au@Ru nanoparticles (red line). (d) Rates of photocatalytic ammonia production in the first 2 h under different light intensities. (e) Optimized structures of N_2 adsorbed on $Ag_{22}Ru_6$ cluster, both charged by 1e and experienced with an electric field of 1.0×10^8 V m^{-1}. The electron density difference for α (spin-up) and β (spin-down) is normalized, and the absolute isovalue is set to 0.02. The red and green colors represent an increase and decrease in electron density, respectively. Panel (a), adapted from ref. [126]. Copyright 2023 Springer. Panels (b–e), adapted from ref. [127]. Copyright 2019 American Chemical Society.

coworkers [128] theoretically studied the bond dissociation of N_2 and H_2 adsorbed to an Ag_8 atomic wire using real time TDDFT, linear response TDDFT, and Ehrenfest dynamics. The computational results revealed that bond activation in diatomic molecular adsorbates was symmetry- and electric field-dependent. Dissociation of N_2 required higher electric field strengths than that of H_2. The bond dissociation of N_2 and O_2 triggered by plasmons in Au and Ag nanoparticles was compared theoretically by Montemore and coworkers [111], who found that both hot electron transfer and local-field enhancement played crucial roles in catalyzing the bond dissociation of N_2, whereas the local-field enhancement was the primary driving force for the dissociation of O_2. Although theoretically predicted to be feasible, plasmon-driven nitrogen fixation directly catalyzed by standalone Au and Ag nanoparticles has not been experimentally realized yet because N_2 exhibits intrinsically low binding affinity to Au and Ag surfaces, resulting in negligible plasmon–adsorbate interactions. When constructing plasmonic photocatalyst materials for nitrogen fixation, Au and Ag nanoparticles need to be combined with other materials, such as semiconductors [129], [130], platinum-group metals [127], [131], and metal–organic frameworks [132], to form multicomponent heterostructured nanocomposites. In these heterostructured photocatalysts, the plasmonic components, typically Au and Ag nanoparticles, serve as the sources of both hot carriers and local field enhancements, whereas the nonplasmonic components play a unique dual role, not only promoting the separation of the photoexcited charge carriers but also providing surface binding sites for N_2. In the past decade, plasmon-driven nitrogen fixation has attracted tremendous attention, and the latest progress in this research area, in terms of both materials development and mechanistic understanding, has been summarized by several recently published review articles [49]–[51].

Through plasmon-driven nitrogen fixation, it becomes possible to replicate the Haber–Bosch process by photocatalysis under mild and environmentally friendly reaction

conditions. To optimize the ammonia synthesis process and further accelerate the transition of this technology from laboratory to industrial-scale applications, the plasmonic photocatalysts must be deliberately designed such that they are able to efficiently absorb the solar light, generate highly energetic charge carriers, have extended excited state lifetime, and possess abundant surface sites for N_2 binding. Xiong and coworkers [127] used a plasmonic heteronanostructure composed of an Au nanoparticle coated with Ru nanowiskers as the photocatalyst to catalyze the dissociation of N_2 toward NH_3 production in pure water at 2 atmospheric pressure and room temperature (Figure 6b). The Au nanoparticles functioned as plasmonic nanoantennas and hot electron generators, while the Ru nanowiskers served as the catalytic reactors and binding sites for N_2. The photocatalytic action spectrum matched the absorption spectrum of the Au@Ru photocatalysis very well (Figure 6c), and a linear relationship between the reaction rate and the photon flux density was clearly observed under CW illumination within the power range experimentally investigated (Figure 6d). *In situ* spectroscopic studies using near ambient pressure X-ray photoelectron spectroscopy provided experimental evidence that N_2 was fully dissociated into surface-adsorbed atomic N at the early stage of the plasmon-driven nitrogen fixation process. First principles calculations were carried out to study the adsorption and plasmon-triggered dissociation of N_2 interacting with an atomic cluster composed of 22 Au atoms and 6 Ru atoms (Figure 6e). N_2 chemisorbed at Ru sites through an end-on configuration, forming a hybridized state that allowed plasmons to directly excite the charge carriers within the Au@Ru–N_2 complex to induce N_2 dissociation. The computational results also suggested that electron transfer alone without enhanced electric field only led to slight bond elongation in surface-adsorbed N_2 and could hardly dissociate N_2 molecules. Only when metal-to-N_2 electron transfer occurred in locally enhanced electric fields could the bond elongation and dissociation in N_2 become efficient. Another unique advantage of plasmon-driven nitrogen fixation is that the reactions occur in aqueous medium without the need to use pressurized H_2 as the reducing agent because water itself serves as the hydrogen donor. Through *in situ* Raman and infrared spectroscopic studies coupled with DFT calculations, Chi and coworkers [133] recently found that the efficiencies of plasmon-driven nitrogen fixation over branched AuCu alloy nanoparticles could be significantly improved by weakening the intermolecular H bonds in water and regulating the arrangement of water molecules at the catalyst–liquid interface. This work sheds light on the effects of interfacial assembly of water molecules on plasmon-driven photocatalysis, which appears to have been overlooked in the past. Plasmon-driven nitrogen fixation has so far been primarily focusing on ammonia synthesis, while direct synthesis of other value-added nitrogen fixation products, such as nitrate and nitrite anions, through plasmon-mediated photocatalytic nitrogen fixation still needs to be further explored.

4 Plasmon-driven bond cleavage in organic adsorbates

Built upon the knowledge gained from the homonuclear diatomic molecular adsorbates, I will further discuss how various plasmonic effects can be judiciously harnessed to selectively cleave certain types of chemical bonds in structurally more complicated organic molecular adsorbates. Instead of going through all bond-cleaving reactions ever reported in the literature, I will focus on several deliberately selected representative reactions to elucidate how the nature of the frontier molecular orbitals involved in electronic excitation and charge transfer processes and the local chemical environment at the metal–adsorbate interfaces determine the reaction pathways and chemoselectivity of plasmon-driven bond cleavage in organic molecular adsorbates.

4.1 Homolytic dissociation of dimethyl disulfide (cleavage of disulfur bond)

Cleavage of chemical bonds in small molecules, such as oxygen [71], [134], nitric oxide [135], carbonyl sulfide [135], and methyl bromide [136], can be effectively triggered by optical excitation of electronic transitions between the frontier molecular orbitals. Although these small molecules in the gas and liquid phases may undergo UV light-induced photodissociation reactions, they remain chemically stable under visible light illumination because the visible photons are energetically insufficient to excite the HOMO-to-LUMO electronic transitions. Strong plasmon–adsorbate interactions can create new photocatalytic reaction pathways that enable the use of visible light to pump the electronic transitions in small molecules, which drives bond cleavage in molecular adsorbates on metal surfaces. Kim and coworkers [137] discovered that when chemisorbed on single-crystalline Cu(111) and Ag(111) surfaces, dimethyl disulfide, $(CH_3S)_2$, underwent photodissociation reactions upon cleavage of the disulfur bond under visible light illumination. Although it has been known that adsorption of disulfur bond-containing molecules to metal surfaces may lead to destabilization or even dissociation of the S–S

bond [138], no $(CH_3S)_2$ dissociation was observed on the Cu(111) and Ag(111) surfaces at room temperature without light illumination. The mechanism of visible light-driven photodissociation of $(CH_3S)_2$ was found to be fundamentally different from those involved in plasmon-driven photodissociation of homonuclear diatomic molecules. The S–S bond dissociation was essentially driven by direct electronic excitation of the molecular adsorbates without involving any charge transfer between the metal and the molecular adsorbates. The strong metal–adsorbate interactions significantly narrowed the energy gap between the frontier molecular electronic states derived from the HOMO and LUMO of $(CH_3S)_2$ (Figure 7a), reducing the energy threshold for HOMO-to-LUMO electronic transitions from the UV to the visible range. In addition, the LUMO-derived molecular orbitals had negligible overlap with the metal surface, keeping the lifetimes of the photoexcited state sufficiently long to induce photodissociation. The photodissociation of surface-adsorbed $(CH_3S)_2$ could be tracked one molecule at a time using scanning tunneling microscopy (STM). In the STM measurements, the $(CH_3S)_2$ molecules were chemisorbed to an Ag (111) or Cu (111) surface, and an Ag tip with a curvature radius of ~60 nm was placed at a certain distance from the metal surface (Figure 7b). At a sample bias voltage (V_s) of 20 mV and a tunneling current (I_t) at 0.2 nA, each $(CH_3S)_2$ molecule appeared as an elliptical protrusion in the STM images. Each elliptical protrusion was transformed into two identical ball-shaped protrusions (Figure 7c) once the $(CH_3S)_2$ molecule was dissociated into two CH_3S molecules on the metal surface under visible light illumination.

The visible light-driven photodissociation of $(CH_3S)_2$ could be kinetically modulated by adjusting the distance between the STM tip and the metal surface [139]. As the Ag tip moved closer to the metal surface, the localized plasmonic field near the metal surface became increasingly more intense, resulting in further increased photodissociation rates. When the tip–substrate gap size was reduced to 1 nm, the plasmon-induced dissociation became kinetically very fast due to strong local field enhancements in the gaps. The yield of $(CH_3S)_2$ dissociation induced by localized plasmon resonances (Y_{LSP}), which was defined as the first-order rate constant divided by the photon flux density, exhibited wavelength-dependent profiles (Figure 7d) well-correlated to the calculated plasmonic field enhancements in the tip–substrate gaps (Figure 7e). The values of photodissociation yield (Y_{photon}) measured when the tip was retracted by more than 2 μm from the metal surface were

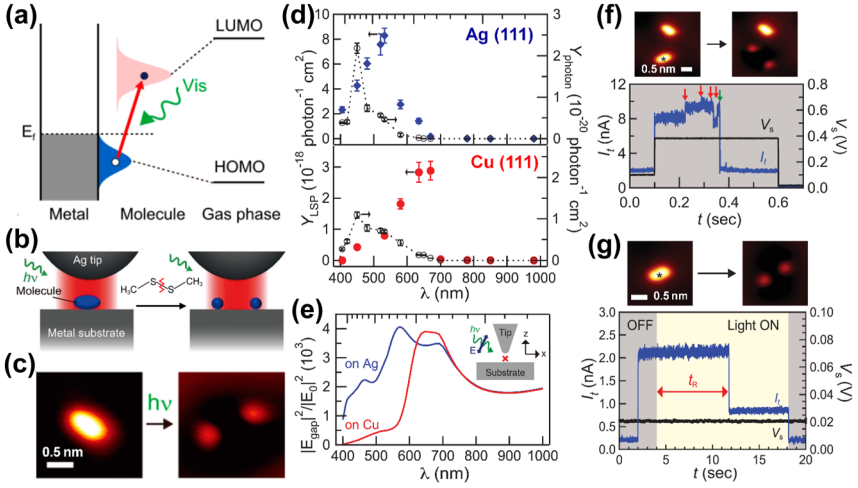

Figure 7: Plasmon-mediated cleavage of S–S bond in surface-adsorbed $(CH_3S)_2$. (a) Mechanism of visible-light-induced photodissociation of $(CH_3S)_2$ on metal surfaces through direct HOMO-to-LUMO excitations. (b) Schematic illustration of plasmon-induced S–S bond dissociation in $(CH_3S)_2$ in a gap between a metal surface and an STM tip. (c) Topographic STM images of a $(CH_3S)_2$ molecule on an Ag(111) surface observed at ~5 K ($V_s = 20$ mV and $I_t = 0.2$ nA) before and after irradiation with 532 nm light (5.86×10^{16} photons cm^{-2} s^{-1}) for 10 min. (d) Wavelength dependence of Y_{LSP} of $(CH_3S)_2$ molecules on Ag(111) (blue diamonds) and Cu(111) (red circles). The photodissociation yields without the excitation of plasmons, Y_{photon}, (black circles) are also shown. (e) Calculated electric field intensity for a 1-nm gap between an Ag tip and the metal substrates under *p*-polarized light. The simulated point is $z = 0.1$ nm above the substrate surfaces and $x = 0$ nm. (f) Current trace for detecting the dissociation of a target molecule in dark induced by inelastic electron tunneling (tunneling conditions: $V_s = 0.38$ V and $I_t = 8.0$ nA). The current changes indicated by red and green arrows correspond to rotation and dissociation, respectively. (g) Current trace for detecting the dissociation event for a target molecule on Ag(111) upon plasmonic excitation by p-polarized light at 532 nm (~2.7×10^{15} photons cm^{-2} s^{-1}). The Ag tip was positioned above the molecule marked by the asterisk in the STM image. t_R refers to the time required for the plasmon-induced dissociation. Panels (a) and (b), adapted from ref. [137]. Copyright 2017 American Chemical Society. Panels (c–g), adapted from ref. [139]. Copyright 2018 American Association for the Advancement of Science.

approximately two orders of magnitude lower than those of Y_{LSP} (Figure 7d) due to diminished field enhancements in the large gaps. In striking contrast to the action spectra of Y_{LSP}, the wavelength dependence of Y_{photon} well-reflected the densities of states of the HOMO and LUMO rather than the plasmonic field enhancements. DFT calculations revealed that in the coupled $(CH_3S)_2$–Ag(111) and $(CH_3S)_2$–Cu(111) systems, the HOMO- and LUMO-derived molecular orbitals consisted of the nonbonding lone pair–type orbitals on the S atoms (n_S) and the antibonding orbital localized at the S–S bond (σ^*_{SS}), respectively. The experimental observations and computational results strongly indicated that molecular dissociation under visible light illumination was driven by plasmon-enhanced n_S-to-σ^*_{SS} electronic excitations in the $(CH_3S)_2$ adsorbates rather than metal-to-adsorbate transfer of plasmonic hot electrons. The cleavage of the S–S bond was essentially caused by the dissociative potential energy surface of the neutral $(CH_3S)_2$ adsorbate in its excited states formed by the direct intramolecular excitations.

As exemplified by the previously discussed cases of H_2 and O_2, molecular dissociation can also be initiated by injecting electrons into molecular adsorbates to produce transient anionic intermediates. Inelastic electron transfer may lead to vibrational or electronic excitations of the molecular adsorbates, resulting in molecular rotation and dissociation that can be tracked in real time at the single-molecule level using STM. In $(CH_3S)_2$ chemisorbed on the metal surfaces, the transient anionic states could be produced through an inelastic electron tunneling process by injecting tunneling electrons from the STM tip instead of the plasmonic hot electrons. Vibrational excitations of surface-adsorbed $(CH_3S)_2$ by inelastically tunneled electrons led to rotation of $(CH_3S)_2$ before the molecular dissociation eventually occurred. Stepwise changes in I_t, a unique feature signifying the rotation of surface-adsorbed $(CH_3S)_2$, was clearly observed at the single-molecule level until the S–S bond was finally dissociated, which was reflected by an irreversible sudden drop in I_t (Figure 7f). The transient anionic state of $(CH_3S)_2$, which was featured by a nondissociative potential energy surface, relaxed to vibrationally excited states to trigger the S–S bond dissociation. Interestingly, such molecular rotation events were not observed prior to the S–S bond cleavage in plasmon-mediated $(CH_3S)_2$ photodissociation processes (Figure 7g), strongly implying that neither direct nor indirect transfer of plasmonic hot electrons was the primary driving force for the photodissociation of $(CH_3S)_2$ adsorbates. The results of DFT calculations also revealed that the LUMOs of $(CH_3S)_2$ were only weakly hybridized with the metal states, which suppressed the relaxation of the excited state and thus made the dissociative potential energy surface of the excited state more accessible. In contrast, the molecular orbitals of O_2 and H_2 adsorbates were more strongly hybridized with metal substrates, which promoted the release of electrons from the anionic intermediates to the metal substrates. Therefore, plasmon-driven dissociation of O_2 and H_2 occurred through a fundamentally different pathway involving vibrational excitations of the molecular adsorbates induced by transient transfer of plasmonic hot electrons. In addition to energetic alignments between adsorbate orbitals and metal states, the degree of hybridization between molecular orbitals and metal states is obviously another determining factor for the pathway selection of plasmon-mediated bond cleavage in molecular adsorbates.

4.2 N-Demethylation of methylene blue (cleavage of carbon–nitrogen bond)

In the case of plasmon-mediated $(CH_3S)_2$ dissociation, the strong chemisorption of $(CH_3S)_2$ to Ag and Cu surfaces narrows the energy gap between the HOMO- and LUMO-derived molecular orbitals, shifting the energies of HOMO—LUMO transitions from the UV to the visible region. However, such strong chemisorption is not necessarily a prerequisite for visible light-driven bond cleavage in molecular adsorbates. Some visible light-absorbing dye molecules may undergo chemoselective bond-cleaving reactions through plasmon-enhanced intramolecular excitations under visible light illumination even when they interact with metal surfaces through physisorption dominated by weak dispersion forces. One striking example is methylene blue (MB), which has a characteristic light absorption band in the wavelength range of 600–700 nm when dissolved in water. Because of the weak metal–adsorbate interactions, physisorption of MB on metal surfaces introduces rather limited spectral shift and line-shape modification to the intrinsic absorption band of MB molecules. Under visible light excitations, MB physisorbed to nanostructured Au surfaces may undergo plasmon-driven transformations to form either fully demethylated thionine or partially demethylated products, such as Azure B, Azure A, and Azure C (Figure 8a) [140]–[143].

Habteyes and coworkers [140]–[143] used SERS as an *in situ* molecular fingerprinting tool to precisely monitor the plasmon-driven N-demethylation of MB in real time. The SERS-based kinetic measurements were conducted at different excitation wavelengths on MB molecules physisorbed to the surfaces of a series of Au nanostructures, such as aggregated Au nanorods, aggregated Au nanospheres, and Au nanorods over Au thin films. The nanoscale gaps in

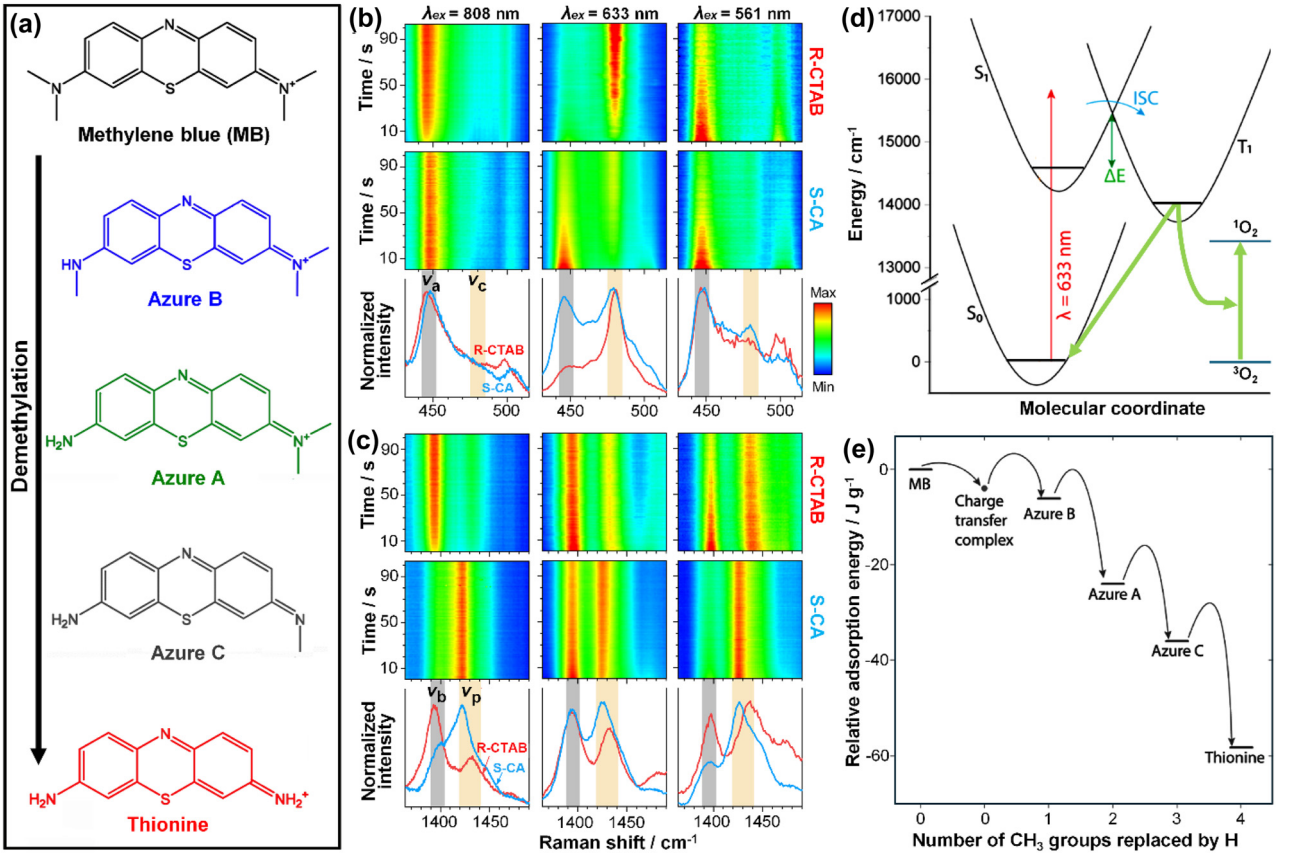

Figure 8: Plasmon-mediated demethylation of MB. (a) Molecular structures of MB and various partially and fully demethylated products. Time-resolved SERS spectra collected from MB adsorbed on (top panels) aggregated CTAB-coated Au nanorods (R-CTAB) and (middle panels) carboxylic acid-coated Au nanospheres (S-CA) at different excitation wavelengths in the Raman shift ranges of (b) 430–515 and (c) 1,364—1,490 cm^{-1}. The last SERS spectra included in the intensity maps are shown as the red (MB on R-CTAB) and blue spectra (MB on S-CA) in the bottom panels. The spectra are normalized to the same maximum. The peak labeled ν_c indicates the formation of thionine due to complete N-demethylation of MB. The peak labeled ν_a is used as a reference. The relative intensity and peak position of the mode labeled ν_p indicate partial N-demethylation and/or charge transfer, which are analyzed with reference to the peak labeled ν_b. (d) Scheme showing the mechanism of C–N bond cleavage in MB adsorbates through plasmon-enhanced intramolecular excitations. The plasmon near field of the particle pumps the $S_0 \rightarrow S_1$ electronic transition of the MB adsorbate. S_1 to T_1 intersystem crossing can populate the MB T_1 state, from which energy transfer can promote oxygen from its triplet ground state ($^3O_2$) to singlet excited state ($^1O_2$). The energy scale is derived from the absorption spectrum of the adsorbate. (e) Evolution of the adsorption energy per unit mass as the CH_3 groups in MB are removed and replaced by hydrogen atom during the stepwise N-demethylation reaction. Adapted from ref. [143]. Copyright 2020 American Chemical Society.

these nanostructures played a dual role as both the hot spots for SERS and the active sites for photocatalysis. The N-demethylation of MB was evidenced by intensity drop of the SERS peak at 449 cm^{-1} (C–N–C rocking vibrational mode of MB), emergence of new SERS peaks at 479 (the skeletal deformation of thionine) and 804 cm^{-1} (the NH_2 rocking vibration modes of thionine and partially demethylated MB with at least one of the N-terminals completely demethylated), and frequency downshift of the in-plane NCH bending mode initially at 1,435 cm^{-1}, which could be attributed to the formation of partially demethylated products. When the excitation energy overlapped with both the plasmon resonance of the metallic substrates and the HOMO-to-LUMO electronic transition energy of the MB adsorbates (excitation wavelength of 633 nm), the rate of photochemical conversion of MB to thionine reached the maximum. Detuning the plasmon resonance or the excitation energy away from the HOMO—LUMO transition energy of MB resulted in decreased reaction rates. Under illumination by a 633 nm CW laser, N-demethylation of MB on aggregated Au nanorods was clearly observed at an incident intensity as low as 10^2 W cm^{-2}. In contrast, excitation of MB adsorbed on an Au bulk film did not lead to any detectable N-demethylation even at an irradiation intensity of 10^5 W cm^{-2}, which underscored the crucial role of local field enhancements in pumping the electronic excitations of

adsorbates [140]. When the MB adsorbates were separated from the Au surfaces by a thin dielectric layer composed of poly(sodium 4-styrenesulfonate), the N-demethylation reactions was kinetically further enhanced instead of being suppressed, suggesting that the N-demethylation of MB did not require any charge transfer between the metallic photocatalysts and molecular adsorbates [140]. The rate of N-demethylation was observed to be sensitive to not only the photoexcitation conditions but the local chemical environment at the active sites as well [141]. MB adsorbed on nanostructured Au surfaces were observed to be highly reactive toward plasmon-mediated N-demethylation reactions in aqueous aerobic environments (under ambient air or in an O_2 atmosphere) but became completely inert in an N_2 atmosphere. Molecular O_2 adsorbed on nanostructured Au surfaces can be photoactivated by promoting oxygen from its triplet ground state ($^3O_2$) to singlet excited state ($^1O_2$), and MB is a well-established and extensively studied photosensitizer for $^1O_2$ generation [144]. Coupling MB or other photosensitizers, such as $[Ru(bpy)_3]^{2+}$ [145], to plasmonic nanostructures enables plasmon-mediated photogeneration of $^1O_2$. Interestingly, $^1O_2$ is a highly reactive species capable of initiating the oxidative N-demethylation of MB, an interesting plasmon-driven bond-cleaving reaction discovered by Habteyes and coworkers through *in situ* SERS measurements [140]–[143].

Besides N-demethylation of MB, plasmon-driven N-dealkylation reactions may also occur on Viologen derivatives. Frontiera and coworkers [146] observed that N-dealkylation reactions could be alternatively driven by anionic O_2^- radicals, which were produced upon injection of a plasmonic hot electron into the π^* orbital of surface-adsorbed O_2. Viologen derivatives, such as benzyl and ethyl viologen, underwent plasmon-mediated C–N bond cleavage to form 4,4′-bipyridine on nanostructured Au surfaces under near infrared excitations. Apparently, near infrared light was incapable of exciting any intramolecular electronic transitions in the viologen derivatives. The cleavage of the C–N bond in these viologen derivatives was proposed to be initiated by interactions of the transient O_2^- radicals with the nitrogen atoms, followed by extraction of hydrogen from the local water molecules on the Au surfaces. Therefore, both the plasmon-enhanced intramolecular excitations and metal-to-adsorbate transfer of plasmonic hot electrons may lead to the formation of photoactivated species that drive the chemoselective N-dealkylation of organic molecular adsorbates.

Although N-demethylation of MB was observed to be driven by plasmon-pumped intramolecular HOMO−LUMO transitions in the MB adsorbates, the possible involvement of charge transfer between Au nanoparticles and surface-adsorbed MB as an alternative reaction mechanism could not be ruled out solely based on those observations. Habteyes and coworkers [143] discovered that the surface-capping molecular ligands on Au nanostructure surfaces could be used as a unique knob to switch the reaction pathways of plasmon-driven N-demethylation of MB. Nanoparticle aggregates composed of two types of Au nanostructures, cetyltrimethyl ammonium bromide (CTAB)-capped Au nanorods (R-CTAB) and carboxylic acid-capped Au nanospheres (S-CA), were utilized as the plasmonic photocatalysts. After incubation of the Au nanostructures with MB in aqueous solutions, MB completely replaced the carboxylic acid ligands and became in direct contact with the Au surfaces, whereas CTAB coadsorbed with the MB molecules on the Au surfaces. As revealed by the results of *in situ* SERS measurements at various excitation wavelengths (Figure 8b and c), in the presence of CTAB ligands, MB was selectively transformed into the fully demethylated product, thionine, whereas MB directly adsorbed on the Au surfaces underwent nonselective N-demethylation reactions to produce thionine and a series of partially demethylated products. The reaction selectivity was intimately tied to the reaction pathways. In the presence of CTAB, the N-demethylation reaction was essentially driven by near field-enhanced intramolecular excitation of the MB adsorbate, resulting in the transition from the singlet ground state (S_0) to the singlet excited state (S_1), followed by intersystem crossing to the excited triplet state (T_1), as schematically illustrated in Figure 8d. The energy transfer from the T_1 state of MB to the triplet ground state of O_2 ($^3O_2$) led to the formation of reactive singlet oxygen O_2 ($^1O_2$), which interacted with MB to form a charge-transfer complex (exciplex) that selectively favored the complete demethylation of MB. The CTAB ligands not only promoted the plasmon-pumped $S_0 \rightarrow S_1$ electronic excitations by aligning the molecular dipoles along the plasmonic fields but also extended the excited state lifetimes by slowing down adsorbate-to-metal energy transfer. When MB was in direct contact with Au surfaces, the energy transfer to the metal surface caused shortening of molecular excited-state lifetime, making the $^1O_2$-mediated reaction pathway less accessible. However, the plasmonic hot electrons could be injected into the surface-adsorbed MB to produce a transient anionic complex, which subsequently underwent stepwise, nonselective N-demethylation. The stepwise N-demethylation process could be assisted by steric effect as the relatively bulky methyl groups were substituted by smaller hydrogen atoms during the N-demethylation reactions. As the N-demethylation proceeded, the molecular adsorption to Au

surface became increasingly more favorable as the steric hindrance caused by the bulky CH_3 groups was removed (Figure 8e). While the fully demethylated thionine represented the thermodynamically most stable product of the plasmon-driven N-demethylation reaction, several partially demethylated products could also be kinetically trapped and clearly identified by SERS during the reactions.

Both the reactivity of the MB adsorbates and the mechanisms for N-demethylation became drastically different when changing the chemical composition of the plasmonic photocatalysts from Au to Ag. Linic and coworkers [147], [148] found that MB molecules could interact with Ag nanocube surfaces through chemisorption to form strongly coupled Ag-MB complexes. By carefully analyzing the relative SERS intensities of anti-Stokes and Stokes peaks at 785 nm excitation, they found that the apparent temperature of MB vibrational modes was significantly elevated in comparison to the local nanoparticle temperature, which was hypothesized to be caused by direct electron transfer through CID at this excitation wavelength [148]. Surprisingly, injection of electrons into the MB adsorbates induced nonselective photodegradation or photodesorption of MB, a reaction fundamentally different from the N-demethylation of MB observed on nanostructured Au surfaces. At 532 nm excitation, no charge transfer between Ag and MB was observed according to the anti-Stokes and Stokes SERS features. However, MB transformed into thionine through plasmon-mediated N-demethylation, even though the authors misinterpreted the characteristic SERS features of thionine as the spectral signatures of MB, based on which they drew a seemingly incorrect conclusion that MB was photochemically inert under this reaction condition [147]. On Ag surfaces, the N-demethylation of MB appears mechanistically even more complicated than on Au surfaces, and many puzzling pieces concerning the detailed mechanisms are still open to further experimental and computational investigations.

4.3 Decarboxylation reactions (cleavage of carbon–carbon bond)

As exemplified by MB demethylation reactions, a plasmon-driven bond-cleaving process may occur along multiple reaction pathways. Another strikingly example is the plasmon-driven decarboxylation reaction, which may interswitch among multiple reaction pathways when changing the light illumination conditions or the local chemical environment at the metal–adsorbate interfaces. Thermally driven decarboxylation of aromatic monocarboxylic acids typically requires high reaction temperatures and relies critically on specifically designed catalysts [149]. The reaction selectivity and decarboxylation yields under thermal conditions remain low in many cases unless electron-withdrawing substituents are regioselectively introduced to the phenyl ring [150]. Plasmon-driven decarboxylation provides a unique means of efficiently utilizing photon energies to trigger chemoselective C–C bond cleavage in aromatic carboxylic acids under mild reaction conditions. For example, 4-mercaptobenzoic acid (4-MBA) chemisorbed on nanostructured Au and Ag surfaces can readily lose its carboxyl group to transform into thiophenol (TP) and release CO_2 under visible light illumination even at room temperature.

The initial discovery of plasmon-driven decarboxylation reactions dates back to the early 2000s when Michota and Bukowska used SERS to monitor the adsorption of 4-MBA onto roughened Au and Ag electrode surfaces [151]. They observed the emergence of two unexpected peaks centered at 998 and 1,020 cm^{-1} in the SERS spectra, which could not be assigned to any characteristic vibrational mode of 4-MBA. Interestingly, these two emerging SERS peaks were both the spectral signatures of in-plane ring breathing modes of mono-substituted benzene derivatives, suggesting that 4-MBA underwent decarboxylation reactions to produce TP on the light-illuminated electrode surfaces during the SERS measurements. Without recognizing the possible involvement of plasmon resonances, the decarboxylation reaction was initially proposed to be driven by the interactions of the deprotonated carboxylate group (COO^-) with the roughened metal surfaces, which was supported by the observed pH-dependency of the reaction rate (fast reaction in alkaline environments but almost no reaction in acidic environments). Zhao and coworkers [152] proposed an alternative explanation for the peculiar SERS features of surface-adsorbed 4-MBA, which involved chemical enhancement caused by interfacial charge transfer. They argued that the SERS peaks at 998 and 1,020 cm^{-1} should be assigned to the nontotally symmetric (b_2) modes of 4-MBA, which got selectively enhanced by charge transfer between 4-MBA and the metal surface. While the origin of the observed spectral features could be interpreted reasonably well in the context of metal–adsorbate interactions and charge transfer, detailed kinetic results obtained from *in situ* SERS measurements provided compelling evidence that the temporal spectral evolution of surface-adsorbed 4-MBA originated essentially from plasmon-driven decarboxylation of 4-MBA residing in plasmonic hot spots [153].

To gain further mechanistic insights, Yoon and coworkers [154] studied decarboxylation of 4-MBA located in gap-mode plasmonic hot spots at various excitation wavelengths under deliberately controlled reaction conditions.

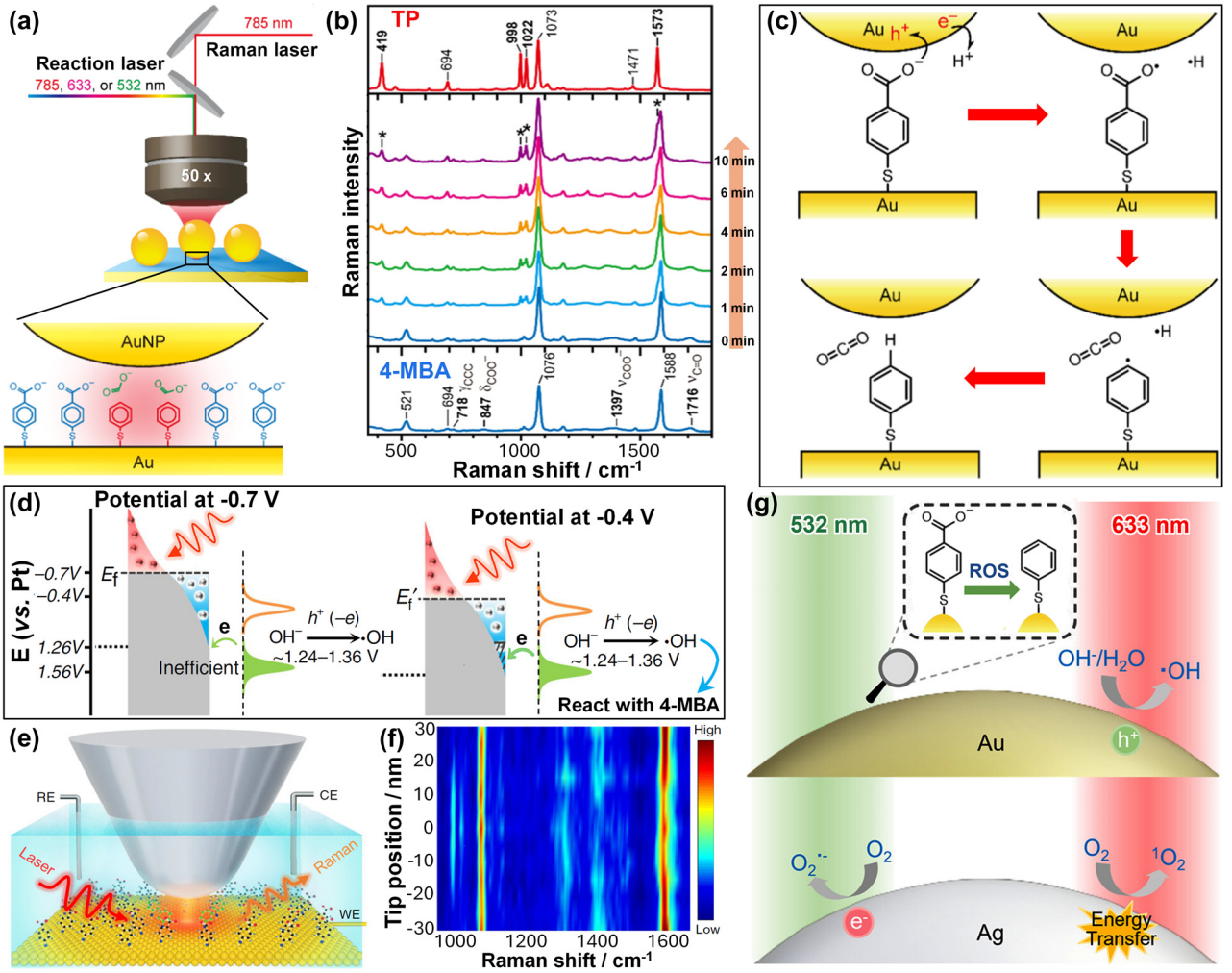

Figure 9: Plasmon-driven decarboxylation reactions. (a) Plasmon-driven decarboxylation of 4-MBA in a nanoscale gap of NPoM. An excitation laser (λ = 785, 633, or 532 nm) was focused on the NPoM structures through a 50× objective to induce the photocatalytic reactions and the reaction progress was monitored by SERS (785 nm excitation) using a Raman microscope. (b) SERS spectra at various reaction times during decarboxylation of 4-MBA at 785 nm excitations. The SERS spectra of the product (TP) and the reactant (4-MBA) are shown in the top and bottom panels, respectively. The asterisks highlight the characteristic peaks of TP. (c) Proposed mechanism of plasmon-driven decarboxylation of 4-MBA sandwiched between an Au nanoparticle and an Au substrate. (d) Effect of applied potential on the energy distribution (the Fermi–Dirac-like distribution after carrier relaxation) and transfer of plasmonic hot carriers. (e) Schematic illustration of the electrochemical tip-enhanced Raman spectroscopy (EC-TERS) setup, where the decarboxylation reaction is induced by gap-mode plasmons between the strongly coupled Ag tip and Au substrate. (f) Color-coded intensity map of the line-trace TERS spectra across a reaction region. The reaction was induced at the sample potential of −0.4 V under a laser (633 nm) power of 0.7 mW. The line-trace TERS spectra were acquired with the sample potential at −0.7 V. Bias: 100 mV, tunneling current: 800 pA. (g) Schematic illustration of plasmon-mediated decarboxylation of 4-MBA driven by photogenerated reactive oxygen species (ROS) at excitation wavelengths of 532 and 633 nm on Au and Ag nanoparticle surfaces. Panels (a–c), adapted from ref. [154]. Copyright 2019 American Chemical Society. Panels (d–f), adapted from ref. [164]. Copyright 2020 Nature Publishing Group. Panel (g), adapted from ref. [166]. Copyright 2024 American Chemical Society.

Au nanoparticles were placed on top of an Au substrate coated with a self-assembled monolayer (SAM) of 4-MBA to form a nanoparticle-on-mirror (NPoM) structure (Figure 9a). Under laser illumination, the 4-MBA molecules in the gap-mode hot spots underwent irreversible photocatalytic decarboxylation reactions, and the reaction progress could be tracked through *in situ* SERS measurements (Figure 9b). When the excitation laser was resonant with the plasmons (785 nm), the reaction rates and yields reached the maximum, whereas the decarboxylation reaction got kinetically suppressed when the excitation laser was off-resonant with the plasmons. This decarboxylation reaction could not be thermally activated by simply heating up the samples in dark and none of the visible and near infrared lasers used in this work had sufficiently high photon energies to excite any intramolecular electronic transitions in surface-adsorbed

4-MBA. Therefore, the primary driving force for this decarboxylation reaction was proposed to be the photoexcited hot carriers. Coating the Au nanoparticle surface with a thin layer of dielectric SiO_2 effectively blocked the interfacial transfer of the hot carriers and thereby completely inhibited the decarboxylation reaction, further verifying the hot carrier-driven reaction mechanism. As schematically illustrated in Figure 9c, the hot carriers in Au nanoparticles were generated from Landau damping, and subsequently transferred to reactant molecules in the hot spots to initiate the decarboxylation reaction. The acceptor of hot holes was identified to be the deprotonated 4-mercaptobenzonate rather than the protonated 4-MBA. Transfer of hot holes to the 4-mercaptobenzonate anions produced a reactive intermediate, carboxyl radicals, while the depletion of hot holes in the Au nanoparticles was compensated for by transfer of hot electrons to protons in water. Each carboxyl radical further underwent homolytic C–C bond cleavage to produce CO_2 and a surface-adsorbed mercaptophenyl radical, which rapidly combined with an atomic H to generate the final product, TP.

Using SERS as an *in situ* spectroscopic tool, Wang and coworkers [155] systematically studied the plasmon-driven decarboxylation of 4-MBA and 2-MBA adsorbates on a suprananostructure composed of a dielectric SiO_2 core (~1.0 μm in diameter) densely decorated with Ag nanocubes (~36 nm in edge length). These SiO_2@Ag suprananostructures executed unique dual-functions as both plasmonic photocatalysts and SERS substrates under near-infrared excitations (785 nm), with interstitial hot spots located in the nanoscale gaps between adjacent nanocubes. A series of critical insights concerning the detailed reaction mechanisms were gained through careful analysis of the *in situ* SERS results, further corroborated by DFT calculations. (1) The apparent decarboxylation rate increased with the local-field enhancement in the hot spots on the photocatalyst surfaces, as the surface abundance of hot carriers was positively correlated with local electric field intensity. (2) When the excitation laser power was varied within the range of sub-mW to mW, a superlinear dependence of reaction rate on the excitation power was observed. The elevation of local temperatures in the reactant-occupying plasmonic hot spots was measured by SERS employing TP as a Raman probe with intrinsic temperature-dependent SERS features. The results of the SERS-based nanothermommetric measurements revealed that photothermal heating had rather insignificant contribution to the kinetic enhancements under the experimental conditions explored in this work. Therefore, the superlinear power dependence of reaction rate observed in this case was essentially the hallmark of a hot carrier-driven reaction involving multiphoton absorption rather than a photothermally trigger reaction. (3) The maximal yield of TP achievable through the decarboxylation reaction (apparent reaction yield quantified based on the SERS spectra) was observed to decrease as the excitation laser power went down, becoming far below unity in the sub-mW power regime. Considering the irreversibility of this reaction, such excitation power dependence of the reaction yield suggested the existence of a threshold local-field intensity required for the plasmon-driven decarboxylation reactions. Only the molecular adsorbates occupying the hottest spots with local field intensities exceeding the threshold could be photoactivated for decarboxylation, while those residing in the colder regions remained essentially unreactive. (4) The pH-dependence of decarboxylation rate should not be interpreted simply in the context of protonation/deprotonation of the MBA adsorbates. Both the frontier orbital energies of the MBA adsorbates (hot hole acceptor) and the redox potentials of protons (hot electron acceptor) were pH-dependent and could be systematically tuned with respect to the Fermi level of Ag and the energy distribution profile of hot carriers. As a result, the kinetic profile exhibited a volcano-type dependence on pH, achieving maximal reaction rates and yields in weakly alkaline media within a pH range of 10–11. These mechanistic insights provided important guiding principles for rational optimization of both the plasmonic photocatalyst materials and the local chemical environment in which the decarboxylation reactions occur.

In addition to the irreversible spectral evolution caused by decarboxylation of 4-MBA, some transient spectral features might also emerge stochastically at additional vibrational frequencies in time-resolved SERS spectra [156]. While the spectral evolution reflecting the decarboxylation reactions could be analyzed by cross-correlation, the transient spectral events were found completely uncorrelated with each other. The probability of observing the uncorrelated stochastic events increased upon elevation of the excitation power and exhibited a superlinear dependence on the excitation power. The origin of the stochastic fluctuations observed in SERS is still poorly understood and whether these transient events can somehow influence the transfer of hot carriers across the metal–adsorbate interfaces remains a fundamentally intriguing open question.

A key factor limiting the utilization efficiency of hot holes for the photocatalytic decarboxylation reactions is the short lifetime of the energetic hot carriers photoexcited in the metallic nanostructures. Incorporation of electron-accepting coadsorbates to the plasmonic nanoparticle surfaces may promote the charge separation on the

nanoparticle surfaces, which leads to longer lifetimes of the hot carriers and more efficient transfer of hot holes into the MBA adsorbates. As a proof-of-concept, Lu and coworkers [157] demonstrated that choosing 4-hydroxythiophenol (4-HTP) as a coadsorbate could significantly accelerate the plasmon-driven decarboxylation of 4-MBA on Ag nanoparticle surfaces. At the excitation wavelength of 633 nm, the energy distribution of photoexcited hot electrons matched the LUMO level of the coadsorbed 4-HTP very well, which facilitated the transfer of the hot electrons from Ag to 4-HTP. Coadsorption of 4-HTP and 4-MBA on Ag nanoparticle surfaces could be achieved by incubating Ag nanoparticles with ethanolic solution containing both 4-HTP and 4-MBA. At a fixed 4-HTP/4-MBA molar ratio, increasing the incubation time resulted in more efficient decarboxylation of 4-MBA on Ag nanoparticle surfaces, suggesting that the spatial distribution of the adsorbate molecules over the nanoparticle surfaces might influence the hot carrier separation and the photocatalytic efficiency [158]. At short incubation times, the two types of molecular adsorbates might be intermixed on Ag nanoparticles, which represented a kinetically trapped metastable state. As the incubation time increased, the intermixed adsorbates might undergo thermodynamically driven phase segregation to form spatially separated 4-HTP and 4-MBA domains, which was found to be more favorable for the hot carrier separation on the Ag nanoparticle surfaces. The spatial distributions and interfacial dynamics of molecular adsorbates on metallic nanoparticle surfaces can be profoundly influenced by a series of factors, such as the chemical nature of metal–adsorbate interactions, the local surface curvature at the molecular binding sites, and the intermolecular interactions among adsorbates [159]–[163]. There is plenty of room to further optimize plasmon-driven photocatalysis by judiciously tailoring the surface chemistry of metallic nanostructures, especially when multiple types of molecular adsorbates are coadsorbed to nanoparticle surfaces.

While the decarboxylation reactions could be induced by transfer of hot holes from the Au to the MBA adsorbates, the photoexcited hot holes could also be utilized to produce reactive oxygen species (ROS) capable of initiating the decarboxylation reactions through an alternative reaction mechanism. Ren and coworkers [164] observed that photoexcited hot holes in Au could oxidize OH^- or H_2O to produce hydroxyl radical, OH·, which effectively drove the decarboxylation of 4-MBA adsorbates. In the presence of an OH· scavenger, tert-butanol, the plasmon-driven decarboxylation of 4-MBA could be completely inhibited. As illustrated in Figure 9d, the Fermi level of Au and the energy distributions of plasmonic hot carriers could both be shifted by applying an electrochemical potential on the Au photocatalysts. The hot holes with energies more positive than the oxidization potential of OH^- are considered reactive toward the production of OH·. Electrochemical tip-enhanced Raman spectroscopy (EC-TERS) was used as an *in situ* nanospectroscopic technique to correlate the detailed kinetic features of plasmon-driven decarboxylation reactions to precisely controlled energy distributions of plasmonic hot carriers. At an excitation wavelength of 633 nm, the fraction of reactive hot holes in Au increased significantly as the applied potential was shifted from −0.7 V to −0.4 V (vs. Pt), which effectively boosted the decarboxylation of 4-MBA adsorbates on Au surfaces. In the EC-TERS measurements, 4-MBA molecules were anchored on an Au (111) electrode surface through strong Au–S interactions to form a SAM and the electrochemical modulation of reaction kinetics was executed by applying a potential on the electrode. The strongly coupled plasmons between an Ag tip and the Au electrode were excited using a 633 nm CW laser, and TERS signals were collected in real time during the plasmon-driven reactions in an electrochemical cell (Figure 9e). The tip potential- and substrate potential-dependent experiments revealed that the decarboxylation of 4-MBA was primarily triggered by the hot carriers generated in the Au electrode rather than the Ag tip. When a potential of −0.7 V was applied to the Au electrode, 4-MBA appeared unreactive at an excitation power of 0.7 mW. However, a positive shift of the electrode potential by only 0.3 V led to rapid decarboxylation of 4-MBA at the same excitation power. The SERS features of TP were well-preserved when the potential was switched to −0.7 V, further verifying that the decarboxylation reaction was irreversible. Using EC-TERS as an imaging tool, the spatial distribution of plasmonic hot carriers on the Au electrode surface could also be fine-resolved with nanometer-scale precision. With the tip held at a fixed position, the substrate potential was first set to −0.4 V (vs. Pt) to induce the decarboxylation reaction. The plasmon-driven reaction was terminated by switching the electrode potential back to −0.7 V. In this way, the spatial distribution profiles of the product and reactant molecules could be mapped using TERS (Figure 9f) without further perturbing the reaction. Considering the hot hole-driven mechanism, the size of the reaction area may be determined by the spatial distribution of the reactive hot holes and the diffusion length of OH·. Based on the EC-TERS imaging results, the transport distance of the reactive hot holes was estimated to be ∼20 nm for the reactive hot holes that could overcome the energy barrier of about 1.66 eV for oxidation reaction. Hot holes with higher energies had shorter

transport distances, as further indicated by potential-dependent EC-TERS imaging results.

Besides OH· radicals, other ROS, such as O_2^- and $^1O_2$, could also induce the decarboxylation of MBA adsorbates. All these ROS could be produced through plasmonic hot carrier-driven reactions. Corio and coworkers [165] found that under illumination by a 633 nm laser, decarboxylation of MBA adsorbates on Ag and Au nanoparticle surfaces was primarily initiated by photogenerated $^1O_2$ and OH·, respectively. Energetic hot electrons in Ag nanoparticles could promote triplet-to-singlet transition from $^3O_2$ to $^1O_2$ *via* Dexter energy transfer, whereas energetic hot holes below the Fermi level of Au nanoparticles were capable of oxidizing OH^- to produce reactive OH·. Recent results reported by Qiu, Hao, and coworkers [166] not only confirmed Corio's findings but also further revealed the critical role of O_2^- in plasmon-driven MBA decarboxylation on Ag nanoparticles at the excitation wavelength of 532 nm (Figure 9g). The selective involvement of different types of ROS under various reactions was verified by control experiments using tert-butanol, *p*-benzoquinone, and furfuryl alcohol as the scavengers of OH·, $^1O_2$, and O_2^-, respectively. The decarboxylation of MBA regioisomers on Ag and Au nanoparticle surfaces driven by photogenerated ROS exhibited interesting regioselectivity [165]. Ag nanoparticles appeared active in catalyzing the decarboxylation for 4-MBA but exhibited almost no photocatalytic active toward decarboxylation of 2-MBA. In contrast, on Au nanoparticle surfaces, only 2-MBA molecules were decarboxylated at appreciable rates under the same reaction conditions. Such regioselectivity in plasmon-driven reactions was believed to originate from intricate metal–adsorbate, adsorbate–adsorbate, and adsorbate–environment interactions. The exact nature of these interactions and how these interactions contribute to the observed regioselectivity, however, are still open to further investigations.

4.4 Dehalogenation reactions (cleavage of carbon–halogen bonds)

Different from the oxidative C–C bond cleavage during decarboxylation of carboxylates, dehalogenation reactions involve reductive cleavage of carbon–halogen bonds in organohalogen molecules. Dehalogenation is a critical step in a large variety of organic reactions, such as the substitution, dissociation, and coupling reactions, through which halognenated organic compounds transform into other molecules with targeted functional groups in a chemoselective and regioselective manner. Photoexcited hot electrons in metallic nanoparticles can be judiciously harnessed to selectively activate the carbon–halogen bonds in halogenated thiophenol derivatives chemisorbed on metal nanoparticle surfaces. Through *in situ* SERS measurements, Xie and coworkers [167] observed that 4-iodothiophenol (4-ITP), 4-bromothiophenol (4-BTP), and 4-chlorothiophenol (4-CTP) adsorbates underwent dehalogenation reactions triggered by plasmonic hot electrons. As schematically illustrated in Figure 10a, plasmonic hot electrons in Ag and Au nanoparticles could be transferred to the LUMO of the adsorbate molecules to produce halogenated 4-thiophenol radicals. This anionic intermediate underwent rapid carbon–halogen bond cleavage to dissociate into a TP radical and a halide anion. The TP radical could either capture a hydrogen atom derived from protons or molecular water in the reaction medium to produce TP or undergo a bimolecular self-coupling reaction to generate 4,4′-biphenyldithiol (4,4′-BPDT). The progress of plasmon-driven dehalogenation reactions could be monitored in real time through SERS measurements. During the dehalogenation reactions, the intensities of the SERS peaks corresponding to vibrational stretching of the C–I, C–Br, and C–Cl bonds, which were centered at 1,055, 1,069, and 1,065 cm^{-1}, respectively, progressively decreased, while several new SERS peaks emerged at ∼1,000, ∼1,580, and 1,590 cm^{-1}, which were attributed to the phenyl ring deformation mode of TP, the ring stretching mode of TP, and the symmetric stretching mode of the phenyl ring in 4,4′-BPDT, respectively, became gradually more intense over time. Figure 10b shows the temporal evolution of the SERS spectra collected from 4-ITP on Ag nanoparticle surfaces at an excitation wavelength of 532 nm, from which the processes of both the C–I bond cleavage and the product formation could be well-resolved. In an aqueous reaction medium, the final products consisted of both TP and 4,4′-BPDT. Interestingly, the plasmon-driven dehalogenation reactions in a water-free environment led to the formation of 4,4′-BPDT as the sole product without any TP detectable by SERS, suggesting that the hydrogen source for TP formation was indeed from water. The plasmon-driven dehalogenation reactions could be further boosted by adding hole scavengers, such as Na_2SO_3 or ethanol, into the reaction medium, which further verified the hot electron-driven mechanism involved in the carbon–halogen bond cleavage. The reaction rates and yields on Ag nanoparticle surfaces were observed to be significantly higher than those achievable on Au nanoparticle surfaces because of stronger local field intensities and higher hot electron abundance on Ag surfaces.

The plasmon-driven dehalogenation reactions could be kinetically modulated by tuning the energies of the photoexcited hot electrons, which could be realized by applying a potential on Au photocatalysts. Xie and coworkers

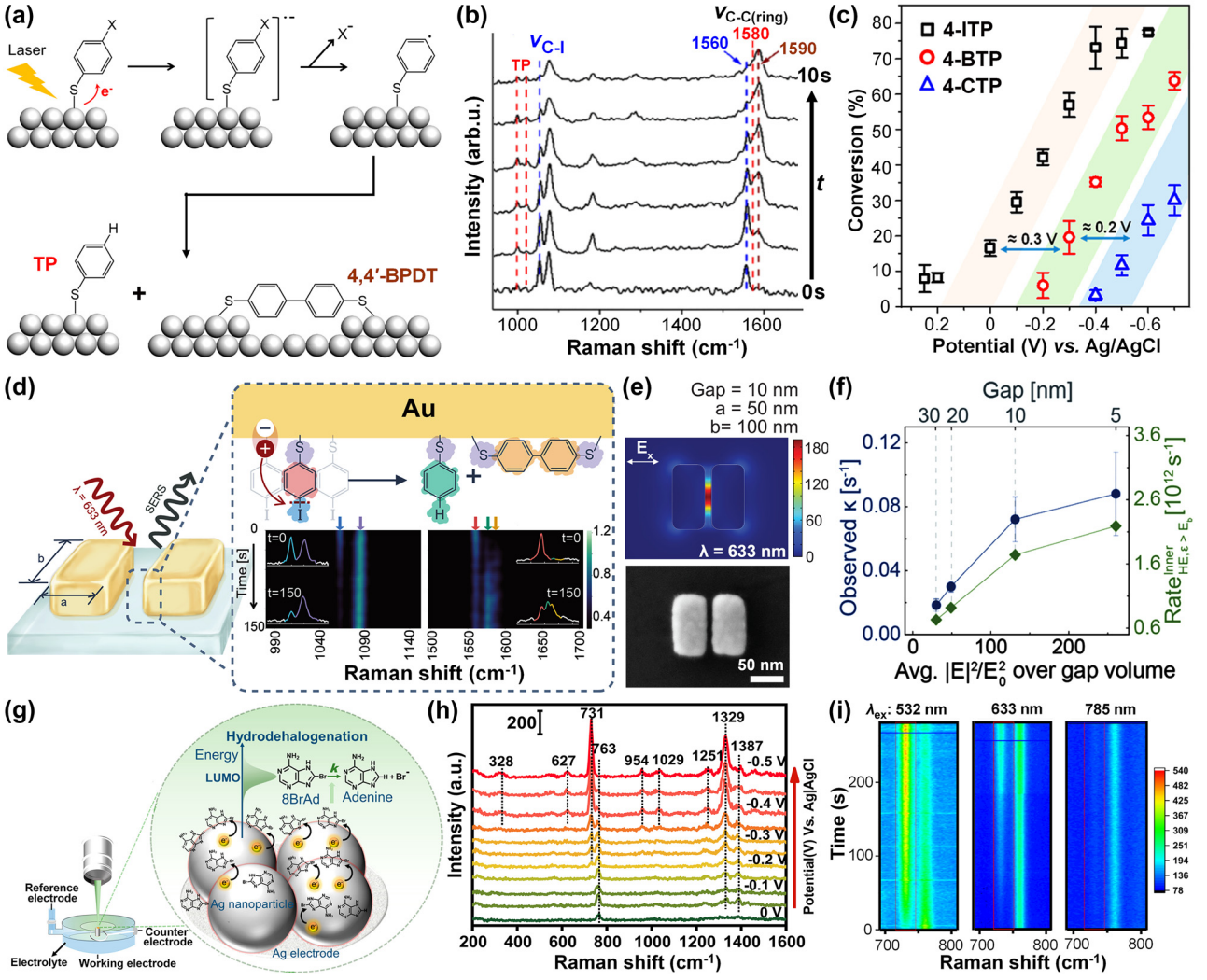

Figure 10: Plasmon-driven dehalogenation reactions. (a) Hot electron-driven reaction mechanism of C–X (X = F, Cl, Br, or I) bond dissociation in halothiophenol adsorbates on the Ag or Au nanoparticle surfaces under laser illumination. (b) *In situ* SERS spectra collected during dehalogenation of 4-ITP on the surfaces of Ag nanoparticles (80 nm in size) at an excitation wavelength of 532 nm and an excitation power density of 2.5×10^7 mW cm^{-2}. (c) Reaction yields of the hot electron-driven dehalogenation of 4-ITP, 4-BTP, and 4-CTP on the Au nanoparticles measured by EC-SERS (632.8 nm laser excitation with a power density of 1.25 mW μm^{-2}). The Au nanoparticles were supported by a glassy carbon electrode, to which an electrochemical potential was applied. (d) Schematic illustration of using *in situ* SERS to study photocatalytic dehalogenation of 4-ITP in a gap-mode nanoantenna composed of two parallelly aligned, brick-shaped Au nanorods. Dehalogenation process can be traced from decreasing Raman peaks of C–I bond (denoted in blue) and phenyl-ring (denoted in red) and increasing peaks of TP (denoted in green) and 4,4′-BPDT (denoted in yellow). The C–S peak (denoted in purple) is chosen as the reference. (e) Calculated field enhancement ($|E|^2/|E_0|^2$) map under the excitation by 633 nm *x*-polarized light (upper panel) and scanning electron microcopy image (lower panel) of an Au nanoantenna dimer. (f) Field enhancement dependency of the observed rate constant, *k*, and calculated hot-electron generation rate in the gaps of the Au nanoantenna dimers for hot electrons with energies exceeding 1.31 eV above the Fermi energy of Au. (g) Schematic illustration of using EC-SERS to study plasmon-driven debromination of 8-BrAd adsorbed on the Ag nanoparticle surfaces. (h) EC-SERS spectra of 8-BrAd adsorbates on Ag nanoparticle surfaces at an excitation wavelength of 532 nm (laser power is 0.1 mW) with a collecting time of 2 s at different potentials from 0 to −0.5 V versus Ag/AgCl. (i) Temporal evolutions of EC-SERS spectra at 0.0 V versus Ag/AgCl at various excitation wavelengths and powers: 532 nm, 0.1 mW; 633 nm, 0.1 mW; 785 nm, 0.2 mW. Panels (a) and (b), adapted from ref. [167]. Copyright 2019 American Chemical Society. Panel (c), adapted from ref. [168]. Copyright 2022 American Chemical Society. Panels (d–f), adapted from ref. [171]. Copyright 2023 American Chemical Society. Panels (g–i), adapted from ref. [173]. Copyright 2020 American Chemical Society.

[168] used *in situ* electrochemical SERS (EC-SERS) to systematically investigate the kinetic features of plasmon-driven dehalogenation reactions on Au nanoparticles at controlled potentials. Only when the electrode potential was more negative than a certain threshold could the hot electrons became sufficiently energetic to get injected into the molecular adsorbates to induce the dehalogenation reactions. Shifting the potential to more negative values resulted in

higher fractions of reactive hot electrons, which further boosted the dehalogenation reactions. By analyzing the intensity evolutions of the C–I, C–Br, and C–Cl stretching peaks in the *in situ* EC-SERS spectra, the apparent rates and yields of the dehalogenation reactions could be quantified. As shown in Figure 10c, the threshold potential for the dehalogenation of halogenated thiophenol derivatives negatively shifted in the order of 4-ITP > 4-BTP > 4-CTP, strongly supporting the proposed hot electron-driven reaction mechanisms.

The relative reactivities of various halothiophenols observed in the EC-SERS measurements were intimately related to the strengths of the carbon–halogen bonds (bond energy decreased in the order of C–F > C–Cl > C–Br > C–I). On Ag nanoparticles, the rates of the dehalogenation reactions decreased in the order of 4-ITP > 4-BTP > 4-CTP, according to the *in situ* SERS results reported by Xie and coworkers [167], [168]. Surprisingly, it was observed by Schürmann, Bald, and coworkers [169] that on Au nanoparticle surfaces, the dehalogenation rates were similar among 4-BTP, 4-CTP, and 4-fluorothiophenol (4-FTP). X-ray photoelectron spectroscopy (XPS) measurements provided important information about the work functions and valence band states of isolated halothiophenol-capped Au nanoparticles in the gas phase. With an increasing electronegativity of the halogen, the effective work-function increased from 4.3 eV for 4-BTP to 5.1 eV for 4-CTP and 5.2 eV for 4-FTP, respectively. While the relatively low work function of 4-BTP favored the transfer of hot electrons, a high density of occupied electronic states close to the Fermi-energy was also required for efficient electron transfer. In 4-BTP-capped Au nanoparticles, the accessible initial states were very limited in the relevant energy range, thereby hampering the electron transfer from the Au nanoparticles to the adsorbed molecules. In contrast, the relatively high work functions of 4-CTP- and 4-FTP-capped Au nanoparticles were a major barrier hampering the electron transfer processes even though the densities of states close to the Fermi level were significantly higher in comparison to 4-BTP-capped Au nanoparticles. Therefore, both the electronic properties of the metal–adsorbate systems and the intrinsic chemical reactivity of the molecular adsorbates should be taken into careful consideration when optimizing plasmon-driven molecule transformations involving carbon–halogen bond cleavage.

When analyzing the rich kinetic information extracted from *in situ* SERS results, we should keep in mind that the overall SERS features are dominated by the spectroscopic signals from molecules residing in the plasmonic hot spots, which may only account for a tiny fraction of all molecular adsorbates over the entire photocatalyst surfaces. The molecular transformations observed in SERS-based kinetic measurements are primarily restricted to small volumes spatially confined within the reactive hot spots, whereas how the majority of the molecular adsorbates on the photocatalyst surfaces behave remains disguised. Molecules chemisorbed to metal surfaces through strong covalent interactions exhibit limited surface mobility during plasmon-driven reactions, resulting in drastic site-to-site deviations in molecular reactivities due to heterogeneous distributions of hot spots on the photocatalyst surfaces. As exemplified by the plasmon-driven debromination of 4-BTP adsorbates on closed-packed Au nanoparticles, 4-BTP molecules in the reactive hot spots (interparticle gaps) underwent rapid debromination reactions, whereas the majority of 4-BTP adsorbate molecules remained almost unreacted at the poorly reactive surface sites where the local field enhancements were limited [170]. Finite-difference time-domain (FDTD) simulations revealed that the apparent kinetic order of plasmon-driven debromination of 4-BTP probed by SERS might be uncorrelated with the real reaction order, which was concealed by the highly heterogeneous enhancement of Raman signals over the photocatalyst surfaces. However, the apparent reaction rates measured by SERS were found to be proportional to the underlying rate constants for the same substrate and excitation wavelength. The experimental results could be fitted with high accuracy using the Fractal-like kinetic model, which took the inhomogeneity of the SERS substrates into account using a time-dependent reaction coefficient.

To assess the impact of hot spots to the reaction kinetics at a higher level of quantitativeness, Cortés and coworkers [171] used *in situ* SERS to track the detailed molecule-transforming processes in individual gap-mode hot spots and further correlated the reaction kinetics to the hot electron generation as a function of gap size at the single hot spot level. Au nanoantennas with precisely controlled hot spot geometries, each of which consisted of a pair of parallelly aligned, brick-shaped Au nanorods, were fabricated using an electron beam lithography-based method. The plasmon-driven deiodination of 4-ITP on each Au nanorod dimer was chosen as a model reaction for detailed kinetics studies. Figure 10d illustrates the basic geometry of the Au nanoantenna and the transformation of 4-ITP into TP and 4,4′-BPDT during SERS measurements. For rigorous comparison, the dimensions of individual nanorods and the gap size in each nanorod dimer were carefully tuned to achieve varying local-field intensities in the hot spots while maintaining a similar level of geometric anisotropy and transversal resonant profile. As shown in Figure 10e, upon optical

excitation of the transverse plasmon mode by a polarized plane wave at 633 nm, the local field enhancements were confined within the interparticle gaps rather than located at the longitudinal ends of individual nanorods. Although unpolarized excitation light was used for the *in situ* SERS measurements, the hot electrons exploitable for photocatalysis were primarily derived from the transverse gap-mode plasmons at the excitation wavelength of 633 nm, while the influence of the longitudinal plasmon resonances could be neglected. When the gap size was tuned within the range of 5–30 nm, higher reaction rates were observed at smaller gaps due to more efficient generation of hot electrons. Aggregated Au nanoparticles also possess highly abundant interparticle gaps, which could serve as the hot spots for the plasmon-driven dehalogenation reactions. However, due to heterogeneous spatial distribution and broad size distribution of the gaps, analysis of the kinetic results became less straightforward, requiring the use of more complicated kinetic models, such as the fractal kinetic model. Benefiting from the precise control over gap sizes and the *in situ* SERS measurements preformed at single hot spot level, the observed kinetic features of the dehalogenation reactions on the lithographically fabricated Au nanorod dimers could be well described by a simple first-order rate law. It was found that the dehalogenation reactions were driven by intraband hot electrons with energies exceeding a certain threshold, which was defined as E_b. The values of E_b for a given metal–adsorbate system under certain photoexcitation conditions could be estimated through DFT calculations. As shown in Figure 10f, the observed rate constants were well-correlated to the calculated generation rates of reactive hot electrons in hot spots (intraband hot electrons over the Au surfaces facing the gap with energies higher than an E_b value of 1.31 eV above the Au Fermi level). Decreasing the gap size from 30 nm to 10 nm led to an increase of the dehalogenation rate by 4 times while the local field enhancements went up by only 1.7 times. Further reduction of the gap size to the sub-10 nm range did not improve the reaction rate significantly even though the local fields were further enhanced by another 2-fold, strongly suggesting that in such small gap regime, the contribution of the stronger local field enhancements might be compromised by the decreased surface areas of the plasmonic nanoantennas.

Besides the halothiophenols, brominated nucleobases adsorbed on Au and Ag nanoparticle surfaces may also undergo plasmon-driven dehalogenation reactions. In 2017, Schürmann and Bald discovered [172] that 8-bromoadenine (8-BrAd) transformed into adenine on the surfaces of Au and Ag nanoparticles when irradiated by CW lasers at excitation wavelengths of 532, 633, and 785 nm. The debromination process could be tracked in real time based on the temporal evolution of spectral features in SERS. Analogous to the plasmon-driven debromination of 4-BTP, the cleavage of the C–Br bond in surface-adsorbed 8-BrAd was initiated upon injection of a hot electron into 8-BrAd, which led to the formation of an anionic radical with a dissociative potential energy surface. Through EC-SERS measurements, Tian and coworkers [173] demonstrated that the energy distributions of hot electrons could be tuned with respect to the LUMO energy of surface-adsorbed 8-BrAd by varying either the potential applied to the Ag photocatalysts or the wavelength of the excitation laser (Figure 10g). At a fixed excitation wavelength, negative shift of the applied potential led to energetic uplift of the hot electrons, which kinetically boosted the cleavage of the C–Br bond in 8-BrAd (Figure 10h). At a fixed potential, increasing the energy of the excitation photons led to higher debromination rates and yields when 8-BrAd were adsorbed on the surfaces of aggregated Ag nanoparticles (Figure 10i).

In addition to 8-BrAd, brominated derivatives of other canonical nucleobases, such as bromocytosine, bromoguanine, and bromouracil, could also undergo plasmon-driven debromination reactions on Ag nanoparticle surfaces [174]. Although the overall reaction rate was initially proposed to be limited by the metal-to-adsorbate transfer of hot electrons, both Br^- and the nucleobase radicals were later found to be played crucial roles in hole deactivation, which ultimately determined the dehalogenation rate [175]. In certain circumstances, insufficient hole deactivation might become a kinetic bottleneck limiting the overall rate of the debromination reactions. While both Br^- and the nucleobase radicals exhibited favorable oxidation potentials toward hole reaction on Ag surfaces, their reactivities toward hole deactivation was compromised on Au surfaces [175]. It is particularly interesting that hot electrons photoexcited in an Ag nanoparticle could be transferred over several nanometers to drive the debromination of an 8-BrAd in double-stranded DNA oligonucleotides [176]. Using double-stranded DNA as an efficient electron-conducting linker, it became possible to utilize plasmonic hot electrons to selectively trigger the C–Br bond cleavage in a bromonucleobase that was not even directly adsorbed on the nanoparticle surfaces.

4.5 Other plasmon-driven bond-cleaving reactions in organic adsorbates

Besides the intensively investigated reactions discussed above, a diverse range of other plasmon-driven bond-cleaving reactions, including but not limited to N–H bond

cleavage in mercaptopyridine [177] and hypoxanthine [178], C–B bond cleavage in mercaptophenylboronic acid [179], C–N bond cleavage in *para*-nitrothiophenol [180], azo bond cleavage in 4,4′-dimercaptoazobenzene [181], O–O bond cleavage in hydrogen peroxide [182], [183], C–I bond cleavage in diaryliodonium salts [184], [185], C–H bond cleavage in aromatic methyl groups [186], and C–O bond cleavage in 1-phenoxy-2-phenylethane [187], allyl phenyl ether [188], and alkoxyamines [189], have also been reported in the literature. The experimental observations reported so far suggest that these reactions are primarily driven by either injection of hot carriers into the molecular adsorbates or plasmon-enhanced intramolecular electronic excitations. Although the plasmonic photothermal effects may contribute to the kinetic enhancement to a certain extent, none of these reactions can be activated by thermal heating alone without the aid of plasmon resonances. With in-depth and comprehensive understanding of the molecule-transforming mechanisms and plasmon–adsorbate interactions, plasmon-driven photocatalysis will ultimately become a precise and versatile molecule-scissoring tool for cleaving targeted chemical bonds in molecular adsorbates to achieve chemoselective reaction outcomes under mild reaction conditions.

5 Applications of plasmonic molecular scissors

The insights gained from detailed mechanistic studies of plasmon-driven molecular scission form a solid knowledge foundation crucial for rational design of catalyst–adsorbate hybrid systems for targeted applications. Here, I briefly showcase three noteworthy examples that successfully demonstrate the unique capabilities of optically excited plasmonic nanostructures to trigger the cleavage of specific chemical bonds in molecular adsorbates, which are transformative to technological innovations in drug release, surface coating, and polymer synthesis.

5.1 Plasmon-triggered molecular release

Metallic nanoparticles with chemically tailored surface functionalities and near infrared plasmon resonances have been of particular interest and widely utilized as nanocarriers for targeted delivery and controlled release of drugs. There are two general strategies for on-demand release of drugs from the plasmonic nanocarriers to targeted tissues or cells using deep penetrating near-infrared light as a stimulus. The first strategy involves optical excitations by pulsed lasers to generate high-energy hot electrons, which cause direct desorption of adsorbates from the nanoparticle surfaces [190]–[193]. The other strategy relies on the plasmonic photothermal effects, which may either weaken thermolabile noncovalent intermolecular interactions or thermally activate covalent bonds for cleavage [194]–[196]. Taking full advantage of plasmon-driven chemoselective bond cleavage in deliberately designed molecular constructs, Camden and coworkers [197] developed an alternative strategy for light-controlled molecular release that neither involved the use of pulsed lasers nor relied on the photothermal effect. This strategy was designed based on a well-studied plasmon-driven oxidative coupling reaction, in which *para*-aminothiophenol (pATP) chemisorbed to Au or Ag nanoparticle surfaces underwent bimolecular coupling to produce 4,4′-dimercaptoazobenzenethiol (DMAB) under moderate CW laser illumination [198]–[200]. A critical step at the early stage of the pATP coupling reaction involved the cleavage of the N–H bond in the amino group in pATP, which could be initiated upon either transfer of hot holes to surface-adsorbed pATP or injection of hot electrons into surface-adsorbed O_2. Interestingly, instead of being restricted to pATP, this plasmon-driven oxidative coupling reaction could also take place in other aminothiophenol derivatives [201], [202], in which one of the H atoms or both H atoms in the amino group were substituted by other functional groups. The bimolecular coupling between two adjacent aminothiophenol derivative adsorbates led to the release of the functional groups originally connected to the nitrogen atoms, followed by the formation of an azo bond.

The feasibility of the proposed strategy was demonstrated using Au nanoparticles as the nanocarriers and a fluorescent molecule, 1-pyrenecarboxylic acid (PyA), as a model molecular cargo for controlled release [197]. As schematically illustrated in Figure 11a, PyA was conjugated to pMA through the 1-ethyl-3-(3-dimethylaminopropyl) carbodiimide (EDC)/N-hydroxysuccinimide (NHS) coupling reaction to form N-(mercaptophenyl)pyrene-1-carboxamide (MPPC), which chemisorbed to Au nanoparticle surfaces through Au–S interactions. When illuminated by a 785 nm CW laser, the MPPC adsorbed on aggregated Au nanoparticles underwent a plasmon-driven oxidative coupling reaction to produce DMAB, which remained chemisorbed to the nanoparticle surfaces, while releasing PyA from the Au nanoparticle surfaces into the solution. The conversion of MPPC to DMAB on the nanoparticle surfaces could be tracked by *in situ* SERS measurements, in which three SERS peaks at 1,144, 1,390, and 1,443 cm^{-1} were identified as the spectral signatures of DMAB (Figure 11b). The release of PyA into the solution led to gradual increase

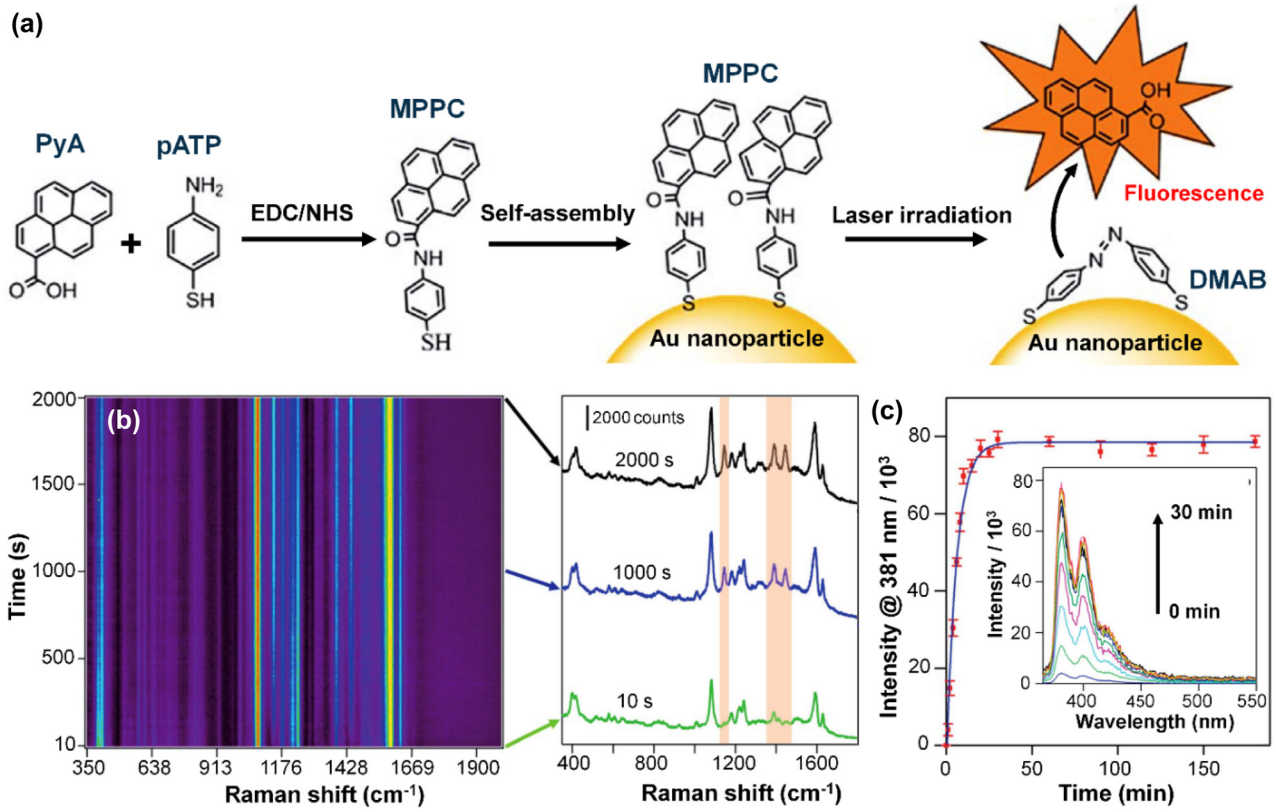

Figure 11: Plasmon-triggered release of molecular cargos from nanocarriers. (a) Scheme illustrating plasmon-triggered release of PyA *via* plasmon-driven oxidative coupling of MPPC on Au nanoparticle surfaces. (b) Temporally evolving SERS spectra collected from MPPC adsorbed on Au nanoparticles under continuous laser illumination (785 nm, 2 mW). The left panel shows the temporal evolution of the SERS spectra. The right panel shows the snapshot spectra collected at reaction times of 10, 1,000, and 2,000 s. (c) The fluorescence intensity (emission wavelength of 381 nm and excitation wavelength of 342 nm) of the supernatant solutions after irradiation (785 nm, 1–180 min) and centrifugation of the MPPC-functionalized nanoparticles. The inset shows the fluorescence spectra of the supernatant of the samples irradiated for between 1 and 30 min. Adapted from ref. [197]. Copyright 2017 The Royal Society of Chemistry.

of the fluorescence intensities in the aqueous solution (Figure 11c).

The facile EDC/NSH cross-linking method can be used as a robust and versatile synthetic tool to conjugate a large variety of targeted molecular cargos, such as drugs, nucleic acids, and proteins, to the amino group in surface-adsorbed host molecules, such as pATP. Therefore, the light-triggered molecular release based on plasmon-driven cleavage of the chemical bonds between the host and cargo molecules represent a particularly useful strategy for designing and constructing drug-nanocarrier systems for targeted biomedical applications.

5.2 Plasmon-mediated surface functionalization

The plasmonic properties of metallic nanostructures can be judiciously harnessed to drive on-surface photoreactions, providing a unique way to create targeted molecular moieties and functionalities on the nanostructured surfaces. Iodonium salts have been widely used as sources of aryl radicals, which serve as highly reactive intermediate species for surface functionalization of a large variety of solid-state materials [203]–[205]. The most widely adopted approaches for the surface functionalization with iodonium-derived compounds are based on either electrochemically induced grafting or chemical reduction processes [203]–[205], both of which have certain limitations and need further improvement. Postnikov, Lyutakov, and coworkers [184] developed an alternative, plasmon-mediated approach to the surface-functionalization of Au-coated optical fibers with targeted organic coating layers using iodonium salts as the precursors. This approach was essentially based on plasmon-driven homolytic cleavage of C–I bonds in iodonium salts followed by grafting of the *in situ* generated aryl radicals to Au surfaces. As illustrated in Figure 12a, the plasmon resonances sustained by an optical fiber coated with a thin layer of

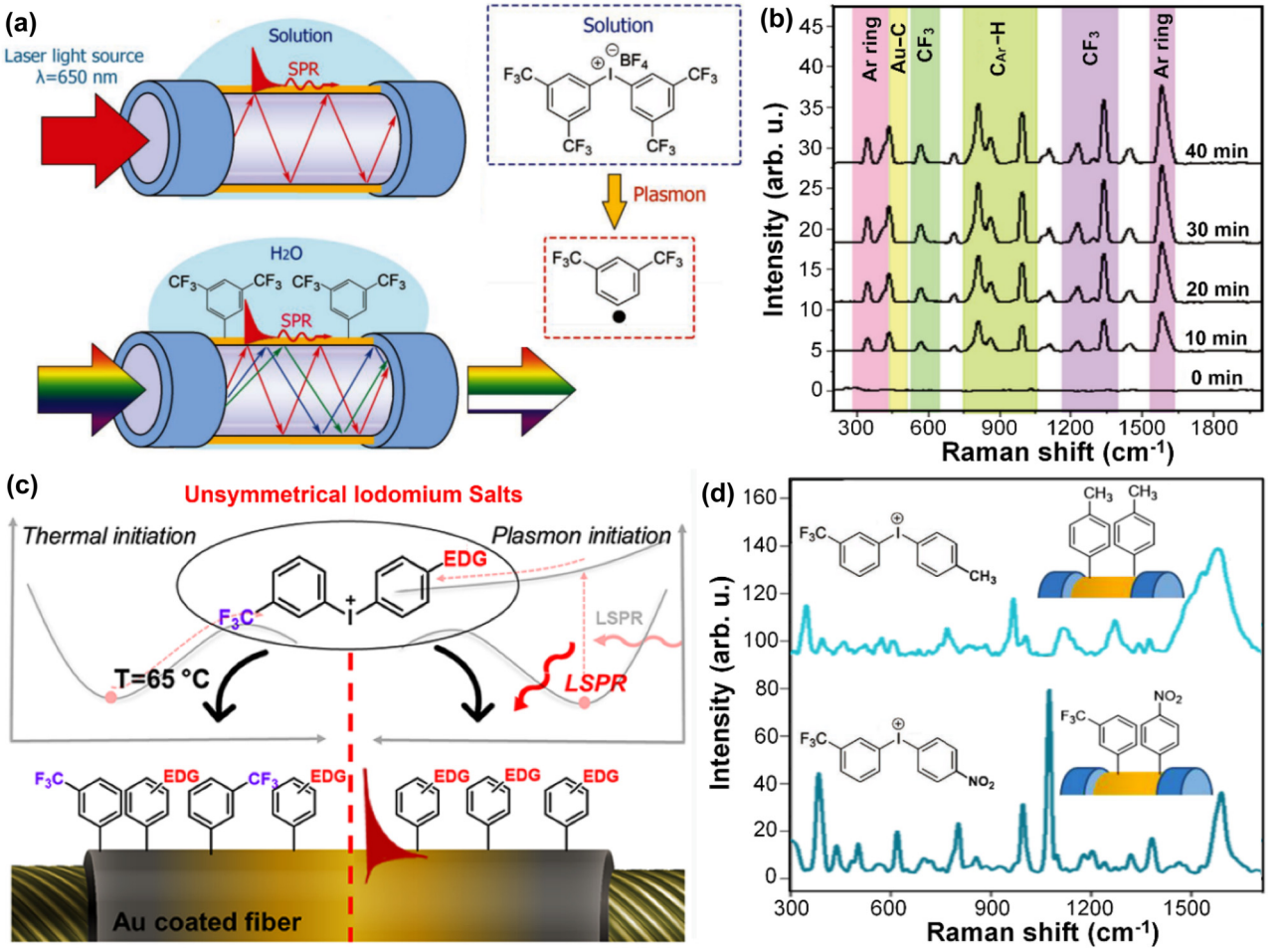

Figure 12: Plasmon-driven surface functionalization using iodonium salts as the precursors. (a) Schematic illustration of plasmon-driven surface functionalization of an Au-coated optical fiber using 3,5-*bis*(trifluoromethyl)phenyl iodonium tetrafluoroborate as the precursor. (b) SERS spectra measured on the pristine Au-coated fiber surface and after different reaction times during the plasmon-driven 3,5-*bis*(trifluoromethyl) phenyl grafting. (c) Schematic illustration of C–I bond cleavage and surface functionalization under thermal and plasmon-mediated reaction conditions when using unsymmetric iodonium salts as the precursors. (d) SERS spectra collected from Au-coated fiber after decomposition and grafting of (4-methylphenyl)[3-(trifluoromethyl)phenyl]iodonium (upper spectrum) and (4-nitrophenyl)(3-(trifluoromethyl)phenyl)iodonium (lower spectrum). Panels (a) and (b), adapted from ref. [184]. Copyright 2018 WILEY-VCH. Panels (c) and (d), adapted from ref. [185]. Copyright 2020 The American Chemistry Society.

Au could be optically excited by passing an excitation laser (650 nm) through the fiber. Exposure of an optically excited Au-coated optical fiber to an aqueous solution of di-[3,5-*bis*(trifluoromethyl)phenyl]iodonium tetrafluoroborate led to the cleavage of the C–I bonds and production of 3,5-*bis*(trifluoromethyl)phenyl radicals, which were spontaneously grafted to the Au surfaces upon formation of Au–C bonds. Coating the Au surfaces with a *bis*(trifluoromethyl)phenyl layer led to spectrally redshifted plasmon resonances and interesting antifouling properties. While the pristine Au surfaces appeared featureless in the SERS spectra, the plasmon-induced molecular grafting led to the emergence of strong SERS peaks signifying the formation of 3,5-*bis*(trifluoromethyl)phenyl moieties on Au surfaces (Figure 12b). By accommodating multiple plasmon-driven grafting steps, mixed-aryl coatings could be created on the metal surfaces. Under continuous laser excitation, exposure of an Au-coated optical fiber to di-[3,5-*bis*(trifluoromethyl)phenyl]iodonium and di(4-nitrophenyl)iodonium salts in a sequential manner could result in grafting of a mixed *bis*(trifluoromethyl)phenyl and 4-(nitrophenyl) layer on the Au surface.

Plasmon-driven C–I bond cleavage in unsymmetric iodonium salts was found to be more complicated than in symmetric iodonium salts because of the possibility to produce different types of aryl radicals exploitable for surface grafting. Therefore, the regioselectivity of plasmon-mediated homolytic decomposition became a critical issue

that must be taken into consideration [185]. Thermally driven dissociation of an unsymmetric iodonium salt at elevated reaction temperatures was typically featured by limited regioselectivity of C–I bond cleavage, leading to mixed-aryl coatings on Au surfaces. In striking contrast, with the aid of plasmons, the C–I bond cleavage occurred preferentially in electron-rich aryl substituents, resulting in the selective grafting of the more electron-rich aryl radical to the Au surface (Figure 12c). When choosing (4-methylphenyl)[3-(trifluoromethyl)phenyl]iodonium as the precursor, plasmon-driven C–I bond cleavage led to selective transfer of the 4-methylphenyl to the Au surface because the methyl group was an electron donating group (EDG). However, exposure of Au to (4-nitrophenyl)(3-(trifluoromethyl)phenyl)iodonium under laser illumination led to surface functionalization with mixed 4-nitrophenyl and 3-trifluoromethyl-phenyl moieties because both nitro and trifluoromethyl were electron-withdrawing groups.

The regioselectivity observed in plasmon-driven C–I bond cleavage in unsymmetric iodonium salts could be interpreted as the consequence of plasmon-enhanced intramolecular excitations [185]. The excitation of an electron from HOMO to LUMO of unsymmetric iodonium cation led to iodonium cations in their excited state with dissociative potential surfaces. It was theoretically predicted by TDDFT that the homolysis of the C–I bond located on the electron-rich aryl groups was kinetically favored, a general trend consistently observed in a series of unsymmetric iodonium salts bearing electron-donating aryl groups. For (4-nitrophenyl)(3-(trifluoromethyl)phenyl)iodonium, which represented an unsymmetric iodonium cation with electron-deficient aryl groups, both (3-(trifluoromethyl)phenyl and 4-nitrophenyl radicals were produced upon C–I bond cleavage induced by intramolecular electronic excitation. Dissociation of (4-nitrophenyl)(3-(trifluoromethyl)phenyl)iodonium *via* excitation by hot electrons, however, led to the formation of 3-(trifluoromethyl)phenyl radical with high regioselectivity, which disagreed with the experimental observations. The aforementioned experimental and theoretical results suggested that the regioselective cleavage of C–I bonds in unsymmetric iodonium salts was a consequence of plasmon-enhanced intramolecular excitations rather than hot electron injection or photothermal heating. Therefore, the plasmon-driven C–I bond cleavage in iodonium salts is mechanistically different from the hot electron-driven deiodination of 4-ITP chemisorbed to Au and Ag nanoparticle surfaces, which was discussed in detail in Section 4.4.

5.3 Plasmon-mediated synthesis of block copolymers

Free radicals produced through plasmon-driven bond-cleaving reactions can be utilized to induce molecular polymerization processes. Nitroxide-mediated polymerization [206]–[209] has been a living radical polymerization technique particularly useful for synthesizing polymer brushes on solid state materials surfaces. The nitroxide-mediated polymerization processes are initiated upon homolysis of the C–ON bond in an alkoxyamine initiator. With the aid of plasmon resonances, it has become possible to efficiently utilize visible and near-infrared light to chemoselectively activate the C–ON bond toward homolytic cleavage, followed by nitroxide-mediated polymerization on Au substrates under mild reaction conditions.

The feasibility of the plasmon-driven nitroxide-mediated polymerization was demonstrated by Tretyakov, Postnikov, and coworkers [210] using Au gratings as a plasmonic substate and a 785 nm CW laser or the sun light as the excitation light source, respectively. As illustrated in Figure 13a, diethyl (1-((1-(4-aminophenyl)ethoxy)(tert-butyl)amino)-2,2-dimethylpropyl) phosphonate was first subjected to diazotization to produce an arenediazonium tosylate, which was subsequently tethered to the surfaces of Au gratings *via* the diazonium chemistry. The surface-functionalized Au gratings were then immersed in a solution of N-isopropylacrylamide (NIPAM) under light illumination to induce the C–ON bond cleavage, which led to the formation of free radicals that initiated a polymerization process on Au surfaces. Through this plasmon-driven nitroxide-mediated polymerization process, block copolymers could be synthesized on the surface of Au gratings by further reacting with 4-vinylbenzeneboronic acid (VBA) monomers. The success in surface functionalization of Au gratings with poly(NIPAM)/poly (VBA) brushes was confirmed by atomic force microscopy, X-ray photoelectron spectroscopy, atomic force microscopy imaging, and SERS, while the plasmon-induced formation of free radicals was verified by electron spin resonance spectroscopy. Through plasmon-driven nitroxide-mediated polymerization, thermally promoted side reactions, such as the undesired formation of a cross linkage *via* boroxine formation, could be effectively suppressed, resulting in significantly enhanced chemoselectivity and precisely controlled block copolymer structures.

The Au gratings with covalently attached poly(NIPAM)/poly(VBA) block copolymers exhibited a unique combination of plasmonic and surface properties particularly useful

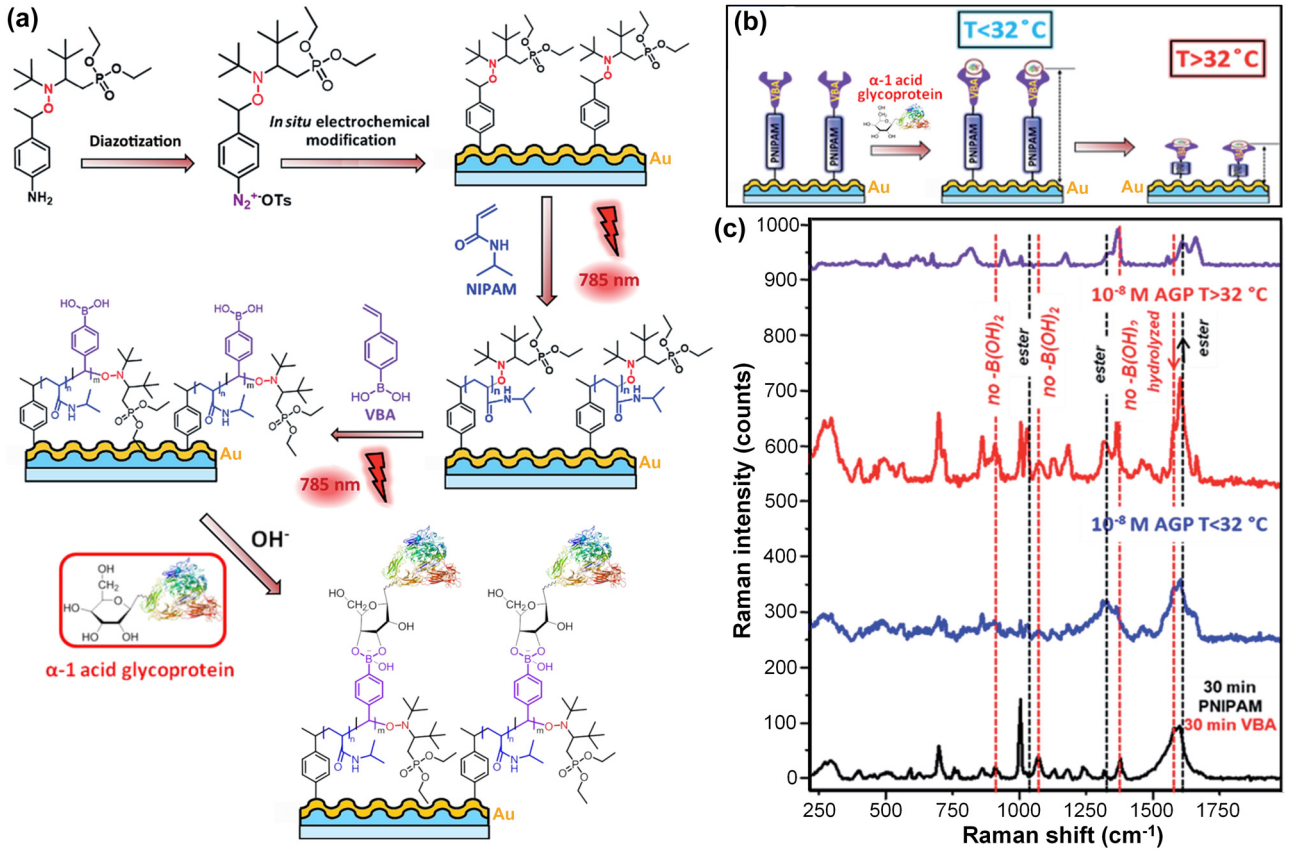

Figure 13: Plasmon-driven nitroxide-mediated polymerization. (a) Scheme illustrating plasmon-driven polymerization of poly(NIPAM)/poly(VBA) on Au gratings and entrapment of α–1 acid glycoprotein (AGP) by the polyVBA units. (b) The principle of α–1 glycoprotein detection at room and elevated temperatures. (c) SERS detection of AGP (10^{-8} M solution in phosphate buffer at pH 7.4). Adapted from ref. [210]. Copyright 2019 The Royal Society of Chemistry.

for biomolecular sensing applications. α–1 glycoprotein, a potentially useful circulating biomarkers for estimating the 5-year risk of all-cause mortality [211], was chosen as an analyte of interest to demonstrate the sensing capability of the block copolymer-functionalized Au gratings. The α–1 glycoprotein could be covalently entrapped by the polyVBA units through coupling reactions between the boronic acid and the carbohydrate moieties (Figure 13a). At a low temperature below 32 °C, the polyNIPAM units were in a swollen state and served as a flexible joint for the polyVBA units to enhance the effectiveness of capturing α–1 glycoprotein from solution. Increase of temperature led to the transition of the polyNIPAM units from the swollen state to the collapsed state, moving the entrapped α–1 glycoprotein closer to the plasmonic Au surface (Figure 13b). The reduced distance between Au surface and α–1 glycoprotein gave rise to significantly higher signal enhancements in the SERS spectra (Figure 13c), greatly improving the sensitivity for α–1 glycoprotein detection.

6 Concluding remarks

Plasmon-mediated photocatalysis provides a unique means of harnessing photon energy to induce the cleavage of specific chemical bonds in molecular adsorbates under mild reaction conditions. Chemoselective bond cleavage in molecular adsorbates can be triggered by plasmon resonances through multiple mechanisms involving plasmon-enhanced intramolecular excitations, transfer of hot carriers from metal to adsorbates following Landau damping, direct electronic excitations in strongly hybridized metal–adsorbate systems through CID, and photothermal activation of molecular vibrations. Even in some seemingly simple cases, such as homonuclear diatomic adsorbates, the detailed mechanisms involved in plasmon-driven bond cleavage can be highly complex and diverse, involving multiple reaction pathways. Some plasmon-driven molecule-scissoring reactions, such as N-demethylation of MB and decarboxylation of MBA, may even undergo pathway

switch upon variation of either the light illumination conditions or the local chemical environment at the metal–adsorbate interfaces. Over the past decade, tremendous research efforts have been devoted to mechanistic studies of plasmon-driven bond-cleaving processes. *In situ* spectroscopies and microscopies, such as STM imaging, ambient pressure XPS, SERS, TERS, EC-SERS, and EC-TERS, have become particularly useful tools for tracking detailed plasmon-driven molecule-transforming processes in real time under operando conditions. Computational tools, such as TDDFT, have been developed and widely utilized for calculating not only the optical responses of metallic nanostructures upon plasmonic excitations but also the dynamic transforming behaviors of molecular adsorbates stimulated by various plasmonic effects. Built upon the mechanistic insights gained from fundamental studies, plasmonic molecular scissors can be rationally designed to match the need for targeted applications, such as controlled release of molecular cargos, surface coating of solid-state materials, and selective bond activation for polymerization.

Through combined experimental and computational efforts, some unified mechanistic pictures have started to emerge over the past decade. The radiative and nonradiative decay of plasmon resonances creates several unique channels to deposit energy into molecular adsorbates, through which certain chemical bonds can be selectively activated for cleavage. In general, plasmon-induced bond activation involves the formation of either electronically or vibrationally excited intermediates triggered by enhanced local electric fields, energetic hot carriers, or photothermal heating. The nature of the frontier molecular orbitals involved in either electronic excitations or hot carrier transfer is a key factor determining the reaction pathway and chemoselectivity of a specific bond-cleaving reaction. On the other hand, the local chemical environment at the metal–adsorbate interfaces may play an equally important role in the selection of reaction pathways, as exemplified by the plasmon-driven N-demethylation of MB and decarboxylation of MBA discussed in this review article. Despite the remarkable progress made in the last decade, several critical aspects concerning detailed bond-cleaving mechanisms remain challenging to elucidate, well-worthy of further investigations.

The thermal and nonthermal contributions in plasmonic photocatalysis remain difficult to quantify [52], [87]–[92]. The key to solving this problem is to precisely the local temperature at the active sites on the photocatalyst surfaces through nanothermometric measurements. Considering the exponential relationship between reaction rate and temperature, even a slight uncertainty in thermometric measurements can lead to significant under- or overestimate of the relatively contributions of the nonthermal and thermal plasmonic effects. In addition, the local temperatures at the photocatalytically active sites may differ significantly from the apparent temperatures in the photocatalyst bed measured at the ensemble level. With recent advancements in plasmonic nanothermometry, it has become possible to precisely measure the local temperatures in a single plasmonic hot spot [212] and even at the single molecule level [213], which will eventually enable us to clarify some widely debated issues regarding the nonthermal and thermal effects.

Both indirect transfer of hot electrons following Landau damping and direct electronic excitation through CID lead to the transient anionic intermediates, lowering the activation energy for bond cleavage [147], [148]. Landau damping and CID may give rise to different quantum efficiencies, reaction selectivity, and kinetic features in plasmon-mediated photocatalysis. However, distinguishing these two mechanisms can be extremely challenging, especially for those mechanistically complicated reactions involving multiple reaction pathways. In numerous cases, identification of the metal and adsorbate states involved in the electronic transitions for a CID-induced reaction is not an easy task due to the complexity of the metal–adsorbate interactions. Experimental approaches capable of unambiguously distinguishing these two mechanisms have so far not been fully established yet.

Plasmon-driven bond cleavage in molecular adsorbates may lead to the formation of intermediates that further evolve into the final products. Identification of important intermediates represents a crucial step toward thorough mechanistic understanding of multistep molecule-transforming processes. Plasmon-enhanced spectroscopies, such as SERS and TERS, can be used as unique *in situ* molecular fingerprinting tools to identify the intermediate species and track their production and consumption during plasmon-driven reactions [43]–[47]. Deliberately designed steady-state and pump/probe-based time-resolved SERS/TERS measurements can provide detailed information about plasmon-induced molecule-transforming events over a broad distribution of timescales ranging from picoseconds to minutes [43]–[47]. Ultrafast SERS/TERS approaches capable of probing even faster molecular events occurring at the early stages of plasmon decay over femtosecond–picosecond timescales still need to be developed. In addition, transient intermediates exhibiting short lifetimes, small Raman cross sections, and spectroscopic features overlapping with those of the reactants and products remain difficult to resolve in SERS/TERS measurements.

Therefore, SERS/TERS needs to be further combined with other time-resolved spectroscopic tools to fully characterize plasmon–adsorbate interactions over the entire range of timescales relevant to plasmonic photocatalysis.

TDDFT has become a particularly useful computational tool for studying the effects of hot carriers and local fields on the dynamic transforming behaviors of molecular adsorbate on metal surfaces. However, the clusters of metal atoms employed in the computational work are too small to support any localized plasmon resonances [100], [111], [127], [128], [214]. Therefore, the TDDFT results do not fully describe the photoexcitation, transfer, and relaxation of hot carriers in experimentally utilized plasmonic photocatalysts. New computational approaches capable of modeling molecular adsorbates on much larger metal nanoparticles in the experimentally relevant size regime need to be developed.

When constructing plasmonic molecular scissors, nanoparticles of noble metals, most commonly Au and Ag, are typically used as plasmonic photocatalysts. Unfortunately, the high cost and scarcity of the noble metal elements limit the large-scale applications of these plasmonic molecular scissors. There has been a tremendous interest in searching for alternative plasmonic materials made of cheaper and more earth-abundant elements, which can potentially replace the noble metals for various applications [215]–[217]. It has been demonstrated that plasmonic nanoparticles made of non-noble metal elements and doped semiconductors, such as Al [101], Mg [218], copper selenides [219], and oxygen vacancy-rich MoO_{3-x} [220], can also be employed as plasmonic photocatalysts to drive molecular transformations. Detailed mechanisms of photocatalytic bond cleavage in molecular adsorbates on these alternative plasmonic materials remain largely unexplored, representing a fundamentally intriguing and potentially transformative research area.

As the discoveries of new materials and reactions continue, we expect to witness ever-increasing mechanistic diversity and complexity of plasmon-driven photocatalytic reactions. When utilizing plasmonic photocatalysis for practical applications, a series of critical issues concerning materials cost, quantum efficiencies, photocatalyst durability, reaction scalability, and reactor design, should all be taken into careful consideration. Thorough understanding of detailed bond-cleaving mechanisms will enable us to build a solid knowledge platform, based upon which both the light–matter and plasmon–adsorbate interactions can be rationally fine-tuned to achieve optimized light-harvesting efficiencies, precisely controlled kinetic features, and targeted reaction outcomes through plasmonic photocatalysis.

Acknowledgment: The publication of this article was funded by the University of South Carolina Libraries Open Access Fund.

Research funding: This work was supported by the Macromolecular, Supramolecular, and Nanochemistry Program in the Division of Chemistry of the National Science Foundation (NSF) of the United States of America under Grant CHE-2202928. The content is solely the responsibility of the author and does not necessarily represent the official views of the NSF.

Author contribution: Single author contribution.

Conflict of interest: The author declares no conflicts of interest regarding this article.

Ethical approval: The conducted research is not related to either human or animals use.

Data availability: Data sharing does not apply to this article as no datasets were generated or analyzed during the current study.

References

[1] A. Gellé, T. Jin, L. de la Garza, G. D. Price, L. V. Besteiro, and A. Moores, “Applications of plasmon-enhanced nanocatalysis to organic transformations,” *Chem. Rev.*, vol. 120, no. 2, pp. 986–1041, 2020.

[2] S. Linic, U. Aslam, C. Boerigter, and M. Morabito, “Photochemical transformations on plasmonic metal nanoparticles,” *Nat. Mater.*, vol. 14, no. 6, pp. 567–576, 2015.

[3] S. Linic, P. Christopher, and D. B. Ingram, “Plasmonic-metal nanostructures for efficient conversion of solar to chemical energy,” *Nat. Mater.*, vol. 10, no. 12, pp. 911–921, 2011.

[4] Y. C. Zhang, *et al*., “Surface-plasmon-driven hot electron photochemistry,” *Chem. Rev.*, vol. 118, no. 6, pp. 2927–2954, 2018.

[5] I. Kherbouche, Y. Luo, N. Félidj, and C. Mangeney, “Plasmon-mediated surface functionalization: new horizons for the control of surface chemistry on the nanoscale,” *Chem. Mater.*, vol. 32, no. 13, pp. 5442–5454, 2020.

[6] M. J. Kale, T. Avanesian, and P. Christopher, “Direct photocatalysis by plasmonic nanostructures,” *ACS Catal.*, vol. 4, no. 1, pp. 116–128, 2014.

[7] N. J. Halas, S. Lal, W. S. Chang, S. Link, and P. Nordlander, “Plasmons in strongly coupled metallic nanostructures,” *Chem. Rev.*, vol. 111, no. 6, pp. 3913–3961, 2011.

[8] P. K. Jain, X. H. Huang, I. H. El-Sayed, and M. A. El-Sayed, “Noble metals on the nanoscale: optical and photothermal properties and some applications in imaging, sensing, biology, and medicine,” *Acc. Chem. Res.*, vol. 41, no. 12, pp. 1578–1586, 2008.

[9] L. Novotny and N. van Hulst, “Antennas for light,” *Nat. Photonics*, vol. 5, no. 2, pp. 83–90, 2011.

[10] J. A. Schuller, E. S. Barnard, W. S. Cai, Y. C. Jun, J. S. White, and M. L. Brongersma, “Plasmonics for extreme light concentration and manipulation,” *Nat. Mater.*, vol. 9, no. 3, pp. 193–204, 2010.

[11] M. L. Brongersma, N. J. Halas, and P. Nordlander, “Plasmon-induced hot carrier science and technology,” *Nat. Nanotechnol.*, vol. 10, no. 1, pp. 25–34, 2015.

[12] K. Kneipp, H. Kneipp, I. Itzkan, R. R. Dasari, and M. S. Feld, "Ultrasensitive chemical analysis by Raman spectroscopy," *Chem. Rev.*, vol. 99, no. 10, pp. 2957–2976, 1999.
[13] J. Langer, *et al*., "Present and future of surface-enhanced Raman scattering," *ACS Nano*, vol. 14, no. 1, pp. 28–117, 2020.
[14] B. Sharma, R. R. Frontiera, A. I. Henry, E. Ringe, and R. P. Van Duyne, "SERS: materials, applications, and the future," *Mater. Today*, vol. 15, nos. 1–2, pp. 16–25, 2012.
[15] C. Zong, *et al*., "Surface-enhanced Raman spectroscopy for bioanalysis: reliability and challenges," *Chem. Rev.*, vol. 118, no. 10, pp. 4946–4980, 2018.
[16] K. Aslan, I. Gryczynski, J. Malicka, E. Matveeva, J. R. Lakowicz, and C. D. Geddes, "Metal-enhanced fluorescence: an emerging tool in biotechnology," *Curr. Opin. Biotechnol.*, vol. 16, no. 1, pp. 55–62, 2005.
[17] E. Fort and S. Grésillon, "Surface enhanced fluorescence," *J. Phys. D-Appl. Phys.*, vol. 41, no. 1, 2008, Art. no. 013001.
[18] J. F. Li, C. Y. Li, and R. F. Aroca, "Plasmon-enhanced fluorescence spectroscopy," *Chem. Soc. Rev.*, vol. 46, no. 13, pp. 3962–3979, 2017.
[19] S. Kühn, U. Håkanson, L. Rogobete, and V. Sandoghdar, "Enhancement of single-molecule fluorescence using a gold nanoparticle as an optical nanoantenna," *Phys. Rev. Lett.*, vol. 97, no. 1, 2006, Art. no. 017402.
[20] S. K. Ghosh and T. Pal, "Interparticle coupling effect on the surface plasmon resonance of gold nanoparticles: from theory to applications," *Chem. Rev.*, vol. 107, no. 11, pp. 4797–4862, 2007.
[21] L. Brus, "Noble metal nanocrystals: plasmon electron transfer photochemistry and single-molecule Raman spectroscopy," *Acc. Chem. Res.*, vol. 41, no. 12, pp. 1742–1749, 2008.
[22] K. Kneipp, H. Kneipp, and J. Kneipp, "Surface-enhanced Raman scattering in local optical fields of silver and gold nanoaggregatess – from single-molecule Raman spectroscopy to ultrasensitive probing in live cells," *Acc. Chem. Res.*, vol. 39, no. 7, pp. 443–450, 2006.
[23] E. C. Le Ru and P. G. Etchegoin, "Single-molecule surface-enhanced Raman spectroscopy," *Ann. Rev. Phys. Chem.*, vol. 63, pp. 65–87, 2012.
[24] A. B. Zrimsek, *et al*., "Single-molecule chemistry with surface- and tip-enhanced Raman spectroscopy," *Chem. Rev.*, vol. 117, no. 11, pp. 7583–7613, 2017.
[25] A. O. Govorov, H. Zhang, H. V. Demir, and Y. K. Gun'ko, "Photogeneration of hot plasmonic electrons with metal nanocrystals: quantum description and potential applications," *Nano Today*, vol. 9, no. 1, pp. 85–101, 2014.
[26] J. Zhao, *et al*., "A comparison of photocatalytic activities of gold nanoparticles following plasmonic and interband excitation and a strategy for harnessing interband hot carriers for solution phase photocatalysis," *ACS Cent. Sci.*, vol. 3, no. 5, pp. 482–488, 2017.
[27] P. Lyu, R. Espinoza, and S. C. Nguyen, "Photocatalysis of metallic nanoparticles: interband vs. intraband induced mechanisms," *J. Phys. Chem. C*, vol. 127, no. 32, pp. 15685–15698, 2023.
[28] V. Jain, R. K. Kashyap, and P. P. Pillai, "Plasmonic photocatalysis: activating chemical bonds through light and plasmon," *Adv. Opt. Mater.*, vol. 10, no. 15, 2022, Art. no. 2200463.
[29] E. Cortés, "Efficiency and bond selectivity in plasmon-induced photochemistry," *Adv. Opt. Mater.*, vol. 5, no. 15, 2017, Art. no. 1700191.
[30] P. Christopher, H. L. Xin, A. Marimuthu, and S. Linic, "Singular characteristics and unique chemical bond activation mechanisms of photocatalytic reactions on plasmonic nanostructures," *Nat. Mater.*, vol. 11, no. 12, pp. 1044–1050, 2012.
[31] M. Fang, X. L. Tan, Z. X. Liu, B. W. Hu, and X. K. Wang, "Recent progress on metal-enhanced photocatalysis: a review on the mechanism," *Research*, vol. 2021, 2021, Art. no. 9794329.
[32] R. Long, Y. Li, L. Song, and Y. J. Xiong, "Coupling solar energy into reactions: materials design for surface plasmon-mediated catalysis," *Small*, vol. 11, no. 32, pp. 3873–3889, 2015.
[33] X. Zhang, *et al*., "Product selectivity in plasmonic photocatalysis for carbon dioxide hydrogenation," *Nat. Commun.*, vol. 8, no. 1, 2017, Art. no. 14542.
[34] Z. Li, *et al*., "Plasmon-determined selectivity in photocatalytic transformations on gold and gold–palladium nanostructures," *ACS Photonics*, vol. 10, no. 9, pp. 3390–3400, 2023.
[35] Y. Dong, C. Hu, H. Xiong, R. Long, and Y. Xiong, "Plasmonic catalysis: new opportunity for selective chemical bond evolution," *ACS Catal.*, vol. 13, no. 10, pp. 6730–6743, 2023.
[36] X.-Q. Liu, *et al*., "Enhancing catalytic activity and selectivity by plasmon-induced hot carriers," *iScience*, vol. 23, no. 5, 2020, Art. no. 101107.
[37] L. V. Besteiro, *et al*., "The fast and the furious: ultrafast hot electrons in plasmonic metastructures. Size and structure matter," *Nano Today*, vol. 27, pp. 120–145, 2019.
[38] P. Christopher and M. Moskovits, "Hot charge carrier transmission from plasmonic nanostructures," *Ann. Rev. Phys. Chem.*, vol. 68, pp. 379–398, 2017.
[39] K. Sytwu, M. Vadai, and J. A. Dionne, "Bimetallic nanostructures: combining plasmonic and catalytic metals for photocatalysis," *Adv. Phys. X*, vol. 4, no. 1, 2019, Art. no. 1619480.
[40] W. Jiang, *et al*., "Active site engineering on plasmonic nanostructures for efficient photocatalysis," *ACS Nano*, vol. 17, no. 5, pp. 4193–4229, 2023.
[41] C. C. Carlin, *et al*., "Nanoscale and ultrafast in situ techniques to probe plasmon photocatalysis," *Chem. Phys. Rev.*, vol. 4, no. 4, 2023, Art. no. 041309.
[42] E. Cortés, R. Grzeschik, S. A. Maier, and S. Schlücker, "Experimental characterization techniques for plasmon-assisted chemistry," *Nat. Rev. Chem*, vol. 6, no. 4, pp. 259–274, 2022.
[43] C. L. Warkentin, Z. W. Yu, A. Sarkar, and R. R. Frontiera, "Decoding chemical and physical processes driving plasmonic photocatalysis using surface-enhanced Raman spectroscopies," *Acc. Chem. Res.*, vol. 54, no. 10, pp. 2457–2466, 2021.
[44] K. X. Chen and H. Wang, "Plasmon-driven photocatalytic molecular transformations on metallic nanostructure surfaces: mechanistic insights gained from plasmon-enhanced Raman spectroscopy," *Mol. Syst. Des. Eng.*, vol. 6, no. 4, pp. 250–280, 2021.
[45] Z. D. Li and D. Kurouski, "Plasmon-driven chemistry on mono- and bimetallic nanostructures," *Acc. Chem. Res.*, vol. 54, no. 10, pp. 2477–2487, 2021.
[46] C. Zhan, X. J. Chen, Y. F. Huang, D. Y. Wu, and Z. Q. Tian, "Plasmon-mediated chemical reactions on nanostructures unveiled by surface-enhanced Raman spectroscopy," *Acc. Chem. Res.*, vol. 52, no. 10, pp. 2784–2792, 2019.
[47] H. Wang, "Deciphering plasmonic photocatalysis using plasmon-enhanced Raman spectroscopy," *Trends Chem.*, vol. 6, no. 9, pp. 510–524, 2024.

[48] Z. Fusco and F. J. Beck, "Advances in fundamentals and application of plasmon-assisted CO_2 photoreduction," *Nanophotonics*, vol. 13, no. 4, pp. 387–417, 2024.
[49] L. Yuan, B. B. Bourgeois, C. C. Carlin, F. H. da Jornada, and J. A. Dionne, "Sustainable chemistry with plasmonic photocatalysts," *Nanophotonics*, vol. 12, no. 14, pp. 2745–2762, 2023.
[50] J. H. Yang, Y. Z. Guo, W. Z. Lu, R. B. Jiang, and J. F. Wang, "Emerging applications of plasmons in driving CO_2 reduction and N_2 fixation," *Adv. Mater.*, vol. 30, no. 48, 2018, Art. no. 1802227.
[51] A. Choudhary, A. Halder, P. Aggarwal, and V. G. Rao, "Plasmonic chemistry for sustainable ammonia production," *Commun. Mater.*, vol. 5, no. 1, 2024, Art. no. 69.
[52] E. Cortés, *et al*., "Challenges in plasmonic catalysis," *ACS Nano*, vol. 14, no. 12, pp. 16202–16219, 2020.
[53] C. Zhan, M. Moskovits, and Z. Q. Tian, "Recent progress and prospects in plasmon-mediated chemical reaction," *Matter*, vol. 3, no. 1, pp. 42–56, 2020.
[54] E. Kazuma, "Key factors for controlling plasmon-induced chemical reactions on metal surfaces," *J. Phys. Chem. Lett.*, vol. 15, no. 1, pp. 59–67, 2024.
[55] L. Mascaretti, *et al*., "Challenges and prospects of plasmonic metasurfaces for photothermal catalysis," *Nanophotonics*, vol. 11, no. 13, pp. 3035–3056, 2022.
[56] W. H. Ou, B. B. Zhou, J. D. Shen, C. H. Zhao, Y. Y. Li, and J. Lu, "Plasmonic metal nanostructures: concepts, challenges and opportunities in photo-mediated chemical transformations," *iScience*, vol. 24, no. 2, 2021, Art. no. 101982.
[57] J. I. Gersten and A. Nitzan, "Photophysics and photochemistry near surfaces and small particles," *Surf. Sci.*, vol. 158, no. 1, pp. 165–189, 1985.
[58] B. N. J. Persson and N. D. Lang, "Electron-hole-pair quenching of excited states near a metal," *Phys. Rev. B*, vol. 26, no. 10, pp. 5409–5415, 1982.
[59] T. L. Jennings, M. P. Singh, and G. F. Strouse, "Fluorescent lifetime quenching near d = 1.5 nm gold nanoparticles: probing NSET validity," *J. Am. Chem. Soc.*, vol. 128, no. 16, pp. 5462–5467, 2006.
[60] M. P. Singh and G. F. Strouse, "Involvement of the LSPR spectral overlap for energy transfer between a dye and Au nanoparticle," *J. Am. Chem. Soc.*, vol. 132, no. 27, pp. 9383–9391, 2010.
[61] C. Chen and N. Hildebrandt, "Resonance energy transfer to gold nanoparticles: NSET defeats FRET," *TrAC Trends Anal. Chem.*, vol. 123, p. 115748, 2020.
[62] J. T. Li, *et al*., "Ag@Cu_2O core-shell nanoparticles as visible-light plasmonic photocatalysts," *ACS Catal.*, vol. 3, no. 1, pp. 47–51, 2013.
[63] J. T. Li, S. K. Cushing, F. K. Meng, T. R. Senty, A. D. Bristow, and N. Q. Wu, "Plasmon-induced resonance energy transfer for solar energy conversion," *Nat. Photonics*, vol. 9, no. 9, pp. 601–607, 2015.
[64] S. K. Cushing, *et al*., "Photocatalytic activity enhanced by plasmonic resonant energy transfer from metal to semiconductor," *J. Am. Chem. Soc.*, vol. 134, no. 36, pp. 15033–15041, 2012.
[65] E. Kazuma and Y. Kim, "Mechanistic studies of plasmon chemistry on metal catalysts," *Angew. Chem. Int. Ed.*, vol. 58, no. 15, pp. 4800–4808, 2019.
[66] A. J. Haes, S. L. Zou, G. C. Schatz, and R. P. Van Duyne, "Nanoscale optical biosensor: short range distance dependence of the localized surface plasmon resonance of noble metal nanoparticles," *J. Phys. Chem. B*, vol. 108, no. 22, pp. 6961–6968, 2004.
[67] J. F. Li, *et al*., "Shell-isolated nanoparticle-enhanced Raman spectroscopy," *Nature*, vol. 464, no. 7287, pp. 392–395, 2010.
[68] A. M. Brown, R. Sundararaman, P. Narang, W. A. Goddard, and H. A. Atwater, "Nonradiative plasmon decay and hot carrier dynamics: effects of phonons, surfaces, and geometry," *ACS Nano*, vol. 10, no. 1, pp. 957–966, 2016.
[69] J. B. Khurgin, "Fundamental limits of hot carrier injection from metal in nanoplasmonics," *Nanophotonics*, vol. 9, no. 2, pp. 453–471, 2020.
[70] H. H. Shin, *et al*., "Vibrationally hot reactants in a plasmon-assisted chemical reaction," *J. Am. Chem. Soc.*, vol. 145, no. 22, pp. 12264–12274, 2023.
[71] S. R. Hatch, X. Y. Zhu, J. M. White, and A. Campion, "Photoinduced pathways to dissociation and desorption of dioxygen on Ag(110) and Pt(111)," *J. Phys. Chem.*, vol. 95, no. 4, pp. 1759–1768, 1991.
[72] S. K. So, R. Franchy, and W. Ho, "Photodesorption of NO from Ag(111) and Cu(111)," *J. Chem. Phys.*, vol. 95, no. 2, pp. 1385–1399, 1991.
[73] J. W. Gadzuk, "Hot-electron femtochemistry at surfaces: on the role of multiple electron processes in desorption," *Chem. Phys.*, vol. 251, nos. 1–3, pp. 87–97, 2000.
[74] M. Bonn, *et al*., "Phonon- versus electron-mediated desorption and oxidation of CO on Ru(0001)," *Science*, vol. 285, no. 5430, pp. 1042–1045, 1999.
[75] S. A. Buntin, L. J. Richter, R. R. Cavanagh, and D. S. King, "Optically driven surface-reactions — evidence for the role of hot-electrons," *Phys. Rev. Lett.*, vol. 61, no. 11, pp. 1321–1324, 1988.
[76] F. J. Kao, D. G. Busch, D. G. Dacosta, and W. Ho, "Femtosecond versus nanosecond surface photochemistry — $O_2 + CO$ on Pt(111) at 80 K," *Phys. Rev. Lett.*, vol. 70, no. 26, pp. 4098–4101, 1993.
[77] P. Avouris and R. E. Walkup, "Fundamental mechanisms of desorption and fragmentation induced by electronic-transitions at surfaces," *Annu. Rev. Phys. Chem.*, vol. 40, pp. 173–206, 1989.
[78] J. A. Misewich, T. F. Heinz, and D. M. Newns, "Desorption induced by multiple electronic-transitions," *Phys. Rev. Lett.*, vol. 68, no. 25, pp. 3737–3740, 1992.
[79] S. A. Lee and S. Link, "Chemical interface damping of surface plasmon resonances," *Acc. Chem. Res.*, vol. 54, no. 8, pp. 1950–1960, 2021.
[80] A. J. Therrien, M. J. Kale, L. Yuan, C. Zhang, N. J. Halas, and P. Christopher, "Impact of chemical interface damping on surface plasmon dephasing," *Faraday Discuss.*, vol. 214, pp. 59–72, 2019.
[81] K. Wu, J. Chen, J. R. McBride, and T. Lian, "Efficient hot-electron transfer by a plasmon-induced interfacial charge-transfer transition," *Science*, vol. 349, no. 6248, pp. 632–635, 2015.
[82] R. Ogata, H. Nishi, T. Ishida, and T. Tatsuma, "Visualization of nano-localized and delocalized oxidation sites for plasmon-induced charge separation," *Nanoscale*, vol. 13, no. 2, pp. 681–684, 2021.
[83] R. Kamarudheen, G. J. W. Aalbers, R. F. Hamans, L. P. J. Kamp, and A. Baldi, "Distinguishing among all possible activation mechanisms of a plasmon-driven chemical reaction," *ACS Energy Lett.*, vol. 5, no. 8, pp. 2605–2613, 2020.
[84] J. R. Adleman, D. A. Boyd, D. G. Goodwin, and D. Psaltis, "Heterogenous catalysis mediated by plasmon heating," *Nano Lett.*, vol. 9, no. 12, pp. 4417–4423, 2009.

[85] T. Bora, D. Zoepfl, and J. Dutta, "Importance of plasmonic heating on visible light driven photocatalysis of gold nanoparticle decorated zinc oxide nanorods," *Sci. Rep.*, vol. 6, no. 1, 2016, Art. no. 26913.
[86] C. Fasciani, C. J. B. Alejo, M. Grenier, J. C. Netto-Ferreira, and J. C. Scaiano, "High-temperature organic reactions at room temperature using plasmon excitation: decomposition of dicumyl peroxide," *Org. Lett.*, vol. 13, no. 2, pp. 204–207, 2011.
[87] X. Zhang, *et al*., "Plasmon-enhanced catalysis: distinguishing thermal and nonthermal effects," *Nano Lett.*, vol. 18, no. 3, pp. 1714–1723, 2018.
[88] L. A. Zhou, *et al*., "Quantifying hot carrier and thermal contributions in plasmonic photocatalysis," *Science*, vol. 362, no. 6410, pp. 69–72, 2018.
[89] R. Kamarudheen, G. W. Castellanos, L. P. J. Kamp, H. J. H. Clercx, and A. Baldi, "Quantifying photothermal and hot charge carrier effects in plasmon-driven nanoparticle syntheses," *ACS Nano*, vol. 12, no. 8, pp. 8447–8455, 2018.
[90] X. Li, X. Zhang, H. O. Everitt, and J. Liu, "Light-induced thermal gradients in ruthenium catalysts significantly enhance ammonia production," *Nano Lett.*, vol. 19, no. 3, pp. 1706–1711, 2019.
[91] Y. Negrín-Montecelo, *et al*., "Plasmonic photocatalysis in aqueous solution: assessing the contribution of thermal effects and evaluating the role of photogenerated ROS," *Nanoscale*, vol. 14, no. 32, pp. 11612–11618, 2022.
[92] Z. Geng, Y. Yu, A. J. Offen, and J. Liu, "Achieving maximum overall light enhancement in plasmonic catalysis by combining thermal and non-thermal effects," *Nat. Catal.*, vol. 6, no. 12, pp. 1241–1247, 2023.
[93] S. Mukherjee, *et al*., "Hot electrons do the impossible: plasmon-induced dissociation of H_2 on Au," *Nano Lett.*, vol. 13, no. 1, pp. 240–247, 2013.
[94] S. Mukherjee, *et al*., "Hot-electron-induced dissociation of H_2 on gold nanoparticles supported on SiO_2," *J. Am. Chem. Soc.*, vol. 136, no. 1, pp. 64–67, 2014.
[95] G. Baffou, I. Bordacchini, A. Baldi, and R. Quidant, "Simple experimental procedures to distinguish photothermal from hot-carrier processes in plasmonics," *Light Sci. Appl.*, vol. 9, no. 1, 2020, Art. no. 108.
[96] Y. Sivan, J. H. Baraban, and Y. Dubi, "Experimental practices required to isolate thermal effects in plasmonic photo-catalysis: lessons from recent experiments," *OSA Contin.*, vol. 3, no. 3, pp. 483–497, 2020.
[97] C. Deeb, C. Ecoffet, R. Bachelot, J. Plain, A. Bouhelier, and O. Soppera, "Plasmon-based free-radical photopolymerization: effect of diffusion on nanolithography processes," *J. Am. Chem. Soc.*, vol. 133, no. 27, pp. 10535–10542, 2011.
[98] K. Ueno, *et al*., "Nanoparticle plasmon-assisted two-photon polymerization induced by incoherent excitation source," *J. Am. Chem. Soc.*, vol. 130, no. 22, pp. 6928–6929, 2008.
[99] Y. Zhang, T. Nelson, S. Tretiak, H. Guo, and G. C. Schatz, "Plasmonic hot-carrier-mediated tunable photochemical reactions," *ACS Nano*, vol. 12, no. 8, pp. 8415–8422, 2018.
[100] Q. S. Wu, L. S. Zhou, G. C. Schatz, Y. Zhang, and H. Guo, "Mechanistic insights into photocatalyzed H_2 dissociation on Au clusters," *J. Am. Chem. Soc.*, vol. 142, no. 30, pp. 13090–13101, 2020.
[101] L. Zhou, *et al*., "Aluminum nanocrystals as a plasmonic photocatalyst for hydrogen dissociation," *Nano Lett.*, vol. 16, no. 2, pp. 1478–1484, 2016.
[102] S. K. Giri and G. C. Schatz, "Photodissociation of H_2 on Ag and Au nanoparticles: effect of size and plasmon versus interband transitions on threshold intensities for dissociation," *J. Phys. Chem. C*, vol. 127, no. 8, pp. 4115–4123, 2023.
[103] M. G. Blaber, M. D. Arnold, and M. J. Ford, "A review of the optical properties of alloys and intermetallics for plasmonics," *J. Phys.-Condens. Matter*, vol. 22, no. 14, 2010, Art. no. 143201.
[104] H. Wang, F. Tam, N. K. Grady, and N. J. Halas, "Cu nanoshells: effects of interband transitions on the nanoparticle plasmon resonance," *J. Phys. Chem. B*, vol. 109, no. 39, pp. 18218–18222, 2005.
[105] G. H. Chan, J. Zhao, E. M. Hicks, G. C. Schatz, and R. P. Van Duyne, "Plasmonic properties of copper nanoparticles fabricated by nanosphere lithography," *Nano Lett.*, vol. 7, no. 7, pp. 1947–1952, 2007.
[106] M. Valenti, *et al*., "Hot carrier generation and extraction of plasmonic alloy nanoparticles," *ACS Photonics*, vol. 4, no. 5, pp. 1146–1152, 2017.
[107] S. K. F. Stofela, *et al*., "A noble-transition alloy excels at hot-carrier generation in the near infrared," *Adv. Mater.*, vol. 32, no. 23, 2020, Art. no. 1906478.
[108] M. Q. Sun, A. K. Wang, M. Zhang, S. L. Zou, and H. Wang, "Interband and intraband hot carrier-driven photocatalysis on plasmonic bimetallic nanoparticles: a case study of Au-Cu alloy nanoparticles," *ACS Nanosci. Au*, vol. 4, no. 5, pp. 360–373, 2024.
[109] P. Christopher, H. L. Xin, and S. Linic, "Visible-light-enhanced catalytic oxidation reactions on plasmonic silver nanostructures," *Nat. Chem.*, vol. 3, no. 6, pp. 467–472, 2011.
[110] B. Seemala, *et al*., "Plasmon-mediated catalytic O_2 dissociation on Ag nanostructures: hot electrons or near fields?" *ACS Energy Lett.*, vol. 4, no. 8, pp. 1803–1809, 2019.
[111] C. J. Herring and M. M. Montemore, "Mechanistic insights into plasmonic catalysis by dynamic calculations: O_2 and N_2 on Au and Ag nanoparticles," *Chem. Mater.*, vol. 35, no. 4, pp. 1586–1593, 2023.
[112] M. J. Chalkley, M. W. Drover, and J. C. Peters, "Catalytic N_2-to-NH_3 (or -N_2H_4) conversion by well-defined molecular coordination complexes," *Chem. Rev.*, vol. 120, no. 12, pp. 5582–5636, 2020.
[113] S. L. Foster, *et al*., "Catalysts for nitrogen reduction to ammonia," *Nat. Catal.*, vol. 1, no. 7, pp. 490–500, 2018.
[114] L. Shi, Y. Yin, S. B. Wang, and H. Q. Sun, "Rational catalyst design for N_2 reduction under ambient conditions: strategies toward enhanced conversion efficiency," *ACS Catal.*, vol. 10, no. 12, pp. 6870–6899, 2020.
[115] S. Y. Wang, F. Ichihara, H. Pang, H. Chen, and J. H. Ye, "Nitrogen fixation reaction derived from nanostructured catalytic materials," *Adv. Funct. Mater.*, vol. 28, no. 50, 2018, Art. no. 1803309.
[116] H. Bothe, O. Schmitz, M. G. Yates, and W. E. Newton, "Nitrogen fixation and hydrogen metabolism in cyanobacteria," *Microbiol. Mol. Biol. Rev.*, vol. 74, no. 4, pp. 529–551, 2010.
[117] Q. Cheng, "Perspectives in biological nitrogen fixation research," *J. Integr. Plant Biol.*, vol. 50, no. 7, pp. 786–798, 2008.
[118] L. C. Seefeldt, *et al*., "Reduction of substrates by nitrogenases," *Chem. Rev.*, vol. 120, no. 12, pp. 5082–5106, 2020.

[119] A. J. Martín, T. Shinagawa, and J. Pérez-Ramírez, "Electrocatalytic reduction of nitrogen: from Haber-Bosch to ammonia artificial leaf," *Chem*, vol. 5, no. 2, pp. 263–283, 2019.
[120] G. Qing, *et al*., "Recent advances and challenges of electrocatalytic N_2 reduction to ammonia," *Chem. Rev.*, vol. 120, no. 12, pp. 5437–5516, 2020.
[121] C. Tang and S. Z. Qiao, "How to explore ambient electrocatalytic nitrogen reduction reliably and insightfully," *Chem. Soc. Rev.*, vol. 48, no. 12, pp. 3166–3180, 2019.
[122] X. Z. Chen, N. Li, Z. Z. Kong, W. J. Ong, and X. J. Zhao, "Photocatalytic fixation of nitrogen to ammonia: state-of-the-art advancements and future prospects," *Mater. Horiz.*, vol. 5, no. 1, pp. 9–27, 2018.
[123] A. J. Medford and M. C. Hatzell, "Photon-driven nitrogen fixation: current progress, thermodynamic considerations, and future outlook," *ACS Catal.*, vol. 7, no. 4, pp. 2624–2643, 2017.
[124] X. L. Xue, *et al*., "Review on photocatalytic and electrocatalytic artificial nitrogen fixation for ammonia synthesis at mild conditions: advances, challenges and perspectives," *Nano Res.*, vol. 12, no. 6, pp. 1229–1249, 2019.
[125] G. Q. Zhang, C. D. Sewell, P. X. Zhang, H. W. Mi, and Z. Q. Lin, "Nanostructured photocatalysts for nitrogen fixation," *Nano Energy*, vol. 71, 2020, Art. no. 104645.
[126] S. C. Jesudass, *et al*., "Pathways of the electrochemical nitrogen reduction reaction: from ammonia synthesis to metal-N_2 batteries," *Electrochem. Energy Rev.*, vol. 6, no. 1, 2023, Art. no. 27.
[127] C. Y. Hu, *et al*., "Surface plasmon enabling nitrogen fixation in pure water through a dissociative mechanism under mild conditions," *J. Am. Chem. Soc.*, vol. 141, no. 19, pp. 7807–7814, 2019.
[128] C. M. Aikens and O. A. Hull, "Theoretical investigations on the plasmon-mediated dissociation of small molecules in the presence of silver atomic wires," *J. Phys. Chem. A*, vol. 127, no. 10, pp. 2228–2241, 2023.
[129] J. H. Yang, *et al*., "High-efficiency "working-in-tandem" nitrogen photofixation achieved by assembling plasmonic gold nanocrystals on ultrathin titania nanosheets," *J. Am. Chem. Soc.*, vol. 140, no. 27, pp. 8497–8508, 2018.
[130] H. L. Jia, *et al*., "Site-selective growth of crystalline ceria with oxygen vacancies on gold nanocrystals for near-infrared nitrogen photofixation," *J. Am. Chem. Soc.*, vol. 141, no. 13, pp. 5083–5086, 2019.
[131] Y. Y. Yang, *et al*., "Construction of gold/rhodium freestanding superstructures as antenna-reactor photocatalysts for plasmon-driven nitrogen fixation," *J. Am. Chem. Soc.*, vol. 146, no. 11, pp. 7734–7742, 2024.
[132] L. W. Chen, *et al*., "Metal-organic framework membranes encapsulating gold nanoparticles for direct plasmonic photocatalytic nitrogen fixation," *J. Am. Chem. Soc.*, vol. 143, no. 15, pp. 5727–5736, 2021.
[133] S. C. Zhang, *et al*., "Concurrent mechanisms of hot electrons and interfacial water molecule ordering in plasmon-enhanced nitrogen fixation," *Adv. Mater.*, vol. 36, no. 15, 2024, Art. no. 2310776.
[134] X. Y. Zhu, S. R. Hatch, A. Campion, and J. M. White, "Surface photochemistry. 2. Wavelength dependences of photoinduced dissociation, desorption, and rearrangement of O_2 on Pt(111)," *J. Chem. Phys.*, vol. 91, no. 8, pp. 5011–5020, 1989.
[135] R. T. Kidd, D. Lennon, and S. R. Meech, "Comparative study of the primary photochemical mechanisms of nitric oxide and carbonyl sulfide on Ag(111)," *J. Phys. Chem. B*, vol. 103, no. 35, pp. 7480–7488, 1999.
[136] Z. M. Liu, S. A. Costello, B. Roop, S. R. Coon, S. Akhter, and J. M. White, "Surface photochemistry. 6. Methyl bromide on platinum (111)," *J. Phys. Chem.*, vol. 93, no. 22, pp. 7681–7688, 1989.
[137] E. Kazuma, J. Jung, H. Ueba, M. Trenary, and Y. Kim, "Direct pathway to molecular photodissociation on metal surfaces using visible light," *J. Am. Chem. Soc.*, vol. 139, no. 8, pp. 3115–3121, 2017.
[138] E. López-Tobar, B. Hernández, M. Ghomi, and S. Sanchez-Cortes, "Stability of the disulfide bond in cystine adsorbed on silver and gold nanoparticles as evidenced by SERS data," *J. Phys. Chem. C*, vol. 117, no. 3, pp. 1531–1537, 2013.
[139] E. Kazuma, J. Jung, H. Ueba, M. Trenary, and Y. Kim, "Real-space and real-time observation of a plasmon-induced chemical reaction of a single molecule," *Science*, vol. 360, no. 6388, pp. 521–525, 2018.
[140] T. E. Tesema, B. Kafle, M. G. Tadesse, and T. G. Habteyes, "Plasmon-enhanced resonant excitation and demethylation of methylene blue," *J. Phys. Chem. C*, vol. 121, no. 13, pp. 7421–7428, 2017.
[141] T. E. Tesema, C. Annesley, and T. G. Habteyes, "Plasmon-enhanced autocatalytic N-demethylation," *J. Phys. Chem. C*, vol. 122, no. 34, pp. 19831–19841, 2018.
[142] T. E. Tesema, B. Kafle, and T. G. Habteyes, "Plasmon-driven reaction mechanisms: hot electron transfer versus plasmon-pumped adsorbate excitation," *J. Phys. Chem. C*, vol. 123, no. 14, pp. 8469–8483, 2019.
[143] H. Kookhaee, T. E. Tesema, and T. G. Habteyes, "Switching a plasmon-driven reaction mechanism from charge transfer to adsorbate electronic excitation using surface ligands," *J. Phys. Chem. C*, vol. 124, no. 41, pp. 22711–22720, 2020.
[144] S. Kwiatkowski, *et al*., "Photodynamic therapy — mechanisms, photosensitizers and combinations," *Biomed. Pharmacother.*, vol. 106, pp. 1098–1107, 2018.
[145] A. Gellé, *et al*., "Enhancing singlet oxygen photocatalysis with plasmonic nanoparticles," *ACS Appl. Mater. Interfaces*, vol. 13, no. 30, pp. 35606–35616, 2021.
[146] J. L. Brooks, D. V. Chulhai, Z. W. Yu, J. D. Goodpaster, and R. R. Frontiera, "Plasmon-driven C-N bond cleavage across a series of viologen derivatives," *J. Phys. Chem. C*, vol. 123, no. 48, pp. 29306–29313, 2019.
[147] C. Boerigter, R. Campana, M. Morabito, and S. Linic, "Evidence and implications of direct charge excitation as the dominant mechanism in plasmon-mediated photocatalysis," *Nat. Commun.*, vol. 7, 2016, Art. no. 10545.
[148] C. Boerigter, U. Aslam, and S. Linic, "Mechanism of charge transfer from plasmonic nanostructures to chemically attached materials," *ACS Nano*, vol. 10, no. 6, pp. 6108–6115, 2016.
[149] L. J. Goossen, N. Rodriguez, B. Melzer, C. Linder, G. J. Deng, and L. M. Levy, "Biaryl synthesis via Pd-catalyzed decarboxylative coupling of aromatic carboxylates with aryl halides," *J. Am. Chem. Soc.*, vol. 129, no. 15, pp. 4824–4833, 2007.
[150] L. J. Goossen, W. R. Thiel, N. Rodriguez, C. Linder, and B. Melzer, "Copper-catalyzed protodecarboxylation of aromatic carboxylic acids," *Adv. Synth. Catal.*, vol. 349, nos. 14–15, pp. 2241–2246, 2007.

[151] A. Michota and J. Bukowska, "Surface-enhanced Raman scattering (SERS) of 4-mercaptobenzoic acid on silver and gold substrates," *J. Raman Spectrosc.*, vol. 34, no. 1, pp. 21–25, 2003.
[152] Y. Wang, *et al*., "Exploring the effect of intermolecular H-bonding: a study on charge-transfer contribution to surface-enhanced Raman scattering of p-mercaptobenzoic acid," *J. Phys. Chem. C*, vol. 118, no. 19, pp. 10191–10197, 2014.
[153] Y. Zong, Q. H. Guo, M. M. Xu, Y. X. Yuan, R. N. Gu, and J. L. Yao, "Plasmon-induced decarboxylation of mercaptobenzoic acid on nanoparticle film monitored by surface-enhanced Raman spectroscopy," *RSC Adv.*, vol. 4, no. 60, pp. 31810–31816, 2014.
[154] H. Huh, H. D. Trinh, D. Lee, and S. Yoon, "How does a plasmon-induced hot charge carrier break a C–C bond?" *ACS Appl. Mater. Interfaces*, vol. 11, no. 27, pp. 24715–24724, 2019.
[155] Q. F. Zhang, K. X. Chen, and H. Wang, "Hot-hole-induced molecular scissoring: a case study of plasmon-driven decarboxylation of aromatic carboxylates," *J. Phys. Chem. C*, vol. 125, no. 38, pp. 20958–20971, 2021.
[156] G. Smith, J. S. Girardon, J. F. Paul, and E. Berrier, "Dynamics of a plasmon-activated p-mercaptobenzoic acid layer deposited over Au nanoparticles using time-resolved SERS," *Phys. Chem. Chem. Phys.*, vol. 18, no. 29, pp. 19567–19573, 2016.
[157] Y. Q. Chen, *et al*., "Molecular coadsorption of p-hydroxythiophenol on silver nanoparticles boosts the plasmon-mediated decarboxylation reaction," *ACS Catal.*, vol. 12, no. 5, pp. 2938–2946, 2022.
[158] K. L. Wang, *et al*., "Modulating the plasmon-mediated decarboxylation reaction on silver nanoparticles by changing the surface adsorption of molecular cocatalysts of p-hydroxythiophenol," *J. Phys. Chem. C*, vol. 128, no. 8, pp. 3361–3369, 2024.
[159] E. Villarreal, G. F. G. Li, Q. F. Zhang, X. Q. Fu, and H. Wang, "Nanoscale surface curvature effects on ligand-nanoparticle interactions: a plasmon-enhanced spectroscopic study of thiolated ligand adsorption, desorption, and exchange on gold nanoparticles," *Nano Lett.*, vol. 17, no. 7, pp. 4443–4452, 2017.
[160] A. Tukova, M. T. Yaraki, A. Rodger, and Y. L. Wang, "Shape-induced variations in aromatic thiols adsorption on gold nanoparticle: a novel method for accurate evaluation of adsorbed molecules," *Langmuir*, vol. 39, no. 44, pp. 15828–15836, 2023.
[161] L. Xu, R. Ye, M. Mavrikakis, and P. Chen, "Molecular-scale insights into cooperativity switching of xTAB adsorption on gold nanoparticles," *ACS Cent. Sci.*, vol. 10, no. 1, pp. 65–76, 2024.
[162] R. Ye, *et al*., "Nanoscale cooperative adsorption for materials control," *Nat. Commun.*, vol. 12, no. 1, 2021, Art. no. 4287.
[163] A. M. Jackson, J. W. Myerson, and F. Stellacci, "Spontaneous assembly of subnanometre-ordered domains in the ligand shell of monolayer-protected nanoparticles," *Nat. Mater.*, vol. 3, no. 5, pp. 330–336, 2004.
[164] S. C. Huang, *et al*., "Probing nanoscale spatial distribution of plasmonically excited hot carriers," *Nat. Commun.*, vol. 11, no. 1, 2020, Art. no. 4211.
[165] D. D. Lopes, D. D. Abreu, R. A. Ando, and P. Corio, "Regioselective plasmon-driven decarboxylation of mercaptobenzoic acids triggered by distinct reactive oxygen species," *ACS Catal.*, vol. 12, no. 23, pp. 14619–14628, 2022.
[166] Y. J. Wei, *et al*., "Probing oxidation mechanisms in plasmonic catalysis: unraveling the role of reactive oxygen species," *Nano Lett.*, vol. 24, no. 6, pp. 2110–2117, 2024.
[167] P. Jiang, Y. Y. Dong, L. Yang, Y. R. Zhao, and W. Xie, "Hot electron-induced carbon–halogen bond cleavage monitored by in situ surface-enhanced Raman spectroscopy," *J. Phys. Chem. C*, vol. 123, no. 27, pp. 16741–16746, 2019.
[168] L. F. Yu, A. X. Du, L. Yang, Y. F. Hu, and W. Xie, "Quantifying hot electron energy contributions in plasmonic photocatalysis using electrochemical surface-enhanced Raman spectroscopy," *J. Phys. Chem. Lett.*, vol. 13, no. 24, pp. 5495–5500, 2022.
[169] R. Schürmann, A. Dutta, K. Ebel, K. Tapio, A. R. Milosavljevic, and I. Bald, "Plasmonic reactivity of halogen thiophenols on gold nanoparticles studied by SERS and XPS," *J. Chem. Phys.*, vol. 157, no. 8, 2022, Art. no. 084708.
[170] R. Schürmann, *et al*., "Microscopic understanding of reaction rates observed in plasmon chemistry of nanoparticle-ligand systems," *J. Phys. Chem. C*, vol. 126, no. 11, pp. 5333–5342, 2022.
[171] L. Nan, *et al*., "Investigating plasmonic catalysis kinetics on hot-spot engineered nanoantennae," *Nano Lett.*, vol. 23, no. 7, pp. 2883–2889, 2023.
[172] R. Schürmann and I. Bald, "Real-time monitoring of plasmon induced dissociative electron transfer to the potential DNA radiosensitizer 8-bromoadenine," *Nanoscale*, vol. 9, no. 5, pp. 1951–1955, 2017.
[173] J. Liu, *et al*., "Plasmonic hot electron-mediated hydrodehalogenation kinetics on nanostructured Ag electrodes," *J. Am. Chem. Soc.*, vol. 142, no. 41, pp. 17489–17498, 2020.
[174] A. Dutta, R. Schürmann, and I. Bald, "Plasmon mediated decomposition of brominated nucleobases on silver nanoparticles – a surface enhanced Raman scattering (SERS) study," *Eur. Phys. J. D*, vol. 74, no. 1, 2020, Art. no. 19.
[175] A. Dutta, R. Schürmann, S. Kogikoski, N. S. Mueller, S. Reich, and I. Bald, "Kinetics and mechanism of plasmon-driven dehalogenation reaction of brominated purine nucleobases on Ag and Au," *ACS Catal.*, vol. 11, no. 13, pp. 8370–8381, 2021.
[176] S. Kogikoski, A. Dutta, and I. Bald, "Spatial separation of plasmonic hot-electron generation and a hydrodehalogenation reaction center using a DNA wire," *ACS Nano*, vol. 15, no. 12, pp. 20562–20573, 2021.
[177] P. Singh, T. Deckert-Gaudig, Z. L. Zhang, and V. Deckert, "Plasmon induced deprotonation of 2-mercaptopyridine," *Analyst*, vol. 145, no. 6, pp. 2106–2110, 2020.
[178] B. B. Zhou, *et al*., "Real-time monitoring of plasmon-induced proton transfer of hypoxanthine in serum," *Nanoscale*, vol. 9, no. 34, pp. 12307–12310, 2017.
[179] L. T. M. Huynh, H. D. Trinh, S. Lee, and S. Yoon, "Plasmon-driven protodeboronation reactions in nanogaps," *Nanoscale*, vol. 12, no. 47, pp. 24062–24069, 2020.
[180] Z. L. Zhang, T. Deckert-Gaudig, P. Singh, and V. Deckert, "Single molecule level plasmonic catalysis – a dilution study of p-nitrothiophenol on gold dimers," *Chem. Commun.*, vol. 51, no. 15, pp. 3069–3072, 2015.
[181] M. T. Sun, Z. L. Zhang, Z. H. Kim, H. R. Zheng, and H. X. Xu, "Plasmonic scissors for molecular design," *Chem. Eur. J.*, vol. 19, no. 44, pp. 14958–14962, 2013.
[182] Y. Zhang, E. Villarreal, G. G. Li, W. Wang, and H. Wang, "Plasmonic nanozymes: engineered gold nanoparticles exhibit tunable plasmon-enhanced peroxidase-mimicking activity," *J. Phys. Chem. Lett.*, vol. 11, no. 21, pp. 9321–9328, 2020.

[183] C. Wang, Y. Shi, Y. Y. Dan, X. G. Nie, J. Li, and X. H. Xia, "Enhanced peroxidase-like performance of gold nanoparticles by hot electrons," *Chem. Eur. J.*, vol. 23, no. 28, pp. 6717—6723, 2017.
[184] E. Miliutina, *et al*., "Plasmon-assisted activation and grafting by iodonium salt: functionalization of optical fiber surface," *Adv. Mater. Interfaces*, vol. 5, no. 20, 2018, Art. no. 1800725.
[185] E. Miliutina, *et al*., "Can plasmon change reaction path? Decomposition of unsymmetrical iodonium salts as an organic probe," *J. Phys. Chem. Lett.*, vol. 11, no. 14, pp. 5770—5776, 2020.
[186] J. H. Zhou, J. Guo, G. Ghimire, A. M. Mebel, S. Chang, and J. He, "Plasmon-mediated dehydrogenation of the aromatic methyl group and benzyl radical formation," *Chem. Sci.*, vol. 14, no. 47, pp. 13951—13961, 2023.
[187] P. F. Han, *et al*., "Plasmonic silver-nanoparticle-catalysed hydrogen abstraction from the C(sp_3)-H bond of the benzylic C_α atom for cleavage of alkyl aryl ether bonds," *Angew. Chem. Int. Ed.*, vol. 62, no. 4, 2023. https://doi.org/10.1002/anie.202215201.
[188] R. K. Kashyap, S. Tyagi, and P. P. Pillai, "Plasmon enabled claisen rearrangement with sunlight," *Chem. Commun.*, vol. 59, no. 89, pp. 13293—13296, 2023.
[189] O. Guselnikova, *et al*., "Establishing plasmon contribution to chemical reactions: alkoxyamines as a thermal probe," *Chem. Sci.*, vol. 12, no. 11, pp. 4154—4161, 2021.
[190] A. M. Goodman, N. J. Hogan, S. Gottheim, C. Li, S. E. Clare, and N. J. Halas, "Understanding resonant light-triggered DNA release from plasmonic nanoparticles," *ACS Nano*, vol. 11, no. 1, pp. 171—179, 2017.
[191] P. K. Jain, W. Qian, and M. A. El-Sayed, "Ultrafast cooling of photoexcited electrons in gold nanoparticle-thiolated DNA conjugates involves the dissociation of the gold-thiol bond," *J. Am. Chem. Soc.*, vol. 128, no. 7, pp. 2426—2433, 2006.
[192] J. Stehr, *et al*., "Gold nanostoves for microsecond DNA melting analysis," *Nano Lett.*, vol. 8, no. 2, pp. 619—623, 2008.
[193] A. Wijaya, S. B. Schaffer, I. G. Pallares, and K. Hamad-Schifferli, "Selective release of multiple DNA oligonucleotides from gold nanorods," *ACS Nano*, vol. 3, no. 1, pp. 80—86, 2009.
[194] T. Kawano, Y. Niidome, T. Mori, Y. Katayama, and T. Niidome, "pNIPAM gel-coated gold nanorods, for targeted delivery responding to a near-infrared laser," *Bioconjugate Chem.*, vol. 20, no. 2, pp. 209—212, 2009.
[195] M. Reismann, J. C. Bretschneider, G. von Plessen, and U. Simon, "Reversible photothermal melting of DNA in DNA-gold-nanoparticle networks," *Small*, vol. 4, no. 5, pp. 607—610, 2008.
[196] A. Riedinger, *et al*., "Subnanometer local temperature probing and remotely controlled drug release based on azo-functionalized iron oxide nanoparticles," *Nano Lett.*, vol. 13, no. 6, pp. 2399—2406, 2013.
[197] X. Gu, H. Wang, and J. P. Camden, "Utilizing light-triggered plasmon-driven catalysis reactions as a template for molecular delivery and release," *Chem. Sci.*, vol. 8, no. 9, pp. 5902—5908, 2017.
[198] Y. F. Huang, H. P. Zhu, G. K. Liu, D. Y. Wu, B. Ren, and Z. Q. Tian, "When the signal is not from the original molecule to be detected: chemical transformation of para-aminothiophenol on Ag during the SERS measurement," *J. Am. Chem. Soc.*, vol. 132, no. 27, pp. 9244—9246, 2010.
[199] M. T. Sun and H. X. Xu, "A novel application of plasmonics: plasmon-driven surface-catalyzed reactions," *Small*, vol. 8, no. 18, pp. 2777—2786, 2012.
[200] Y. R. Fang, Y. Z. Li, H. X. Xu, and M. T. Sun, "Ascertaining p,p′-dimercaptoazobenzene produced from p-aminothiophenol by selective catalytic coupling reaction on silver nanoparticles," *Langmuir*, vol. 26, no. 11, pp. 7737—7746, 2010.
[201] Q. Zhang and H. Wang, "Mechanistic insights on plasmon-driven photocatalytic oxidative coupling of thiophenol derivatives: evidence for steady-state photoactivated oxygen," *J. Phys. Chem. C*, vol. 122, no. 10, pp. 5686—5697, 2018.
[202] K. Kim, D. Shin, J.-Y. Choi, K. L. Kim, and K. S. Shin, "Surface-enhanced Raman scattering characteristics of 4-aminobenzenethiol derivatives adsorbed on silver," *J. Phys. Chem. C*, vol. 115, no. 50, pp. 24960—24966, 2011.
[203] E. A. Merritt and B. Olofsson, "Diaryliodonium salts: a journey from obscurity to fame," *Angew. Chem. Int. Ed.*, vol. 48, no. 48, pp. 9052—9070, 2009.
[204] A. Yoshimura and V. V. Zhdankin, "Advances in synthetic applications of hypervalent iodine compounds," *Chem. Rev.*, vol. 116, no. 5, pp. 3328—3435, 2016.
[205] V. V. Zhdankin and P. J. Stang, "Chemistry of polyvalent iodine," *Chem. Rev.*, vol. 108, no. 12, pp. 5299—5358, 2008.
[206] R. B. Grubbs, "Nitroxide-mediated radical polymerization: limitations and versatility," *Polym. Rev.*, vol. 51, no. 2, pp. 104—137, 2011.
[207] C. J. Hawker, A. W. Bosman, and E. Harth, "New polymer synthesis by nitroxide mediated living radical polymerizations," *Chem. Rev.*, vol. 101, no. 12, pp. 3661—3688, 2001.
[208] J. Nicolas, Y. Guillaneuf, C. Lefay, D. Bertin, D. Gigmes, and B. Charleux, "Nitroxide-mediated polymerization," *Prog. Polym. Sci.*, vol. 38, no. 1, pp. 63—235, 2013.
[209] V. Sciannamea, R. Jérôme, and C. Detrembleur, "In-situ nitroxide-mediated radical polymerization (NMP) processes: their understanding and optimization," *Chem. Rev.*, vol. 108, no. 3, pp. 1104—1126, 2008.
[210] O. Guselnikova, *et al*., "Unprecedented plasmon-induced nitroxide-mediated polymerization (PI-NMP): a method for preparation of functional surfaces," *J. Mater. Chem. A*, vol. 7, no. 20, pp. 12414—12419, 2019.
[211] K. Fischer, *et al*., "Biomarker profiling by nuclear magnetic resonance spectroscopy for the prediction of all-cause mortality: an observational study of 17,345 persons," *PLoS Med.*, vol. 11, no. 2, p. e1001606, 2014, (in eng).
[212] M. Richard-Lacroix and V. Deckert, "Direct molecular-level near-field plasmon and temperature assessment in a single plasmonic hotspot," *Light Sci. Appl.*, vol. 9, no. 1, 2020, Art. no. 35.
[213] Q. Meng, *et al*., "Local heating and Raman thermometry in a single molecule," *Sci. Adv.*, vol. 10, no. 3, 2024, Art. no. eadl1015.
[214] C. J. Herring and M. M. Montemore, "Recent advances in real-time time-dependent density functional theory simulations of plasmonic nanostructures and plasmonic photocatalysis," *ACS Nanosci. Au*, vol. 3, no. 4, pp. 269—279, 2023.
[215] G. V. Naik, V. M. Shalaev, and A. Boltasseva, "Alternative plasmonic materials: beyond gold and silver," *Adv. Mater.*, vol. 25, no. 24, pp. 3264—3294, 2013.

[216] Y. Gutiérrez, A. S. Brown, F. Moreno, and M. Losurdo, "Plasmonics beyond noble metals: exploiting phase and compositional changes for manipulating plasmonic performance," *J. Appl. Phys.*, vol. 128, no. 8, 2020, Art. no. 080901.
[217] A. Agrawal, S. H. Cho, O. Zandi, S. Ghosh, R. W. Johns, and D. J. Milliron, "Localized surface plasmon resonance in semiconductor nanocrystals," *Chem. Rev.*, vol. 118, no. 6, pp. 3121—3207, 2018.
[218] A. Ten, V. Lomonosov, C. Boukouvala, and E. Ringe, "Magnesium nanoparticles for surface-enhanced Raman scattering and plasmon-driven catalysis," *ACS Nano*, vol. 18, no. 28, pp. 18785—18799, 2024.
[219] X. Y. Gan, E. L. Keller, C. L. Warkentin, S. E. Crawford, R. R. Frontiera, and J. E. Millstone, "Plasmon-enhanced chemical conversion using copper selenide nanoparticles," *Nano Lett.*, vol. 19, no. 4, pp. 2384—2388, 2019.
[220] H. Bai, *et al*., "A Schottky-barrier-free plasmonic semiconductor photocatalyst for nitrogen fixation in a "one-stone-two-birds" manner," *Adv. Mater.*, vol. 34, no. 2, 2022, Art. no. 2104226.